Role and Influence of Microalloying with Silver on Mechanical Properties and Deformation Behavior of Aluminum Alloys

A Thesis Submitted in
Partial Fulfillment of the Requirements
for the Degree of

DOCTOR OF PHILOSOPHY

by

PURNENDU KUMAR MANDAL

(Roll No. 09610315)

DEPARTMENT OF MECHANICAL ENGINEERING
INDIAN INSTITUTE OF TECHNOLOGY GUWAHATI
GUWAHATI-781039, INDIA
November 2017

DEPARTMENT OF MECHANICAL ENGINEERING

INDIAN INSTITUTE OF TECHNOLOGY GUWAHATI

GUWAHATI–781039, ASSAM, INDIA

CERTIFICATE

It is certified that the work contained in the thesis entitled **“Role and Influence of Microalloying with Silver on Mechanical Properties and Deformation Behavior of Aluminum Alloys”** submitted by **Mr. Purnendu Kumar Mandal (Reg. No. 09610315)** for the award of the degree of Doctor of Philosophy has been carried out under my supervision in the Department of Mechanical Engineering, Indian Institute of Technology Guwahati. This work has not been submitted elsewhere for the award of any other degree or diploma.

The thesis in my opinion, has reached the standard fulfilling the requirements for the award of degree of Doctor of Philosophy in accordance with the regulations of the institute.

Prof. P.S. Robi
Department of Mechanical Engineering
Indian Institute of Technology Guwahati
Guwahati – 781039, India

27th November, 2017

Dedicated

To

My Parents

ACKNOWLEDGEMENTS

I would like to express my heartfelt gratitude towards all those who have immensely helped me during this long arduous journey and eventually assisted me to emerge as an experienced researcher and a mature individual.

First and foremost, I must express my deepest sense of appreciation and respect for my thesis supervisor, Prof. P S Robi for providing me the opportunity to work under his supervision. His persistent patience and friendliness in the moments of difficulties have always been remembered and also his constant encouragement have played a crucial role in writing the thesis and bringing it to its present form.

I would like to thank my doctoral committee members, Prof. U S Dixit, Prof. A Srinivasan, Prof. G Pugazhenthi and Prof. S Senthilvelan for carefully reading the reports at various stages of evaluation and providing many useful comments, which have helped in the development of this thesis.

My sincere gratefulness to past and present departmental heads Prof. D Chakraborty, Prof. P Mahanta and Prof. A K Dass for their kind permission for enrollment, registration and several important supports at IIT Guwahati. I am also grateful to all the faculty members of Mechanical Engineering Department for giving me a comfortable and friendly environment for pursuing my research. I would also like to acknowledge the contribution of office staff, for helping me with various academic as well as non-academic issues.

I would like to express my sense of gratitude to Dr. D K Sharma and Mr. N K Das, past and present Assistant Workshop Superintendent and all the staffs of the workshop specially Mr. Mrinal Sarma, Mr. Dilip Chetri, Mr. Dhaneswar Khaklary, Mr. Chandan Banikya Mr. Ali and others for extending their help in fabrication of the different experimental set-ups for this work. I sincerely acknowledge the assistance received from Mr. Rituraj Saikia, Mr.Sanjib Sarma, Mr. Pranjol Paul, Mr. Saiffuddin Ahmed, Mr. Jiten Basumatary, Mr. Nip Borah and Dr. Sidananda Sarma in various experimental proceedings.

I also wise to express my gratitude to the Central Instrument Facility, IIT Guwahati to providing technical support with SEM, FESEM, FETEM and DSC.

The financial support of this research, which was provided by the Department of Mechanical Engineering, Indian Institute of Technology Guwahati, is gratefully acknowledged.

The most important support for this work came from my parents, Sri Jyotirmoy Mandal and Smt. Sovarani Mandal, for encouraging me to go still further at every points of life. I would like to thank my brother, sisters, sister-in-law, brother-in-law and also my nephew and niece. Parents for all of their love and support through the years, especially at peak of the economy encouraged me to pursue Ph.D on a modest stipend.

Finally the friends form an important part of this long and enduring journey, and without their constant support and encouragement, the completion of this thesis perhaps would have been an impossible task. I would therefore be forever be grateful to my closest friends Dr. Niladri Sett, Dr. Barun Gorain, Dr. Kalyan Manna, Dr. Kaushik Mondal, Dr. Himadri Nayak, Dr. Santu Das, Dr. Aravinda Kumar, Dr. Ratnakar Das, Dr. Perumalla Janaki Ramulu, Mr. Biplab Das, Mr. Arpan Kumar Mondal, Dr. Prakash Kumar Sahu, Mr. Rakesh Bhadra, Mr. Rasmi Ranjan Behera, Mr. Ambesh Kumar, Mr. Uttam Kumar Tarai and Mr. Sujit Das.

I consider myself privileged and fortunate to work in the Indian Institute of Technology Guwahati.

Above all, I am thankful to the Almighty.

27th November, 2017 Purnendu Kumar Mandal

ABSTRACT

The present study aimed to investigate the microstructure and mechanical properties of Al-Cu-Zn-Fe-Ti-Mg alloy (≈2219 aluminum alloy) microalloyed with silver (Ag in the range 0–0.1 wt.%) under different thermo-mechanical process conditions for obtaining high specific strength, reasonable ductility, high fracture toughness and good corrosion resistance properties. Five different alloys were prepared with varying silver content. Chemical analysis was done to determine the percentage composition by weight of each element of the alloy. Microstructural characterization and mechanical properties were determined at different heat treatment conditions in cast as well as cast-rolled conditions. Age hardening behavior of alloys was performed by means of transmission electron microscope (TEM). Hot deformation behavior and processing maps were also generated by relevant microstructural study. Artificial neural network (ANN) modeling was also carried out to predict the flow stress.

Microstructural investigation revealed the presence of intermetallic $CuAl_2$ and metastable Al-Cu-Fe-Zn-Si-Mn phases at the grain boundary regions. The metastable phase reduced with further solutionized heat treatment and subsequent rolling process. Also the dendritic structure was eliminated resulting in improved mechanical properties. During precipitation strengthening process hardness was at its peak in between 40–45 hour for all alloys at 150 °C temperature. The maximum hardness was observed in the alloy containing 0.07 wt.% silver after 45 hours of ageing at 150 °C.

The strength and hardness increased with the increase in silver content up to 0.07 wt.% along with reasonable ductility. The highest strength of the alloy was obtained in the rolled-solutionized-age hardened condition. Tensile fracture surface observation by scanning electron microscope revealed brittle failure mode in as-cast alloys whereas the heat treated alloys exhibited features typical of ductile failure.

The hot compression tests were carried out at constant true strain rates in the range of 0.001–10 s^{-1} and temperatures in the range of 300–500 °C. The flow stress of alloys decreased with increasing silver content. Constitutive models correlating the peak flow stress with deformation temperature and strain rates for the two alloys were developed using hyperbolic-sine relationship. The activation energy for deformation of the 2219 aluminum alloy decreased with the addition of silver. Comparison of the predicted and experimental values of peak flow stress revealed that 88% of the data could be predicted within an error of ± 12.5% indicating good predictive capability for the developed constitutive relationships.

Flow stress as a function of strain, strain rate and temperature during hot deformation was predicted for all alloys by artificial neural network (ANN) modeling in “MATLABR201a”. A large number of simulations were carried out to generate a weight function as well as to reduce the error. The coefficient of determination (R^2) during the prediction of more than 0.97 indicates very good prediction capability by artificial neural network technique.

CONTENTS

LIST OF FIGURES

LIST OF TABLES

Nomenclatures

a	Atomic size
b	Burger vector
d	Particle diameter
d_c	Critical particle diameter
E	Young’s modulus
e_f	Fracture strain
μ	Shear modulus
G	Dissipater content
J	Dissipater co-content
K	Strength coefficient
K	Temperature in kelvin
m	Strain rate sensitivity
n	Strain hardening exponent
P	Pressure
Q	Activation energy for high temperature deformation
R	Universal gas constant (8.314 J/mol.K)
R^2	Coefficient of determination
s	Standard deviation
S	Inter-particle spacing
$\mathrm{S_o}$	Yield strength
$\mathrm{S_u}$	Ultimate tensile strength
T	Absolute temperature
t	Time
T_e	Peak end temperature
T_m	Melting temperature
T_o	Peak onset temperature
T_p	Peak temperature
V	Volume
Z	Zener-Hollomon parameter

Greek

$\dot{\varepsilon}$	True strain rate
$\xi\left(\dot{\varepsilon}\right)$	Instability parameter
σ	Flow stress
θ	$CuAl_2$
ε	True strain
σ_p	Peak flow stress
σ_s	state flow stress
ε_p	Peak strain
α	Stress multiplier
ΔE	Activation energy for precipitation reaction
η	Efficiency of power dissipation
ϕ	Heating rate

Abbreviations

AAS	Atomic absorption spectroscopy
ANN	Artificial neural network
ASTM	American Society for Testing and Materials
BCT	Body centered tetragonal
DMM	Dynamic materials model
DRX	Dynamic recrystallization
DSC	Differential scanning calorimeter
EDS	Energy dispersive X-ray spectrometer
GP-Zones	Guinier-Preston-zones
MSE	Mean squared error
RMS	Root mean square
SEM	Scanning electron microscope
SFE	Stacking fault energy
TEM	Transmission electron microscope
UTM	Universal testing machine
UTS	Ultimate tensile strength
VHN	Vickers hardness number
YS	Yield strength
wt.%	Weight percentage
at.%	Atomic percentage
vol.%	Volume percentage

Chapter 1

Introduction

The search for new materials with enhanced properties for industrial and structural applications, during the last several decades, has led to the development of many metallic alloys. An alloy is a solid solution made of two or more metallic elements or metal and non-metal elements in a metallic matrix. Alloys can be either of (i) homogeneous solid solution, (ii) heterogeneous mixture of tiny crystals, (iii) true chemical compound, or (iv) mixture of all these. Among all alloys, ferrous alloys are most widely used for engineering applications due to their favorable mechanical properties that can be tailored by thermo-mechanical treatments. However, their use in aircraft and space applications are impeded due to their high density compared to non-ferrous alloys such as titanium (Ti), aluminium (Al), and magnesium (Mg). The high demand for light weight alloys for strategic applications has resulted in a thrust for the development of light weight non-ferrous alloys exhibiting high strength, high fracture toughness, good corrosion resistance and reasonable ductility [1–3]. Among the non-ferrous alloys, light alloys of aluminum, titanium, magnesium etc. have been the main focus of research in the development of high strength lightweight materials due to their very low density, ease of manufacture and minimum environmental problems compared to other alloy systems. Out of these light weight alloy systems, aluminum alloys have been used extensively for structural applications [1–4].

Aluminum alloys are mainly classified into: (i) cast alloys that are solidified inside molds to obtain desired shape and size before use and (ii) wrought alloys that are cast into ingots and plastically deformed to obtain different sections like wires, rods, tubes, or sheets [1–3]. It is generally known that deformation processing of wrought alloys results in elimination of casting defects such as micro-porosities, dendritic structure, inter-dendritic segregation, presence of large second phase particles, etc. The deformation process also results in the refinement of grain size and reduction in the size of second phase particles present during the casting process leading to improved mechanical properties [1–5].

Among the aluminum alloys, wrought Al-Cu (2xxx), Al-Mg-Si (6xxx) and Al-Cu-Zn-Mg (7xxx) series alloys have been studied extensively due to their high specific strength [1, 2]. These alloys, after plastic deformation, are subjected to heat treatments such as (i) solid solution heat treatment where the solutes dissolve in the aluminum lattice resulting in strengthening and (ii) age hardening heat treatment of the solutionized alloy. The age hardening process is accompanied by uniform precipitation of fine intermetallic particles in the alloy matrix that acts as impediments for the movement of dislocations along the slip plane thereby improving the mechanical properties [6–7].

Sufficient information is available regarding the effect of mechanical properties of commercial wrought aluminum alloys produced by addition of one or more other metallic elements where the amount of alloying elements are generally greater than 1.0 wt.% [9–13]. The extent of strengthening in these commercial alloys by various thermo-mechanical treatments has almost reached a saturation level. The recent research trend to obtain aluminum alloys with better combination of properties is by microalloying the existing commercial alloys, i.e. by addition of trace amounts (< 0.1 wt.%) of elements like tin (Sn), cadmium (Cd), scandium (Sc), titanium (Ti), silver (Ag), zirconium (Zr) and indium (In) etc. Trace addition of these elements influence the microstructure and mechanical properties of the base alloy [14–18]. However, only limited investigations regarding the effect of microalloying on the heat treatable 2xxx series of aluminum alloys have been carried out so far. Addition of 0.05 wt.% titanium (Ti) has been found to increase the strength of Al-4.5Cu-0.3Mg alloy by around 10% [18]. Investigation reveals that even small variations in tin (Sn) content in the range 0–0.1 wt.%, results in major changes in microstructure and mechanical properties of 2219 alloy [17, 19]. These studies reveal that the strength increases with increase in tin (Sn) content in the alloy up to 0.06 wt.% and further addition of tin (Sn) reduces the strength [17]. The potential advantages and the general lack of information regarding microalloying of high strength commercial Al-Cu alloys is one of the motivations behind the present work.

Investigations have been carried out to study the effect of silver addition (in the range 0.3–0.5 wt.%) on the mechanical properties, hot deformation characteristics and age hardening behavior of Al-Cu-Mg alloys [20–23]. Addition of 0.3 wt.% silver (Ag) accelerates the precipitation hardening behavior resulting in an increase in the strength and hardness of Al-Cu-Mg (2519 Al) alloy [20]. Addition of 0.48 wt.% silver

(Ag) reveals that the hot deformation microstructure is sensitive to strain rate and deformation temperature [21]. It also accelerates the precipitation kinetics with simultaneous increase in the peak hardness, yield strength and ultimate tensile strength of Al-Cu-Mg alloy [22]. The effect of ageing on the microstructure and mechanical properties of Al-Cu-Mg alloy containing 0.5 wt.% silver (Ag) indicates that the peak hardness of the alloy is same for the T6 temper and T614 temper conditions [23].

The precipitation sequence and its influence on the mechanical properties of Al-Cu-Mg alloys during the age hardening process has been well established [7–9, 11, 17, 20, 22]. The optimum mechanical properties that can be achieved by precipitation strengthening are influenced by (i) nature of the precipitates, (ii) coherency between the precipitate and the matrix, (iii) size of the precipitates and (iv) inter particle spacing between the precipitates in the matrix. The reaction sequence occurring in the supersaturated solid solution (SSS) Al-Cu-Mg alloy during age hardening initiates with the formation of Guinier-Preston-zones (GP-zones). GP-zones contain clusters of monoatomic layer of copper atom on the (001) planes of the aluminum lattice. Further age hardening results in formation of Ω phase by diffusion of copper atoms into the matrix and formation of additional layers of GP-zones. The entire precipitate formation in the aluminum matrix occurs by the following sequence:

$$\text{SSS} \rightarrow \text{GP-zone} \rightarrow \theta''\text{phase} \rightarrow \theta'\text{phase} \rightarrow \theta\,\text{phase}$$

The GP-zone and θ'' phase are fully coherent with the matrix, whereas θ' phase is disk shaped and semi-coherent with the matrix. The final θ precipitate phase is almost spherical in shape and incoherent at the precipitate matrix interface regions. This precipitate exhibits a body centered tetragonal structure with $a = b = 0.6066$ nm, $c = 0.4874$ nm [17, 24].

Precipitation sequence in Al-Cu-Mg alloys containing small amount of silver (Ag), 0.1 wt.% $\leq$Ag $\leq$ 0.2 wt.%, during age hardening was studied by researchers [24]. The study revealed that the as-quenched ternary Al-1.7Cu-0.5Mg alloy was accompanied by the presence of high density of dislocation loops. It was observed that the first stage of hardening in this alloy was due to the formation of GP-zones from the solution of Cu-Mg co-clusters. Addition of 0.1 wt.% silver into this alloy reveled absence of dislocation loops indicating trapping of vacancies by silver atoms in the as-quenched condition. The early stage of age hardening in this tertiary alloy was accompanied by nucleation of Mg-Ag co-clusters, Mg-Cu co-clusters and Mg clusters in the matrix [25]. The final hardening of Al-Cu-Mg-Ag alloy has been attributed to the presence of GP-zones, finely dispersed hexagonal X′ phase, and S phase formed from the GP-zones [25]. Also the tertiary Al-Cu-Mg-(Ag) alloys with high copper to magnesium (Cu:Mg) ratio and very low magnesium (Mg) content lie in the $\alpha + \theta$ region of the ternary phase diagram [26].

Sufficient literature is available regarding the microstructure of Al-Cu alloys in the wrought condition. However, few reports are available regarding the microstructure of these alloys in the as-cast condition and modification of the microstructure by subsequent plastic deformation. Addition of silver in very small amount can have profound influence on the microstructure and strength of Al-Cu alloys. The available literature regarding the mechanical properties of Al-Cu-Mg-Ag alloys revealed that the silver content in the investigated alloys are 0.3 wt.% or more [20, 22]. From the few reports available, it is not obvious whether better mechanical properties for Al-Cu alloys can be achieved with silver content less than 0.1 wt.%. Among the Al-Cu alloys, 2219 aluminum alloy exhibits high fracture toughness, good weldability and is less resistant to stress corrosion cracking in addition to the fact that the strength and ductility can be tailored by heat treatment [1, 2].

All commercial high strength aluminum alloys are precipitation hardenable wrought alloys. The primary processing of these alloys is by casting into ingots. For obtaining the final component with the required size, shape and properties, the material is subjected to various thermo-mechanical treatments like rolling, forging, extrusion, heat treatment etc. As mentioned earlier, the secondary processing improves the mechanical properties of the wrought alloys by elimination of defects formed during the casting stage. The secondary deformation processing is generally carried out in the warm/hot working conditions. Since it is necessary to have a defect free component during the deformation processing, an insight into the material parameters and processing conditions are required a priori [27, 28].

The deformability of materials during mechanical working is generally characterized by constitutive equations, which relate the flow stress to the strain, strain rate and temperature. The deformability of the material depends on: (i) the inherent flow characteristics of the material such as flow stress and activation energy (*Q*) for deformation, which is directly influenced by the alloy composition and (ii) externally controlled process variables like strain, strain rate and temperature [29–34]. Hu at al. [35] reported that activation energy for hot deformation decreases with increasing deformation temperature and increase in strain rate. The composition and microstructure of the material also influence the activation energy during deformation [36]. Constitutive relationships for commercial aluminum alloys were developed using experimental data obtained by mechanical testing and are represented in the form of empirical rate equations, which helps in identification of the specific rate-controlling mechanisms [37]. Flow stress behavior of several aluminum alloys have been studied extensively by carrying out hot compression tests. These investigations reveal that the plastic deformation of aluminum alloys at elevated temperatures is a thermally activated process with an activation energy *Q*. The flow stress has either an exponential, power law or hyperbolic-sine relationship with temperature and strain rate [21, 38].

In high temperature deformation studies, two main areas of interest are: (i) metal forming by hot working and (ii) creep deformation. Though both are being studied at almost the same temperature range, the major objectives in the former case are to raise the fracture strain and to reduce the flow stress during deformation. In the latter case, emphasis is towards achieving low strain rates and limiting the total strain [27, 28]. Various constitutive relationships have been developed to model the high temperature deformation behavior of materials [31–33]. These studies show that the stress can also be represented by a Zener–Hollomon parameter, Z. Almost all the constitutive modeling studies on the deformation behavior of commercially available alloys were focused on determining (i) Zener–Hollomon parameter, (ii) activation energy for deformation and (iii) various constants in the constitutive models. These are influenced by small variations in the composition and microstructure of the alloys [31–34]. Though the constitutive equations can explain the hot deformation behavior of materials in terms of strain, strain rate and temperature, they are unable to identify the process regime at which defect formation initiates during the deformation process [37].

An important parameter to be considered during the deformation processing of any material is the workability (or deformability), which refers to the extent to which a metal can be deformed without the formation of any defect [39]. In recent years, dynamic materials model (DMM) has been developed for understanding the workability parameter. Dynamic materials model was first developed based on the fundamental principles of continuum mechanics of large plastic flow using the concepts of physical systems modeling, principles of irreversible thermodynamics and those describing the stability of the system. The dynamic materials model may be viewed as a bridge between the continuum mechanics of large plastic deformation and microstructural evolution [40–42].

During plastic deformation, depending upon the strain rate and temperature, several irreversible metallurgical phenomena occur inside the material [37, 39]. Some of these are (i) dynamic recrystallization, (ii) superplastic deformation, (iii) flow localization and/or adiabatic shear band formation, (iv) void formation, (v) inter-crystalline cracking along grain boundaries. Out of all these, dynamic recrystallization and superplastic deformation are considered to be safe while the process regime at which other phenomena occur should be avoided. These safe process regimes can be identified by investigation of the microstructure of samples that have been hot deformed under various combinations of strain, strain rate and temperature. The workability parameter can be represented in the form of processing maps. The processing map is obtained by superimposing a power dissipation map and an instability map obtained from the stress–strain data during hot deformation process. The power dissipation map is a contour plot of efficiency of power dissipation as a function of strain rate and temperature at a particular strain. Instability map demarcates the regions of stable and unstable flow. The processing map provides useful information that can be applied to industrial metal working processes. During the development of new materials, the processing maps can be used to suit the requirements of the material from the viewpoint of optimum workability and microstructural control [37, 39, 41–43].

One of the major hurdles in obtaining a process map is to find out the strain rate sensitivity for the entire domain of temperature and strain rates. Hot compression tests for generation of processing maps are generally carried out at different combinations of constant temperature and strain rates. The strain rate at which experiments are generally carried out differ by several orders of magnitude. Determination of the flow stress and strain rate sensitivity for the entire experimental domain using the data obtained from limited number of experiments requires an efficient computational technique. Artificial neural network technique is found to be an efficient and accurate interpolation technique for the determination of the flow stress and strain rate sensitivity for the entire process regime of temperature, strain rate and strain [40, 44].

The motivation for choosing the present thesis work is highlighted as follows :

- ✓ Sufficient literature is available regarding the microstructure of Al-Cu alloys in the wrought condition. However, few reports are available regarding the microstructure of these alloys in the as-cast condition and modification of the microstructure by subsequent plastic deformation;
- ✓ Among the Al-Cu alloys, 2219 aluminum alloy exhibits high fracture toughness, good weldability and are less resistant to stress corrosion cracking in addition to the fact that the strength and ductility can be tailored by heat treatment.
- ✓ Addition of silver in very small amount can have profound influence on the microstructure and strength of Al-Cu alloys. The available literature regarding the mechanical properties of Al-Cu-Mg-Ag alloys revealed that the silver content in the investigated alloys are 0.3 wt.% or more. From the few reports available, it is not obvious whether better mechanical properties for Al-Cu alloys can be achieved with silver content less than 0.1 wt.%.
- ✓ The influence of microalloying with silver on the age hardening behavior, microstructure and mechanical properties of 2219 aluminum alloy under various thermo-mechanical conditions is not well established.
- ✓ The hot deformation characteristics of 2219 aluminum alloys microalloyed with silver have not been investigated. For the successful processing of these materials requires generation of processing maps for the new materials. This will give

insight to the safe process parameters and the microstructural changes during hot deformation.

The main objectives of the present research study are follows:

1. To process the precipitation hardenable wrought Al-Cu alloys (2219 Al alloy) microalloyed with varying amount of silver (in the range 0 to 0.1) by casting route.
2. To study the microstructures and mechanical properties of these alloys in the as-cast, rolled and different heat treated conditions and compare the properties with respect to the silver content in the alloy.
3. To optimize the age hardening conditions required to achieve peak hardness in the developed alloys and study the influence of silver addition during age hardening of 2219 aluminum alloy.
4. To study the effect of silver addition on the high temperature deformation behavior of 2219 aluminum alloy and develop constitutive models for predicting the peak flow stress during high temperature deformation of these materials.
5. To predict the high temperature flow stress (σ) for the developed alloys as a function of strain (ε), strain rate ($\dot{\varepsilon}$) and temperature (T) using artificial neural network modeling.
6. To generate processing maps for the microalloyed 2219 aluminum alloys and identify the safe process zones for these alloys, mechanism of hot deformation as well as defect formation.

This thesis is arranged in five chapters. Chapter 1 presents a brief introduction to the thesis work. Chapter 2 summarizes the available literature on topics relevant to the contents of this thesis. The details regarding the experimental methodology adopted, instruments used and the procedures followed for processing and characterizing the alloys is described in detail in Chapter 3. This also includes the modeling work performed for predicting the flow stress and procedure for generation of processing maps. The results obtained are presented and discussed in Chapter 4. The major conclusions drawn from the study and future scope of investigation in this area are enumerated in Chapter 5.

Chapter 2

Literature Review

2.1 Introduction

Appreciable interest in the development of metallic alloys for industrial applications was observed starting from the beginning of last century. Alloys of light metals such as aluminum and magnesium are used as structural materials in applications like automobile, aerospace, food packaging and wire cable industry etc., due to the combination of high strength, light weight, reasonable ductility and excellent formability. The recent focus is on the development of light weight alloys exhibiting high specific strength [4] for aircraft and space applications. Aluminum (Al) alloys are found to be most suitable for these applications. Several decades of intense research work has focused on the development of alloys having high specific strength, reasonable ductility, high fracture toughness, and good corrosion resistance properties for alloys of aluminum, titanium, magnesium etc. Aluminum-lithium alloys have recently been developed for use by these industries. These materials have relatively low densities (between about 2.5 and 2.6 g/cm^3), high specific moduli, good fatigue resistance and low-temperature toughness properties. However, due to the requirement of special processing techniques, these alloys are costlier compared to the conventional aluminum alloys [3]. Among these traditional aluminum alloys, the wrought and precipitation strengthened Al-Cu (2xxx series), Al-Mg-Si (6xxx series) and Al-Cu-Zn-Mg (7xxx series) series of alloys have been studied extensively due to their high strength to weight ratio [1–3].

2.2 Aluminum alloys

Aluminum alloys are classified into cast and wrought alloys. The wrought aluminum alloys are further classified into non-heat treatable and heat treatable alloys. Better mechanical properties of heat treatable alloys are achieved from work hardening. The heat treatable wrought aluminum (Al) alloys respond to heat treatment and develop their strength mainly by age hardening. Examples are alloys of 2xxx, 6xxx and 7xxx series aluminum alloys [1–3].

A major amount of the aluminum alloys used for space and aircraft applications are manufactured by either the ingot casting or direct chill casting technique. The ingots are then homogenized at temperatures of around 500 °C to achieve a homogeneous composition across the section. These are then hot rolled or warm rolled into slabs, rods or plates. Subsequently they are solution heat treated followed by precipitation treatment to achieve the desired strength and ductility. Among the aluminum alloys, wrought and precipitation strengthened Al-Cu (2xxx), Al-Mg-Si (6xxx) and Al-Cu-Zn-Mg (7xxx) series alloys have been studied extensively due to their high specific strength [1–3].

Sufficient information is available regarding the effect of mechanical properties of commercial aluminum alloys by addition of one or more elements like magnesium (Mg), silicon (Si), copper (Cu), zinc (Zn) etc. [9–13]. The strengthening of non-precipitation hardenable aluminum alloys are due to either the nucleation of second phase particles during solidification or solid solution strengthening [7–9]. Addition of elements like magnesium (Mg) and manganese (Mn) into aluminum alloy results in almost linear dependence of strength on the concentration of alloying elements [7]. Addition of manganese (Mn) was found to have higher strengthening effect compared to magnesium [7]. Presence of iron (Fe) and manganese (Mg) in Al-Si alloys results in the formation of intermetallic compounds [45].

The strength of Al-Mg alloy increases with magnesium (Mg) content in the alloy up to 5.5 wt.%. The ductility and strain rate sensitivity of Al-Mg alloys increases with the addition of elements like manganese (Mn) within the range of 0.3–0.5 wt.% and 0.18 wt.% zirconium [46]. Precipitation strengthening of Al-Mg-Si alloy is by the nucleation and growth of Mg_2Si precipitates in the aluminum matrix. Addition of copper into these alloys results in grain refinement, change in precipitation sequence, acceleration in precipitation kinetics, and increase in peak hardness values [47, 48]. The segregation of S_1 phase at grain boundary regions in Al-Mg-Li-Me alloys decreases when the Mg content in the alloy reduces from 5 wt.% to 3.5 wt.%. [10]. Addition of silicon (Si), more than 4wt.%, into Al-5wt.% Cu alloy increases fluidity of the molten metal and reduces the hot cracking tendency [12] during casting.

2.3 Effect of alloying elements in aluminum alloys

Considerable amount of studies have been carried out to understand the effect of traditional alloying elements such as copper (Cu), magnesium (Mg), zinc (Zn), silicon (Si), silver (Ag) etc. on the mechanical properties of some commercial aluminum alloys. In wrought precipitation hardenable aluminum alloys, the alloying element(s) present as solute atoms in the solvent lattice sites are responsible for strengthening [48].

Addition of copper (Cu) into aluminum (Al) matrix facilitates strengthening by solid state strengthening or precipitation hardening mechanisms. During aging the strengthening is achieved through the precipitation of $CuAl_2$ or $CuAl_2Mg$ intermetallic phases. These precipitates also improve the elevated temperature properties, machinability and fatigue properties of the alloy. Copper in excess of 6 wt.% in the alloy results in precipitation of the second phases at the grain boundaries, making the metal very susceptible to stress corrosion, pitting or inter-granular corrosion. Copper (Cu) in higher amounts makes the Al-Cu alloys vulnerable to solidification cracking. Also addition of copper (Cu) to Al-Mg-Si alloys has been found to influence the strengthening and grain refinement [49–53].

An Al-Mg alloy are strengthened by solid solution strengthening along and also increases the strain hardening ability. A few Al-Mg alloys tend to increase their strength and ductility when age hardened at room temperature. These alloys tend to further increase in strength by artificial ageing and also show increase in yield strength at a substantial reduction in ductility. Though no significant effect on tensile, ductility, strain-rate sensitivity or flow stress could be observed in Al-Mg alloys having magnesium in the range of 2.8 % to 5.5 % [46], the mechanical properties are found to improve with magnesium content above 5.5 wt.%.

Silicon (Si) is added to improve the properties of cast aluminum alloys. Addition of silicon increases the fluidity of the aluminum alloys. The high strength 6xxx series alloys contain around 1.0 wt.% magnesium (Mg) along with 0.6 wt.% silicon (Si). In these alloys the main strengthening particles are magnesium silicide (Mg_2Si), which is precipitated in the matrix during heat treatment [45].

Addition of manganese (Mn) increased the strength of Al-Cu-Mg alloys. The strengthening mechanism is by solution strengthening or formation of finely precipitated intermetallic phase. Addition of magnesium (Mg) improves strain hardening of the alloy without much compromise on the ductility or corrosion resistance. However the Mg content is limited to ≤ 1 % since further increase leads to decrease in ductility [7].

Presence of iron (Fe) in Al-4%Cu-0.5%Mg reduces the tensile properties in the heat-treated condition [1, 2]. Presence of iron (Fe) forms Cu_2FeAl_7. Fe in Al-Cu-Ni alloys improves the elevated temperature strength. Addition of zinc (Zn) to aluminum (along with magnesium and copper) produces heat-treatable aluminum alloys, with the highest strength among all aluminum alloys. Addition of silver (Ag) in trace levels substantially increases the strength of age hardenable Al-Cu-Mg alloys [1, 2]. Addition of cadmium (Cd) to Al-Cu alloys accelerates the age hardening process and increases the strength and corrosion resistance. Up to 0.2 wt.% of indium (In) in Al-Cu alloys, reduces room temperature ageing. Vanadium (V), zirconium (Zr) and titanium (Ti) raise the recrystallization temperature of Cu-Al alloys, thereby permitting to retain their properties at elevated temperatures [1, 2]. Titanium (Ti) is added to aluminum primarily as a grain refiner. Nickel (Ni) up to 2 wt.% increases the strength of high-purity aluminum but reduces its ductility. Lead (Pb) is primarily added to improve machinability of Al alloys [1, 2].

2.4 Effect of microalloying of aluminum alloys

The information regarding the effect of addition of alloying elements on the mechanical properties of Al alloys is well established [1, 4]. The extent of improving the mechanical properties by the addition of various elements have almost reached a saturation level. The recent efforts in improving the mechanical properties are by microalloying (i.e., by the addition of trace amounts of elements) the commercial Al alloys with some specific elements.

Addition of 0.4 wt.% scandium increases the strength of Al-Mg alloys due to the precipitation of Al_3Sc particles in the matrix [13] whereas addition of 0.15 wt.% zirconium (Zr) and 0.4 wt.% scandium (Sc) results in a stabilized microstructure for the alloy [54]. Addition of 0.2 wt.% erbium (Er) increases the elevated temperature strength of Al-Mg-Mn-Zr alloy by precipitation of Al_3Er particles in the alloy matrix [54]. Alloying Al-7Si-0.4Mg alloy with 0.1 wt.% indium delays the precipitation of GP-zones, thereby decelerating the precipitation hardening kinetics of the alloy [31].

The recent research trend to obtain aluminum alloys with better combination of properties is by microalloying the existing commercial alloys, i.e. by addition of trace amounts (< 0.1 wt.%) of elements like tin (Sn), cadmium (Cd), scandium (Sc), silver (Ag), zirconium (Zr), indium (In) etc. [14–18]. Addition of these elements influences the microstructure and mechanical properties of the base alloy [14–16]. The study reveals that the best combination of mechanical properties of Al-Si-Mg alloy is achieved by the addition of 0.05 wt.% tin (Sn) [55]. Further increase in tin content leads to the precipitation of β-Sn particles within the $CuAl_2$ network as well as the formation of very fine Mg_2Sn particles on the eutectic silicon (Si) resulting in lowering of tensile properties of the alloy. Presence of titanium (Ti) above 0.05 wt.% increases the strength of Al-4.5Cu-0.3Mg alloy [18]. However, the strength of the alloys are reduced due to hot tearing defects during the casting process when the titanium content was below 0.05 wt.%.

A systematic investigation on the effect of trace amounts of Sn (up to 0.1 wt.%) on mechanical properties, microstructure and hot deformation behavior etc., reveals that even small variations in tin (Sn) content results in major changes in microstructure and mechanical properties of 2219 alloy [19, 44]. The results of the investigations reveals that the strength increases with increase in tin (Sn) content in the alloy up to 0.06 wt.%. Further, addition of tin (Sn) reduces the mechanical properties of the alloy. Sufficient literature is available regarding the effect of addition of elements like tin, indium, scandium, etc. on the microstructure and mechanical properties of commercial aluminum alloys.

Investigations have been carried out to study the effect of silver addition (0.3 – 0.5 wt.%) on the mechanical properties, hot deformation characteristics and age hardening behavior of Al-Cu-Mg alloys. Addition of 0.5 wt.% silver (Ag) in Al-Cu-Mg alloy revealed that the hot deformation microstructure is sensitive to strain rate and deformation temperature [21]. The effect of interrupted ageing on the microstructure and mechanical properties of Al-Cu-Mg alloy containing 0.5 wt.% Ag indicates that the peak hardness of the alloy is same for T6 temper and T614 temper conditions whereas better thermal stability is achieved for the T614 tempered alloy [23]. Addition of 0.3 wt.% Ag accelerates the precipitation hardening behavior as well as increase in the strength and hardness of Al-Cu-Mg (2519 Al) alloy [20]. Addition of 0.48 wt.% silver accelerates the precipitation kinetics with simultaneous increase in the peak hardness of Al-Cu-Mg alloy. The yield strength and ultimate tensile strength of the alloy also increases due to the addition of 0.48 wt.% silver [22].

The available literature reveals that the silver (Ag) content in the investigated alloys are above 0.1 wt.%. Studies regarding the effect of microalloying (i.e. alloying with ≤ 0.1 wt.%) with silver on the microstructure, and mechanical properties of Al-Cu alloy under different processing conditions are not available in the literature. Hence the present work is aimed in studying the effect of addition of trace amounts of silver (Ag) (≤ 0.1 wt.%) on the microstructure and mechanical properties of as-cast and rolled 2219 Al-alloy at different thermo-mechanical conditions.

2.5 Precipitation strengthening

Metallic alloys having elements as solutes with limited solid solubility in solution can be strengthened by solid solution strengthening and /or precipitation strengthening [1, 3, 6, 48]. In solid solution alloys, the strengthening is the result of expansion of crystal lattice due to substitution of parent metal atom by substitutional elements. The alloys for which the phase diagram exhibits an increase in the solute solubility limit with increase in temperature, can be solutionized at elevated temperature and then suddenly cooled to room temperature. Under such circumstances, a supersaturated solid solution of solute in the solvent is formed. If the temperature of the alloy is then raised to an intermediate level and held for sufficient time, the solute elements diffuse out of the solution and form fine stable precipitates in the matrix. Formation of stable precipitates is a thermally activated process consisting of nucleation and growth. During this process the variation of the hardness with respect to ageing time is illustrated schematically in Figure 2.1. The reaction sequence occurring in the supersaturated solid solution (SSS) Al-Cu-Mg alloy during age hardening initiates with localized clustering of solute atoms known as GP-zones. GP-zones contain clusters of monoatomic layer of Cu atom on the (001) planes of the Al lattice and is fully coherent with the matrix. The formation of GP-zone results in local strains, thereby raising the hardness of the alloy. Further aging results in the formation of larger clumps of copper atoms on (001) plane of the matrix [3, 6]. This structure is known as θ''. This is followed by precipitation of platelets of $CuAl_2$ or θ', which are semi-coherent with the matrix. This results in further increase in hardness of the alloy. Extended ageing results in the formation of equilibrium phase $CuAl_2$ or θ from the transition θ' phase. The entire precipitate formation occurs by the following sequence:

$$\text{SSS} \rightarrow \text{GP-zone} \rightarrow \theta''\text{phase} \rightarrow \theta'\text{phase} \rightarrow \theta\,\text{phase}$$

The GP-zone and θ' phase are fully coherent with the matrix, whereas θ' phase is disk shaped and semi-coherent with the matrix. At this stage a peak in the hardness variation is observed. The final θ precipitate phase is almost spherical in shape and incoherent at the precipitate matrix interface. This precipitate exhibits a body centered tetragonal structure with $a = b = 0.6066$ nm, $c = 0.4874$ nm [17, 24]. Hardness of alloy decreases drastically with the formation of θ precipitates which are incoherent with the matrix. This stage is generally referred to as over–aged condition. The hardness or strength of the alloy up to the peak aged condition is higher compared to that after the solution heat treatment. The time to reach the peak hardness or strength depends on the heat treatment temperature; higher the temperature, shorter the time required. The commercial precipitation hardenable alloys are normally heat treated in the range between 120–180 °C. Depending upon the temperature and the alloy composition, the ageing time for these alloys may vary from four hours to 72 hours [6–8].

Ageing temperature and degree of supersaturation play a great role on the final properties of the alloy. The higher the ageing temperature and higher the degree of supersaturation, the hardening process will be faster. Higher temperature ageing is adopted when more stable phase is required together with dimensional stability. Besides mechanical properties, physico-chemical properties are also affected by ageing. This happens due to the metastable structure of the alloy which are formed during ageing of the supersaturated solid solution obtained by the solution treatment.

During the precipitation process, the morphology, size, distribution and mean inter-particle distance of the second phase precipitates also gets altered. The mechanical properties are controlled by the lattice coherency at the particle matrix interface, size and properties of the precipitates [3, 6].

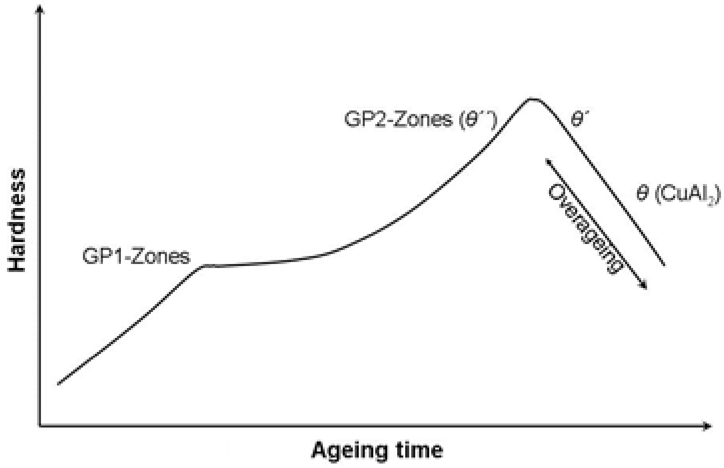

Figure 2.1 Schematic diagram showing hardness as a function of aging time at constant temperature during precipitation hardening [3]

The relation between dislocation motion and mechanical behavior is important for understanding the strengthening in metals and alloys. At micro-level, plastic deformation corresponds to the motion of a large number of dislocations. The ability of a metal to plastically deform depends on the ability of the dislocations to move. Hardness and strength signify the ability of the material to resist plastic deformation. Hence, the mechanical strength can be enhanced by impeding the movement of dislocation through the matrix [3, 6]. In the case of precipitation strengthening, the motion of dislocations is impeded by the finely dispersed brittle second phase particles precipitated in the alloy matrix.

According to Orowan theory [56], it was observed that the quantitative model explains the hardening effect during ageing. The three conditions to be fulfilled in Orowan's theory of strengthening mechanism are as follows [57]:

i. The material should have two phase microstructure; (a) the ductile continuous phase (matrix) and (b) very fine precipitates uniformly distributed in the matrix. These fine precipitates impede the motion of dislocations of the matrix.

ii. The particle diameter (d) and inter-particle spacing (S) should generally be less than 100a, where a is the atomic size.

iii. Particle needs to be strong enough to promote looping of dislocations without being sheared, for which $d_c < d$ where d_c is the critical particle diameter.

During the application of external load on a material containing uniform distribution of second phase precipitates, plastic deformation commences by movement of dislocation through the matrix. The motion of the dislocations is impeded when they encounter hard second phase precipitates. Subsequent application of external load results in piling up of a large number of dislocations near the precipitates. Since the dislocations are accompanied by stress fields, the piling up dislocations results in the stresses at the particle. The force F, which a particle can sustain, depends on its intrinsic strength and particle diameter. Two mechanisms are possible (Figure 2.2) for the movement of dislocations; *viz.* (i) dislocation cut through (shear) the particles, when strength is week and (ii) dislocation by-pass the particles resulting in a dislocation loops around the particles, when the particles are strong [57].

In the latter case, the force

$$F > \mu b^2, \tag{2.1}$$

where μ is the shear modulus of the particle and b is the Burger's vector of the dislocation. For ordered particles which are coherent with the matrix

$$F = C\gamma_{APB} d, \tag{2.2}$$

where γ_{APB} is energy of the anti-phase domains boundaries. The critical particle diameter d_c is obtained as

$$d_C = C\frac{\mu b^2}{\gamma_{APB}}, \tag{2.3}$$

where C is a geometrical factor given by the shape of the particle. For a particle non coherent with the matrix and having a high shear modulus G_β, dislocation will have to be generated in order to shear the particle. In such case, the critical diameter is very small and is given by

$$d_C = \frac{4\pi b \mu_\alpha}{G_\beta}, \tag{2.4}$$

where G_α is the high shear modulus of the matrix [57]. In case of the Al-Cu alloy system, θ'' is typically coherent with the matrix, whereas, the hard θ ($CuAl_2$) phase is the non-coherent particle. The increase of yield stress due to the dispersed particles, is given by

$$\Delta\sigma_P = \frac{\mu b}{S_{eff}} = \frac{\mu b}{S-D} = \frac{\mu b}{d} f_P^{1/3}, \tag{2.5}$$

where S spacing of the particle centers and f_P is the volume fraction of the particle in the matrix. In aluminum alloys, $S_{eff} \approx S$ for small volume fractions ($f_P \leq 1\%$). The condition $d < d_c$ limits the applicability of Eq. (5). However the relationship provides a good estimate of the strengthening that can be achieved in precipitation hardenable alloys [57].

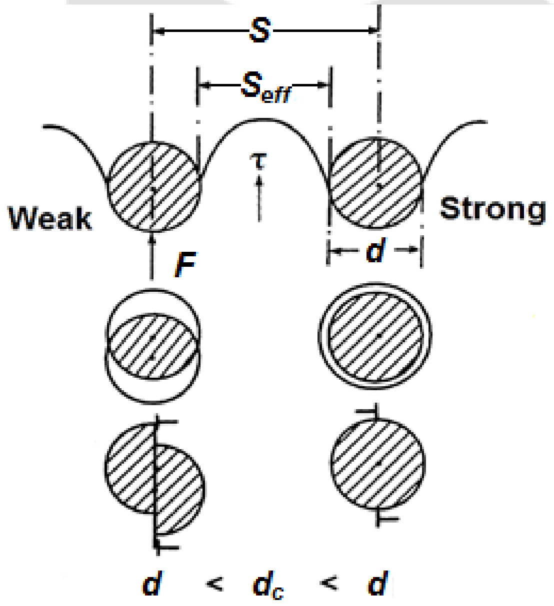

Figure 2.2 Schematic diagram force F exerted on particle by looping dislocation [57], with permission, copyright Elsevier

The Al-Cu phase diagram shown in Figure 2.3 indicates a decreasing solubility of the solute in the Al matrix. Consider a alloy of 96%Al–4%Cu. The α-phase is a single phase solid solution of Cu in Al matrix with a maximum solubility of 5.65 wt.% Cu at 548 °C. The solubility of Copper into aluminum decreases with decreases with decreasing the 550–75 °C. The precipitation hardening process involves three basic steps: solution treatment, quenching and finally aging [57]. The sequence of the process is shown schematically in Figure 2.4.

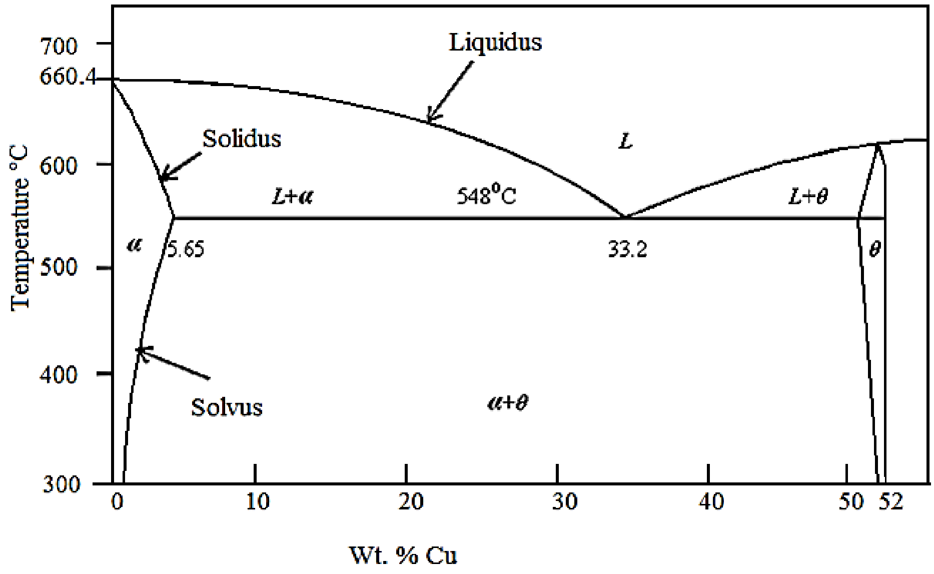

Figure 2.3 Partial Al-Cu equilibrium phase diagram [3]

Solution treatment, or solutionizing, is the first step in the precipitation-hardening process where the alloy is heated above the solvus temperature and soaked there until a homogeneous solid solution (α) is produced. During this process the copper atoms dissolves in the aluminum matrix.

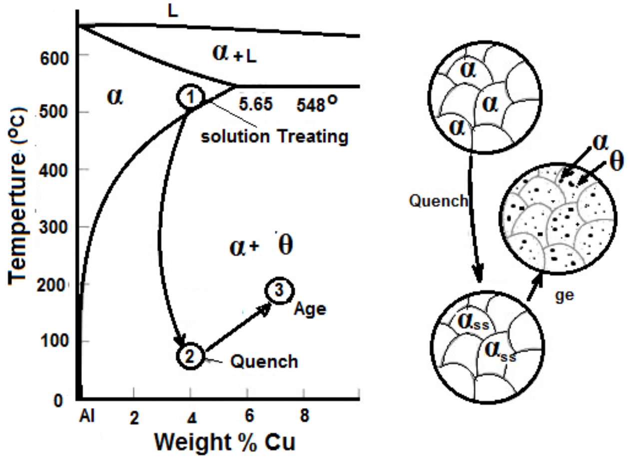

Figure 2.4 Aluminum rich end of the Al-Cu equilibrium phase diagram showing the three steps in the age-hardening heat treatment and corresponding microstructures that can be obtained [6]

Quenching is the second step where the solid α is rapidly cooled forming a supersaturated solid solution α_{ss} of copper in aluminum matrix. For precipitation hardenable alloys α_{SS} is in a metastable state. Due to the rapid water quench, the solute atoms are not able to diffuse out of the super saturated α_{SS} solution. Given sufficient energy, the extra copper atoms can diffuse out of the Al lattice. This is possible with the ageing process which is the final process of enhancing the strength of the alloy. Aging is the process where the supersaturated alloy is heated to an intermediate temperature between the solvus temperature and room temperature. These results in the diffusion of the solute from the matrix forming find precipitated phases. The solute atoms diffuse only short distances at this aging temperature. The formation of the second phase is by a process of nucleation and growth. Initially a large number of nucleating sites are available. With more and more of copper diffusing out of the lattice, the size of the particles increases. The fine precipitates in the alloy impede dislocation movement by forcing the dislocations to either cut through the precipitated particles or go around them, as shown in Figure 2.2. By restricting dislocation movement during deformation, the alloy is strengthened [3, 6, 57].

During the age hardening of Al-Cu alloys, the precipitation of second phase occurs by a sequence of four mechanisms (i) formation of solute cluster which later results in the formation of Guinier-Preston-1 (GP-1) Zones. Further aging results in (ii) formation of GP-2 Zones (also called θ''). Subsequent aging results in (iii) modification of the morphology of the precipitates to form the θ' Phase, and finally resulting in (iv) stable θ ($CuAl_2$) Phase. A large number of very small solute-rich clusters form during the early stages of the aging process that are completely coherent with the alloy lattice. Since the atomic dimensions of the solute-rich regions will differ somewhat from that of the lattice, strains occur in the lattice regions around the clusters [3, 6].

Needle shaped GP-1 zones grow rapidly from the initial clusters The sizes of GP-1 zones are typically ~10 nm thick. Hardening and a decrease in ductility accompany the formation and growth of the GP-1 zones; these effects have been attributed to the distortion of the lattice which inhibits the movement of dislocations. The needle shaped GP-1 phases transforms continuously to disc shaped and finally spherical shape (final θ phase) when the alloy is in over-aged condition. Transformation of θ' phase to θ phase is accompanied by an increase in the size of the precipitates leading to low coherency at the precipitates matrix interface. this results in a sudden drop in hardness and strength of the alloy. This stage of decrease in hardness with ageing time is referred as over ageing [3, 6].

During aging, the GP-1 zones transform to GP-2 zones having 10–100 nm diameter and 1–4 nm thickness. The strengthening process increases with transformation of GP-1 to θ'' phase and later to the θ' phase. During this process the coherency at the particle matrix interface changes from a coherent interphase to a semi-coherent interface and finally the interface becomes incoherent when the θ' phase transforms to the stable θ phase ($CuAl_2$). The θ' phase has a tetragonal structure with a different lattice parameter from the matrix; no coherency strains exist, but each particle is surrounded by a ring of dislocations. The size of the θ' phase depends on time and temperature; size ranges from 10 to 600 nm diameter with a thickness of 10–15 nm. Eventually the θ' phase is replaced by θ ($CuAl_2$) which has the same structure and composition as the θ phase formed during solidification. The formation of θ phase results in softening of the alloy and is referred to as over-aging [3, 6].

2.6 High temperature deformation behavior of wrought alloys

The wrought alloys for structural application need to undergo a thermo-mechanical treatment prior to their final use. The mechanical properties are affected by the composition, strain history and the microstructure resulting from the thermo-mechanical treatments imparted. These alloys are required to be plastically deformed to reduce the defects (*viz.* segregations, dendrite structures, gas defects, inclusions etc.) induced during casting. The deformation process is generally carried out at high homologous temperatures *i.e.*, $T/T_m > 0.5$, where T and T_m are the absolute working temperature and melting temperature of the material, respectively. In high temperature deformation, the two main research areas are (i) creep deformation, and (ii) metal forming by hot working. The major objectives in hot working are to reduce the flow stress and raise the fracture strain at high strain rates ($0.01\ s^{-1} < \dot{\varepsilon} < 100\ s^{-1}$), whereas the emphasis in creep research is for low strain rates and curtailment of total strain, even though both these studies are carried out at almost the same temperature range [27–28].

A clear understanding of the process variables and material parameters is required for successfully deforming these materials within certain range of strain rates and temperatures. The deformation behavior of these materials, which is the relationship between flow stress (σ), strain (ε), strain rate ($\dot{\varepsilon}$) and process temperature (T) is dependent on the activation energy (Q) for deformation, which is a measure of the degree of difficulty for deformation. Composition and microstructure strongly influence the Q value of the materials. Considering hot deformation similar to the creep phenomenon occurring at high strain rates and stresses [58], various constitutive relationships have been developed to model the high temperature deformation behavior of materials.

Cho et al. developed a thermo–viscoplastic finite element method (FEM) model, using hot compression test data to predict the microstructural evolution in Al–5wt.% Mg alloys during hot deformation [59]. Smith et al. proposed a unified creep–plasticity constitutive model for the stress–strain behavior of cast Al–Cu–Si [60]. Kaibyshev et al. [61] investigated the deformation behavior of a 2219 Al alloy (Al-6.4%Cu-0.3%Mn-0.18%Cr-0.19%Zr-0.06%Fe) in the temperature range from 250–500 °C. The results indicate an increase in stress exponent and apparent activation energy with decrease in temperature.

Hot and warm formability studies of solutionized 2618 aluminum alloy (Al-2.3%Cu-1.6%Mg-1.1%Fe-1.0%Ni-0.07%Ti-0.18%Si) at various strain rates and temperatures were carried out by torsion testing. The study revealed that effect of the precipitation of second phase particles are formed during deformation [62]. The flow curves indicated temperature dependent behavior with (i) a continuous increase of flow stress up to 250 °C due to precipitation, and (ii) a peak in the flow curves above 250 °C due to precipitation and coarsening of precipitates followed by softening. The high temperature tensile deformation behavior of Al-Cu-Mg-Zr alloy, 2014, and 6082 Al alloy in a wide range of temperature and strain rate were described by a modified hyperbolic sine equation, where the peak flow stress (σ_p) was substituted by an effective stress, which is the difference between peak stress and a threshold stress representing the strengthening effect of the second phase precipitates in the matrix [63, 64]. Extensive investigations of the flow stress behaviors of Al-Cu-Li-Zr, Al-Mg, Al-Cu-Mg-Ag, and Al-Mg-Si-Cu alloys were carried out by several researchers [58, 65–67]. The studies reveal that the plastic deformation of these alloys at elevated temperatures ($T > 0.5\ T_m$) is a thermally activated process. The flow stress has either an exponential or hyperbolic sine relationship with strain rate and temperature.

The Zener–Hollomon parameter, *Z*, is used for representing the hot deformation behavior of metallic alloys [31]. The constitutive relationships and the modeling procedures developed for predicting the flow stress behavior are discussed below in Section 2.6.1

2.6.1 Constitutive models

Based on the principles of creep deformation, models were developed to explain the high temperature deformation behavior of metallic materials. Similar to the creep deformation, high temperature deformation of metallic alloys is also a thermally activated process controlled by strain rate and temperature [68]. During the hot deformation, the strain rate is higher by several orders of magnitude as compared to creep deformation. Hence, the theories of hot deformation can be regarded as an extension of the creep deformation under high strain rate and at high stresses.

The initial development of the constitutive relationships was based on the assumption that the flow stress (σ) is a function of only the instantaneous values of strain (ε), strain rate ($\dot{\varepsilon}$) and temperature (T) [48, 68], *i.e.*

$$f\left(\sigma,\varepsilon,\dot{\varepsilon},T\right)=0. \tag{2.6}$$

This is analogous to the expression for a thermodynamic system in equilibrium, which can be expressed by the state variables *viz*., pressure (P), volume (V) and temperature (T), *i.e.*

$$f\left(P,V,T\right)=0. \tag{2.7}$$

It was soon realized that plastic deformation is an irreversible process, so that strain and strain rate are not state functions like pressure (P), volume (V) and temperature

(T). Instead, the flow stress depends on the dislocation structure which in turn is related to the metallurgical factors strain (ε), strain rate ($\dot{\varepsilon}$) and temperature (T) [68].

A sine hyperbolic relationship which is particularly useful for correlating stress, temperature and strain rate under hot working conditions was first proposed by Sellars and Tegart [68–69] Subsequently, a set of constitutive relations was developed [70] to analyze constant true strain rate, strain rate change, stress relaxation and creep test data. A computer representation of the constitutive relations was developed [71] for analyzing high temperature deformation.

Strain rate ($\dot{\varepsilon}$) depends on temperature (T) and activation energy (Q) for deformation by an Arrhenius type equation that can be expressed as [60, 61]:

$$\dot{\varepsilon} = A\, f(\sigma) \exp\left(-\frac{Q}{RT}\right), \tag{2.8}$$

where Q is the activation energy for deformation (J/mole), A is a constant, R is universal gas constant and $f(\sigma)$ is the stress function which can be expressed by any of the following relationships [72–78]:

$$f(\sigma) = \sigma^{n_1}, \tag{2.9}$$

$$f(\sigma) = \exp(\beta\sigma), \tag{2.10}$$

$$f(\sigma) = [\sinh(\alpha\sigma)]^{n}. \tag{2.11}$$

Combining Eq. (2.8) with Eq. (2.9), (2.10) and (2.11), the following constitutive equations can be obtained:

$$\dot{\varepsilon} = A_1 \sigma^{n_1} \exp\left(-\frac{Q}{RT}\right), \tag{2.12}$$

$$\dot{\varepsilon} = A_2 \exp(\beta\sigma) \exp\left(-\frac{Q}{RT}\right), \tag{2.13}$$

$$\dot{\varepsilon} = A_3 [\sinh(\alpha\sigma)]^{n} \exp\left(-\frac{Q}{RT}\right). \tag{2.14}$$

In the above equations, though flow stress, σ is generally taken as the peak flow stress (σ_p) [74], the steady state flow stress (σ_s) has also been used in a few instances. Flow curve at hot working conditions generally exhibits a peak flow stress (σ_p), especially when the deformation is carried out at high temperatures and low strain rates. After achieving the peak flow stress, the flow curve may start decreasing at a constant rate (flow softening) when dynamic recrystallization sets in. If the rate of strain hardening is equal to the rate of dynamic recrystallization the flow curve remains at a steady state value (σ_s). The term α is the stress multiplier used in the mathematical fitting procedure. The terms of n_1, β, n, A_1, A_2 and, A_3 are material constants. The power law equation (Eq. 2.12) breaks down at high stress values whereas the exponential equation (Eq. 2.13) breaks down at low stress values [27, 58, 67, 72, 73]. Over a wide range of stresses, the hyperbolic sine law (Eq. 2.14) is found to be most suitable form for describing high temperature deformation behavior of materials.

It has been observed in many instances that peak flow stress (σ_p) and steady state flow stress (σ_s) have a linear relationship. It has also been found that the Zener–Hollomon parameter is a useful tool in describing the high temperature deformation behavior of metallic materials [75].

2.6.2 Zener-Hollomon parameter (*Z*) and activation energy (*Q*)

The flow stress of the material σ during hot deformation can be expressed as [68, 69, 79]:

$$\sigma = \sigma\left(\varepsilon, \dot{\varepsilon}, T\right). \tag{2.15}$$

Generalized form of peak flow stress (σ_p) is possible using the Zener–Hollomon parameter *Z*. The *Z*, which correlates strain rate ($\dot{\varepsilon}$), deformation temperature (*T*), and activation energy (*Q*), can be expressed as [20]:

$$Z = \dot{\varepsilon}\exp\left(\frac{Q}{RT}\right). \tag{2.16}$$

The physical meaning of *Z* is the so called temperature-modified strain rate.
Combining Eq. (2.14) and Eq. (2.16), the expression for *Z* can be expressed as

$$Z = \dot{\varepsilon}\exp\left(\frac{Q}{RT}\right) = A_3\left[\sinh(\alpha\sigma)\right]^n. \tag{2.17}$$

The activation energy, *Q*, indicates the energy for plastic deformation and is determined from the following relationship [77–81]:

$$Q = R\left[\frac{\partial \ln \dot{\varepsilon}}{\partial \ln\left[\sinh(\alpha\sigma)\right]}\right]_T \left[\frac{\partial \ln\left[\sinh(\alpha\sigma)\right]}{\partial\left(\frac{1}{T}\right)}\right]_{\dot{\varepsilon}} \tag{2.18}$$

$$= R\, n\, S.$$

In the above relationship, n is the mean slope of $\ln(\dot{\varepsilon})$ versus $\ln[\sinh(\alpha\sigma)]$ plots obtained at different T and S the mean slope of the $\ln[\sinh(\alpha\sigma)]$ versus $(1000/T)$ plots at various strain rate $(\dot{\varepsilon})$.

Survey of the literature indicates that so far the focus has been to determine *Z*, *Q*, *α*, *n*, *etc*. of commercially available Al alloys. These parameters are known to be influenced by even small variations in the composition and microstructure of the alloys. Investigations on the effect of microalloying on the high temperature deformation behavior of the wrought aluminum alloys are still sparse.

2.7 Artificial neural network (ANN) modeling

A neural network is similar to the biological nervous system, which is basically a connectionist system, in which various nodes called neurons are interconnected [40, 82, 83]. An artificial neural network (ANN) can be defined as a model of reasoning similar to the human brain, where a large amount of complex information can be stored and processed simultaneously by each neuron along the entire domain. A typical neuron receives one or more input signals and gives an output signal that depends on the processing function of the neuron. This output is transferred as input to the adjacent connected neurons in varying intensities. The signal intensity is decided by the weights assigned. Artificial neural network has the advantages of (i) modelling the data where the input–output relation is either unknown or nonlinear, (ii) adaptive learning during training and (iii) real time applications aided by a very fast computational speed. The conventional computational techniques follow an algorithmic approach, where a set of instructions in the specified order is followed to solve a problem. The relationship between each stage is required for solving the problem. On the other hand, neural network technique is data driven and the solution can be obtained even if the exact relationship is unknown. This can be obtained if a number of input–output data sets are available. Once the artificial neural network architecture is fixed, the output for any combination of input variables can be predicted [40, 83, 84].

The most popular neural networks are feed forward networks. A feed forward network architecture consists of at least three distinct layers: the input layer, the hidden layers and the output layer. Each layer consists of a number of neurons. The output from the neurons of one layer is transferred as input to neurons of the succeeding layer. The first layer, called an input layer, receives data from the outside world. The second layer, called the hidden layer is used to help in extracting higher-level features and to facilitate generalization of outputs. Depending on the network architecture more than one hidden layer may be present. The hidden layers have no direct contact with the environment. The last layer is the output layer, which sends information out to users. For a given input vector, it generates the output vector by a forward pass. The data are fed to the network at the input layer and propagated with weights and activation functions to the output layer through the hidden layers to provide the response. Once the data at the output neuron is reached, the mean squared error (MSE), which is the difference between the network output vector and the known target vector, is computed and back-propagated through artificial neural network to modify the weights for the entire network. This process is referred to as training. Learning can be of three types: (a) supervised and (b) unsupervised or reinforced. The most popular method practiced for supervised training of neural networks is the back-propagation training algorithm. Here, the training process involves two passes. In the forward pass, the input signals propagate from the network input to the output. In the reverse pass, the calculated error signals propagate backwards through the network where they are used to adjust the weights. Any efficient optimization method can be used for minimizing the error through weight adjustment. The calculation of the output is carried out, layer by layer, in the forward direction. The output of one layer is the input to the next layer. In the reverse pass, the weights of the output neurons are adjusted first, since the target value of each output neuron is available to guide the adjustment of the associated weights. Next, the weights of the middle layers are adjusted, since the middle layers have no target values. As the errors of succeeding layers, after proper transformations, are propagated back through the network, layer by layer, this algorithm is termed as the back propagation algorithm [40, 84].

After presenting the sets of inputs and associated outputs, the network is able to learn the relationships between them by changing the weights of its connections, *i.e.* training. Once the network has been trained according to the assigned learning rule, it is capable of computing the output values associated with new input vectors. The trained neural network has to be tested by supplying testing data. If the testing error is much more compared to training error, the network is said to over-fit the data. A properly fitted network will give nearly equal training and testing errors [40, 83, 84].

During hot working process, flow stress (σ) of the material is a function of three independent parameters, and is expressed as: $\sigma = \sigma(\varepsilon, \dot{\varepsilon}, T)$ (as discussed in Eq. 2.15). This flow stress, σ of a particular material can be modeled by artificial neural network architecture, as shown in Figure 2.5. In such a network, the input layer can consist of three neurons representing the three parameters *viz.*, strain (ε), strain rate ($\dot{\varepsilon}$) and temperature (T). The output layer on the other hand consists of one neuron representing flow stress. Once the proper network architecture is determined, flow stress can be successfully predicted for any combination of the input variables within the process domain. The flow stress values thus obtained can be successfully applied to generate processing maps to determine the safe processing zones [40, 83, 84].

Traditional curve fitting techniques have been used for obtaining these processing maps [39]. Strain rate values generally used for carrying out experiments cover a range of four to five orders of magnitude. Hence, the traditional curve fitting techniques may not be appropriate for modeling such highly complex phenomena. On the other hand, neural network techniques have been found capable of learning from a data set to describe the non-linear and interaction effects with great success [85]. The advantages of neural networks are that the functional relationship between various variables can be obtained even if the form of non-linear relationship is unknown and some of the experimental data are faulty. This makes the neural network technique a robust technique for obtaining the functional relationship in any engineering problem. The application of neural network modeling in generating the processing maps for hot workability is covered in the following section. Neural network has been successfully demonstrated as a more robust technique than any other conventional methods for generating the processing maps [40, 83, 84].

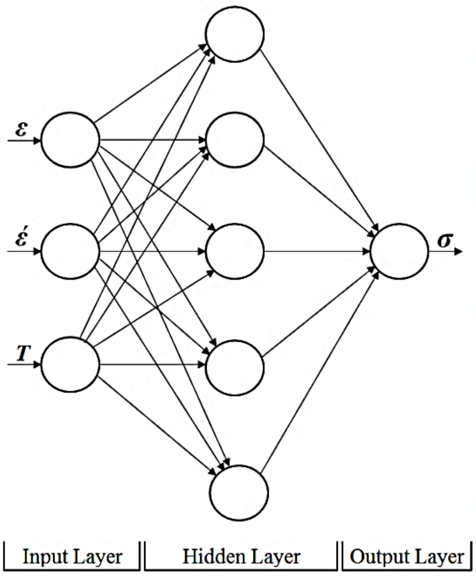

Figure 2.5 Schematic diagram of a typical neural network architecture [40], with permission, copyright Elsevier

2.8 Processing map for hot workability

'Workability' is an important parameter in mechanical working of materials, which refers to the relative ease with which a metal can be shaped through plastic deformation without the formation of any defect in it. Processing maps can express clearly the hot workability of materials. Various models developed for understanding deformation behavior of metallic alloys are as follow:

Kinetic models: The earlier developed models were of kinetic nature. Dorn used a kinetic rate equation to correlate the creep rate to the applied stress (power law creep) and temperature by the equation [86]

$$\dot{\varepsilon} = A\sigma^{n} \exp\left(-\frac{Q}{RT}\right). \tag{2.19}$$

where $\dot{\varepsilon}$ is the strain rate, A is the material constant, σ is the flow stress, n is the stress exponent, Q is the activation energy, R is the universal gas constant and T = temperature. Jonas et al. [87] reviewed the application of kinetic analysis to hot deformation and this methodology has been used extensively for several decades. On this basis, the deformation mechanism and microstructural features could be correlated with the Zener–Hollomon parameter (Z). Though the kinetic analysis were carried out for pure metals and dilute alloys, the apparent activation energy values become too complex to interpret in terms of a single atomic mechanism when used to analyze the hot deformation behavior of complex alloys. The kinetic rate equation is obeyed in the deterministic regimes of process parameters where a single rate controlling mechanism operates whereas it was difficult to interpret in the regimes where more than one mechanism operates. It is also to be noted that the kinetic analysis does not help in optimizing the hot workability [81, 82].

Atomistic mechanism maps**:** Ashby [88] developed the deformation mechanism maps to represent the materials response at high temperatures and stresses. These are plots of normalized stress versus homologous temperature where the area of dominance of each mechanism calculated using fundamental atomistic parameters are shown. The Ashby maps are very useful in predicting the creep behaviors of the alloys since the emphasis has been on the creep mechanisms applicable to lower strain rates. Hence these maps were not of much use in industrial processing of alloys where high strain rates are encountered. Considering strain rate and temperature as the variable, Raj [89] extended the concept of Ashby maps to construct processing maps. Raj considered two different fracture nucleating mechanisms and calculated the limiting conditions for avoiding the microstructural damage. These are: (i) cavity formation at hard particles in a soft matrix occurring at lower temperature and higher strain rate, and (ii) wedge cracking at grain boundary triple junctions occurring at higher temperature and lower strain rate. At very high strain rate, a regime representing adiabatic shear band formation was also included. In the Raj maps, a region termed ‘safe” could be highlighted where neither of these damage mechanisms occurs [89].

Dynamic materials modeling**:** Dynamic materials model (DMM) has been developed [37, 39, 41] for studying the workability parameter based on principles of continuum mechanics of large plastic flow using the concepts of physical systems modeling and extremum principles of irreversible thermodynamics. This model for hot deformation is expected to predict: (i) the response of the work piece material in terms of microstructural evolution, (ii) optimum process parameters without trial and error, and

(iii) process limits for controlling the manufacturing environment. Extensive reviews of dynamic material model for hot deformation behavior have been carried out by Prasad at al. [41] and Rao at al. [90]. The dynamic materials model was able to bridge the microstructural evolution in materials and principles of continuum mechanics of large plastic deformation. In this model, the work-piece is considered to have the following characteristics [39]:

1. The work piece dissipates power during hot deformation and does not store energy significantly.
2. The constitutive response of the material at a given T during hot deformation depends essentially on the $\dot{\varepsilon}$ and to a small extent on the ε, *i.e.*, the work-piece is visco-plastic.
3. The flow stress response of the work-piece to the imposed variables like ε, $\dot{\varepsilon}$ and T is non-linear.
4. The large plastic flow at high T causes irreversible changes in the microstructure of the work-piece.

The major irreversible changes in the microstructure and their salient features are as follows:

Dynamic recrystallization (DRX): The dynamic recrystallization domain generally occurs in the temperature range of 0.7–0.8 T_m and at intermediate strain rate of 0.1–1 s^{-1} for materials with low stacking fault energy (SFE) while it occurs at strain rate of 0.001 s^{-1} for high stacking fault energy materials. The maximum efficiency of power dissipation is about 30–35 % for low stacking fault energy materials, 40 % for medium stacking fault energy (SFE) metals and 50–55 % for high stacking fault energy materials [39]. Flow softening with an initial peak stress generally suggests dynamic recrystallization. However based on the material modeling and microstructural observations, similar behavior can also be interpreted due to other flow instabilities during the deformation process. The grain boundaries of the dynamic recrystallization domain are more irregular and wavy in nature. The grain size variation with $\ln(\dot{\varepsilon})$ at the dynamic recrystallization temperature exhibits a minimum at the peak efficiency. Dynamic recrystallization process refers to the nucleation and growth of new crystals during the deformation processes [42, 78, 91–

93]. Dynamic recrystallization differs from static recrystallization in the sense that dynamic recrystallization characteristics are decided by the rate of nucleation versus rate of growth under given conditions of strain rate and temperature. In static recrystallization on the other hand, a fixed amount of stored energy, depending on cold work, is released by thermally activated process. The nucleation during dynamic recrystallization consists of the formation of grain boundary due to dislocation generation and simultaneous recovery. The growth of the nucleus is by grain boundary migration. When nucleation and growth occur simultaneously, the one with slower rate controls dynamic recrystallization. Dynamic recrystallization is a beneficial process in hot deformation since it gives the stable flow and good workability to the material by simultaneous softening and reconstituting the microstructure [94, 95]. Dynamic recrystallization is a chosen domain for optimizing hot workability and controlling the microstructure and is accepted as a safe domain for bulk metal working [39].

Dynamic recovery: Thermal recovery of dislocations due to their climb causes dynamic recovery that occurs generally in the homologous temperature range of 0.4–0.6 and is thus relevant to warm working of materials. The dynamic recovered microstructure has well defined sub-grains with relatively dislocation free interiors. Dynamic recovery causes work hardening of the material, the rate of which is lower than that obtained in cold working

Adiabatic shear bands: During deformation at higher $\dot{\varepsilon}$, local temperature rise in the workpiece may occur especially due to lack of sufficient time to dissipate the heat generated. This results in nonhomogeneous deformation in the form of localized shear bands. The flow localization results in a decrease in σ. The shear bands thus formed get intensified under adiabatic conditions [96–97]. The adiabatic shear bands occur at an angle of 45° with respect to the applied stress axis. Under intense conditions, these may result in internal cracks along these shear bands.

Void formation: Void formation at hard particles simultaneously becomes predominant at high strain rate and low temperature [39, 89, 98]. If hard particles are present in a soft matrix, deformation causes voids to nucleate at the particle-matrix interface by debonding or by particle fracture. This ultimately leads to the microstructural damage in the work piece.

Intercrystalline cracking: This feature is generally encountered at higher temperature and higher strain rate. The fast propagation of cracks along the grain boundaries results in intercrystalline cracking. This may be due to the segregation of low melting phases/compounds at the grain boundaries. Adiabatic temperature rise at higher $\dot{\varepsilon}$ may aggravate cracking by incipient melting [39].

Wedge cracking and super plasticity: Superplasticity and wedge cracking are two irreversible phenomena that can occur at temperatures in the range of 0.7–0.8 T_m and at $\dot{\varepsilon} < 0.01$ s^{-1}. Both processes are characterized by high efficiency of power dissipation (> 60 %) and a steep rise of efficiency with decrease in strain rate. During wedge cracking, which is the zone identified at lower strain rate and higher temperature, grain boundary sliding occurs under shear stress. Wedge cracks are produced at triple junction points to relieve the stress concentration [39]. If the strain rate is so high that the matrix deforms at a rate faster than the rate at which the boundaries can slide, then the sliding effect would be negligible, thereby preventing wedge cracking. However, at lower strain rate, there is enough time to relax the high stress at the triple junctions. Wedge cracking may be identified by microscopic observation of the grain boundary triple junctions particularly in the area of the specimen where a tensile component of the stress occurs (*e.g.* bulge region of a compression specimen).

Materials with stable fine grained structure when deformed at low strain rate and high temperature exhibit abnormal elongations and the process is called superplasticity [99]. If the stress concentration is relieved by diffusion aided flow, superplasticity occurs [39].

The above mentioned damage processes are sometimes very efficient in dissipating power for the generation of new surfaces. On the other hand, the safe processes become less efficient, because power dissipates through annihilation of dislocations. However, dynamic recrystallization holds a higher efficiency than dynamic recovery [98].

True stress and true strain (flow stress) curves provide information related to the mechanisms of hot deformation. Different ‘safe’ and ‘damage’ mechanisms occur at various combinations of strain rate and deformation temperature. The safe mechanisms comprise dynamic recovery occurring at lower temperature and strain rate and dynamic recrystallization occurring at higher temperature and intermediate strain rate [98]. Among the above mentioned mechanisms, the superplastic deformation is also considered to be safe while the others are to be avoided during hot deformation. However, for optimizing hot workability and controlling the microstructure, dynamic recrystallization is a chosen domain.

Flow behavior and processing maps

The general expression of flow stress (σ) at constant strain (ε) and temperature (T) can be represented by:

$$\sigma = K\dot{\varepsilon}^{m}\Big|_{\varepsilon,T} . \tag{2.20}$$

where K and m are materials constants. A typical plot of ln(σ) versus ln($\dot{\varepsilon}$) at constant temperature is shown in Figure 2.6.

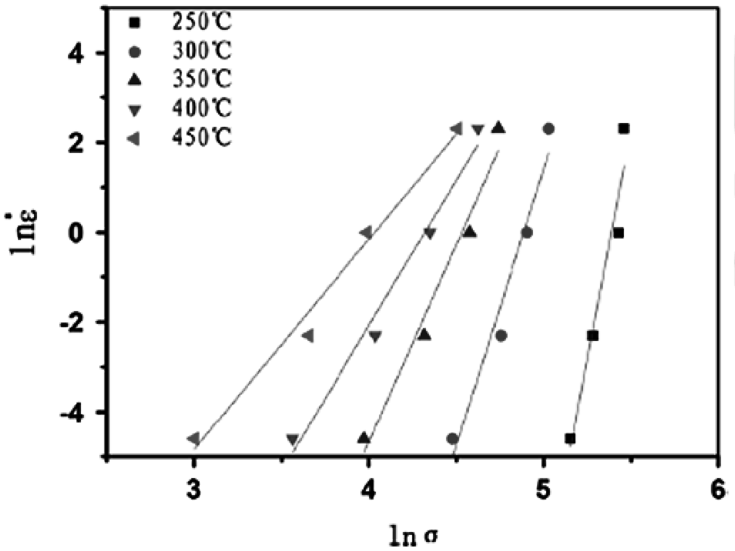

Figure 2.6 Plots of ln $\dot{\varepsilon}$ versus ln σ_p at constant temperature, for an Al-Cu alloy [30], with permission, copyright Elsevier

The term m, (strain rate sensitivity), is expressed by:

$$m = \left.\frac{\partial \ln \sigma}{\partial \ln \dot{\varepsilon}}\right|_{\varepsilon, T} . \tag{2.21}$$

Values of strain rate sensitivity (m) lie between 0 and 1, for a stable material flow. However, a close examination of the experimental data would reveal that m is different at different values of $\dot{\varepsilon}$ values. The power dissipated per unit volume is given by [39, 97] :

$$P = G + J = \sigma \dot{\varepsilon}, \tag{2.22}$$

where G and J are the dissipater content and dissipater co-content, respectively, given by the following equations:

$$G = \int_0^{\dot{\varepsilon}} \sigma \, d\dot{\varepsilon}, \tag{2.23}$$

$$J = \int_0^{\sigma} \dot{\varepsilon} \, d\sigma. \tag{2.24}$$

The maximum value of dissipater co-content can be expressed as:

$$J_{\max} = \frac{1}{2} \sigma \dot{\varepsilon}. \tag{2.25}$$

The schematic representation of G content, J co-content and $J_{\max}$ is shown in Figure 2.7. The efficiency of power dissipation (η) can be defined as

$$\eta = \frac{J}{J_{\max}}. \tag{2.26}$$

If strain rate sensitivity (m) is considered as constant corresponding to its value at limiting strain rate, J can be obtained from the following expression:

$$J = \frac{m \sigma \dot{\varepsilon}}{m+1}. \tag{2.27}$$

The efficiency of power dissipation according to the DMM model [44] is

$$\eta = \frac{2m}{m+1}, \tag{2.28}$$

Efficiency was directly computed by calculating J by numerical integration [44, 96], where the assumption of m as a constant term with respect to strain rate is not required. The efficiency of power dissipation can be obtained from the flow stress as

$$\eta = \frac{J}{J_{\max}} = \frac{P-G}{J_{\max}} = 2\left(1 - \frac{1}{\sigma\dot{\varepsilon}}\int_0^{\dot{\varepsilon}} \sigma\, d\dot{\varepsilon}\right), \tag{2.29}$$

The above integral in Eq. (2.33) can be split and expressed as

$$\begin{aligned}\int_0^{\dot{\varepsilon}} \sigma\, d\dot{\varepsilon} &= \int_0^{10^{-3}} \sigma\, d\dot{\varepsilon} + \int_{10^{-3}}^{\dot{\varepsilon}} \sigma\, d\dot{\varepsilon} \\ &= \left(\frac{\sigma\dot{\varepsilon}}{m+1}\right)_{\dot{\varepsilon}=10^{-3}} + \int_{10^{-3}}^{\dot{\varepsilon}} \sigma\, d\dot{\varepsilon}.\end{aligned} \tag{2.30}$$

Ziegler at al. [101] applied continuum mechanics principles for large plastic flow, which was used by Kumar [102] to arrive at the following metallurgical instability criteria:

$$\xi\left(\dot{\varepsilon}\right) = \frac{\partial \ln\left(\frac{m}{m+1}\right)}{\partial \ln \dot{\varepsilon}} + m \leq 0. \tag{2.31}$$

The parameter $\xi(\dot{\varepsilon})$ is evaluated as a function of temperature and strain rate to obtain an instability map, indicating metallurgical instability during plastic flow occurring at regimes where its values are negative.

The procedure of generating processing maps and their interpretations have been discussed in detail in the literature [39]. These maps can be generated from hot compression tests data acquired at constant strain rate under isothermal conditions. A processing map is an explicit representation of the response of the material in terms of microstructural mechanisms, to the imposed process parameters. It is obtained by the superimposition of a power dissipation map and instability map developed on the basis of dynamic materials model [39, 44].

In a power dissipation map, the efficiency of power dissipation is plotted as a function of temperature and strain rate at a particular true strain value. It exhibits various domains in which specific microstructural mechanisms occur. The efficiency map itself represents the power transactions within a continuum and the understanding of its origin and its interpretation in terms of atomistic mechanisms requires a correlation with the concepts of irreversible thermodynamics. It helps in interpreting the microstructures resulting from hot deformation as 'dissipative' and characterizes them in terms of atomistic mechanisms. Instability map separates out the regions of stable and unstable flow.

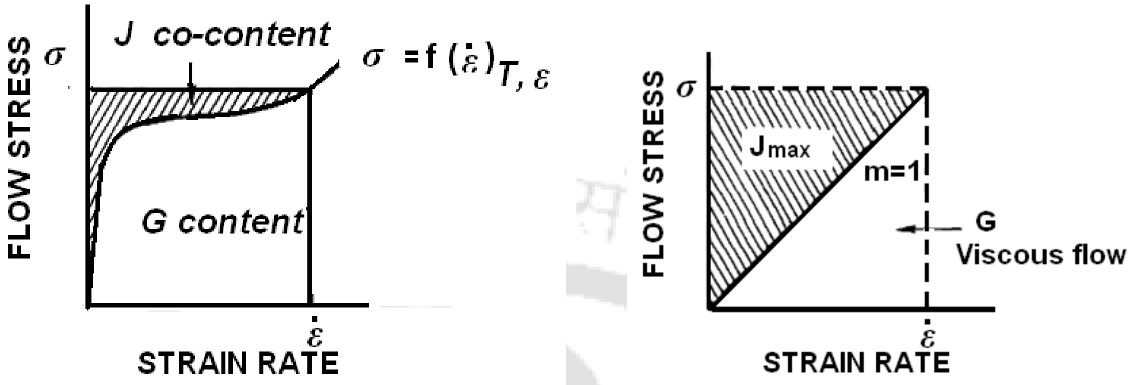

(a) (b)

Figure 2.7 Schematic representation of (a) constitutive equation in a non-linear power dissipater and (b) ideal linear dissipater [37], with permission, copyright Springer

Industrial metal working processes require the information provided by the processing maps. For newer materials, the process can be designed to suit the constitutive requirements of the material from the viewpoint of optimum workability and microstructural control. In addition, these maps can be used to optimize existing processes that can help to improve the product quality and yield. Defects arising during hot deformation processing can be avoided with the knowledge of the limiting temperature (T) and strain rate ($\dot{\varepsilon}$) conditions, which lead to the flow instabilities.

Processing maps for a large number of metals, alloys, intermetallic and metal matrix composites have been systematically compiled along with a summary of metallurgical interpretations [39]. Maps have also been generated for TiAl/TiB_2 composites by Zhao et al. [102], microalloyed steel by Omar et al. [103] and rolled aluminum [104].

Various structural defects arising in 2124 Al alloy produced by powder metallurgy technique at different deformation conditions have been studied. Flow instability in this alloy arising from adiabatic shear band formation and matrix cracking has been observed [105]. In a study of Al with different purities in the temperature range of

250–600 °C, dynamic recrystallization was observed to occur at a particular strain rate ($\dot{\varepsilon}$), while the dynamic recrystallization temperature increased with decrease in the purity level of aluminum [98]. Al–4Mg alloy exhibited wedge cracking when deformed at $\dot{\varepsilon} < 0.2\ s^{-1}$ and $T > 650$ K [106]. 6061 Al alloy composite reinforced with 20% Al_2O_3 was investigated to evaluate the efficiency of forging process by generating processing maps [107]. The power dissipation efficiency, instability regimes, shear band formation and other structural defects have been investigated for various Ti alloys at various deforming conditions. These include the studies on forged Ti-6242 titanium alloy and commercially pure titanium (Ti) [44, 108]. However, only a few reports are available on the effect of alloying elements and the corresponding microstructural changes occurring in Al alloys during hot deformation. Addition of Erbium was observed to restrain recrystallization in Al–5.7Mg alloy [109]. The apparent activation energies estimated for the two domains of dynamic recovery suggested cross-slip of dislocation and lattice self-diffusion as the deformation mechanisms. Yang Sheng et al. [110] while investigating the flow stress behavior and processing map of Al-Cu-Mg-Ag alloy observed two optimum domains for hot deformation at different ε, including the high strain rate domain between 623–773 K and the low strain rate domain in the 573–673 K range. Investigations on the hot deformation behavior of Al-Mg-Si-Cu alloys revealed dynamic flow softening resulting from dynamic recovery and dynamic recrystallization [38]. Microstructural characterization of hot deformed Al-Cu-Mg-Ag alloy revealed that with decreasing Z value, the subgrain size increased, dislocation density decreased and the major softening mechanism got transformed from dynamic recovery to dynamic recrystallization [66].

Very few studies have been reported on the different mechanisms of high temperature deformation behavior correlated with kinetics of dislocation generation and annihilation, nucleation of new phases and zones, precipitation growth or recrystallization for some commercial 2xxx series Al alloys like 2219 and 2618 [61–62].

Literature reveals several studies on power dissipation maps and instability maps of some commonly used aluminum alloys. However, processing maps for Al–Cu–Mg alloys microalloyed with additive elements have not been generated so far. Since these alloys have considerable industrial applications, these maps are important.

2.9 Detailed Objectives

From the literature it is observed that the mechanical properties of Al-alloys are affected by even small variation in compositions and microstructure. Though the effects of alloying elements on commercial alloys have been well documented, the compositions studied are generally with higher concentrations. The limited reports on micro alloying of Al-alloys are mainly investigating the microstructure and/or limited mechanical properties and precipitation strengthening. A detailed study by systematically varying the amount of trace quantity (approximately < 0.1 wt.%) of alloying elements in commercial alloys are still very few. From the report it appears that addition (≥ 0.3 wt.%) of silver will have better influence on the structure and mechanical properties of the precipitation hardenable Al alloys. There is a need to investigate (≤ 0.1 wt.% silver) the microstructural evolution, precipitation behavior, and mechanical properties of Al-Cu alloys microalloyed with silver (≤ 0.1 wt.% silver) under different processing conditions. For the use of these materials the high temperature deformation characteristics of these microalloyed Al-Cu alloys are also to be investigated to identify the exact deformation conditions.

From the limited literature available, it appears that the following areas are worth investigating:

- Influence of trace additions of silver (Ag) on the microstructure and mechanical properties of the Al-Cu alloys cast, rolled and different heat treated conditions.
- Effect of silver (Ag) addition on the age hardening conditions required to achieve peak hardness of the alloy.
- Effects of silver (Ag) addition on the high temperature behavior of the Al-Cu alloys.
- Constitutive analysis and modeling of flow characteristics of Al-Cu alloys microalloyed with silver (Ag).
- Computational modeling and prediction of flow stress by artificial neural network (ANN) technique of the relevant alloys.
- Generation of processing map for these microalloyed Al-Cu alloys.

Accordingly, detailed objectives of the present study are as follows:

1. To process the precipitation hardenable wrought aluminum alloys microalloyed with different amounts of silver (~ in the range 0 to 0.1) by a casting route.
2. To study the microstructures and mechanical properties in the cast, solutionized and rolled conditions.
3. To optimize the age hardening conditions required to achieve peak hardness value.
4. To study the effect of silver (Ag) addition on the high temperature deformation behavior of the investigated alloy system.
5. To generate constitutive models for modeling the high temperature deformation behavior and predicting peak flow stress of the alloy with varying silver (Ag) contents at different deformation conditions.
6. To generate a model for predicting the high temperature the flow stress (σ) of the material as a function of strain (ε), strain rate ($\dot{\varepsilon}$), temperature (T) and concentrating of all by artificial neural network (ANN).
7. To generate processing maps for the alloys with different trace contents of silver (Ag).

Chapter 3

Methodology

The experimental methodology followed for meeting the objectives of the thesis work is presented in this chapter. This includes details regarding the preparation of 2219 aluminum alloys by casting technique, secondary processing, heat treatments, microstructural characterization, thermal analysis and mechanical property evaluation. The methodology of artificial neural network (ANN) modeling for determination of flow stress during hot deformation, generation of deformation mechanism maps and development of constitutive equations for hot deformation are also presented in the subsequent sub-sections.

3.1 Processing of alloys

2219 aluminum alloys containing trace amounts of silver were prepared by casting technique. Details of the casting, rolling and heat treat are described in this section.

3.1.1 Casting process

Five alloys with different amounts of silver up to 0.1 wt.% were processed and cast to obtain 21 mm diameter × 200 mm long cylindrical rods and 300 mm × 100 mm × 10 mm rectangular slabs. From each alloy melts, 16 numbers of cylindrical rods and 2 numbers of rectangular slabs were obtained. The casting process involves pattern making, mold making, melting and casting and is described in the following paragraphs.

3.1.1.1 Pattern making

The pattern material for the cylindrical rods was made out of wood. The pattern consists of an assembly of 8 cylindrical rods, pouring cup, down sprue, sprue base and runner as per the general principles of pattern design [111–112]. Figure 3.1 shows the schematic diagram, photograph of wooden pattern assembly and mold of the vertical split pattern assembly designed and fabricated for the present work. The mold for obtaining rectangular alloys slabs were machined from mild steel for the preparation of the rolling sample.

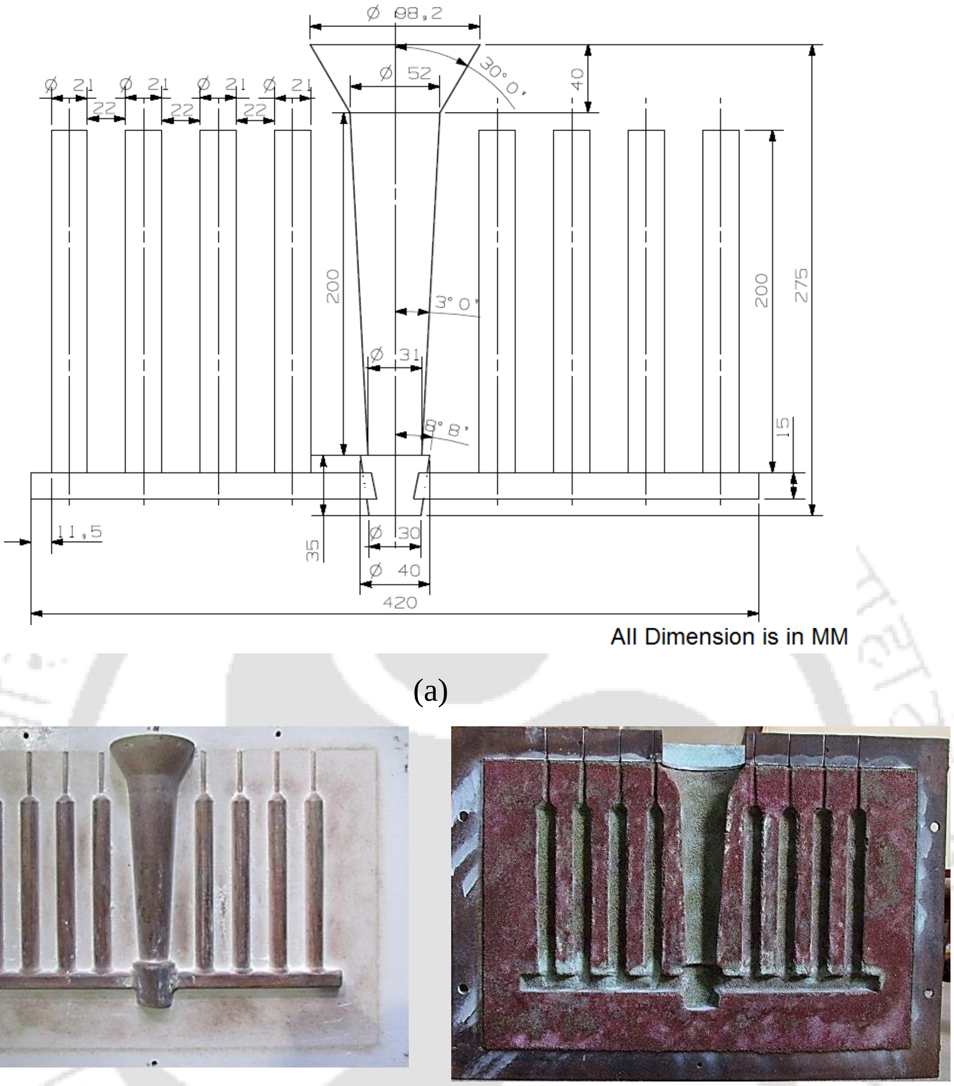

(a)

(b)

(c)

Figure 3.1 Molding design: (a) schematic diagram of pattern assembly, (b) photograph of the wooden pattern assembly and (c) photograph of the sand mold

3.1.1.2 Preparation of sand mold

The cylindrical rods were cast into sand molds, which were prepared by No-bake process [111]. The binder used for the No-bake process was a phenol formaldehyde with paratoluene sulphuric acid as the catalyst. The sand mold preparation consisted of the following sequence:

- Sand mixture used for the present work was silica sand passing through sieve of US series number 30 and retained on number 70. For each mold 22 kg of sand mixture was used.
- The molding board was placed on the table. The pattern and molding flasks were properly aligned in position and clamped properly.
- Initially 250 g of catalyst (paratolune salphonic acid) was thoroughly mixed with 22 kg of the silica sand for around 4 minutes.
- Subsequently, 500 g phenol formaldehyde resin was added to the sand-catalyst mixture and again mixed thoroughly for another 2 minutes.
- The molding sand mixture was introduced into the molding flask and rammed gently to ensure uniform filling as per the standard molding practice.
- The sand mold along with the pattern was then allowed to cure for 2 hours to obtain sufficient mold strength. The pattern was then removed to obtain one part of the split mold.
- The second part of the split mold was also prepared by the same procedure.
- Commercially available alcohol based zircon paint was sprayed on the mold surface to ensure reasonably good surface for the castings. After 4 hours of drying the two halves of the molds were assembled and were ready for pouring of molten metal.

3.1.1.3 Casting process

2219 Al-alloys (Al-Cu-Zn-Fe-Mg-Mn-Ti) microalloyed with different amounts of silver were prepared by casting technique. Alloy processing includes preparation of the master alloys and the final alloy preparation.

The starting materials for the present investigation were aluminum–1100 alloy (99% pure) ingot, IACS grade copper rod and sterling silver (92.5% pure). Prior to the alloy preparation, Al-42 wt.% copper (Cu) and Al-5.8 wt.% silver (Ag) master alloys (1 kg melt level) were prepared by melting followed by solidification in metal ingots. The melting temperatures of commercially pure aluminum, copper and silver are 660 °C, 1082 °C and 961.8 °C respectively. It was therefore necessary to make master alloys of Al-Cu and Al-Ag for obtaining Al-Cu-Ag melt with uniform composition.

Melting was carried out in a 25 kg capacity resistance heated melting furnace. The melt charge was 12.5 kg. The required quantities of the commercially pure aluminum (Al) ingot and Al-Cu master alloys as per the required alloy compositions were placed inside a clay graphite crucible kept inside a resistance heating melting furnace and heated up to 700 °C. The melt was then stirred thoroughly for obtaining molten metal with uniform chemical composition. The dross formed at the top of the molten metal was removed. This was followed by degassing of the molten metal using 0.5% degasser tablet kept in a stainless steel strainer and stirred for few minutes. This was to ensure complete removal of any gases dissolved in the molten metal. The dross formed during the degassing was also removed. The required quantity of Al-Ag master alloy was added into the melt and stirred slowly by a stainless steel rod to obtain a uniform homogeneous alloy composition. Pouring of the molten metal into molds were carried out at a temperature of 700±5 °C and allowed to solidify in the molds. After cooling to room temperature, the molds were opened and the castings were taken out. Figure 3.2 shows photographs of the mold assembly and casting obtained.

Five alloy compositions of 2219 aluminum alloy containing varying amounts of silver were prepared for the present work. Table 3.1 presents the details of the raw materials used for the alloy melting. The cast alloys were subjected to different thermo-mechanical processes. Table 3.2 illustrates the details regarding different thermo-mechanical processes imparted to the alloys.

The cast alloys were homogenized at 510 °C for 10 hours to obtain homogeneous composition by reducing segregation and coring formed during the solidification process. The heat treated samples were furnace cooled. The chemical compositions of the five alloys were then determined by atomic absorption spectrophotometer (AAS). Figure 3.3 shows the photograph of the atomic absorption spectroscopy (AAS) (Make: Varian Spectra Duo) used for the present analysis.

3.1.2 Rolling of alloys

The cast rectangular slabs were cut and machined to size 100 mm ×30 mm × 8 mm bars for rolling. These were then homogenized at 510 °C for 10 hours followed by

Table 3.1 The alloy designation and the details of melting

Sl No.	Alloy designation	Target value of silver content (wt.%)	Weight of pure Al ingot (kg)	Weight of Al-Cu master alloy (kg)	Weight of Al-Ag master alloy (g)
1	Alloy A	0	10.66	1.84	00.0
2	Alloy B	0.04	10.56	1.84	87.0
3	Alloy C	0.06	10.53	1.84	130.0
4	Alloy D	0.08	10.48	1.84	173.0
5	Alloy E	0.10	10.44	1.84	218.0

Figure 3.2 Photograph of the alloy after sand casting

Figure 3.3 Photograph of the atomic absorption spectrophotometer (AAS)

Table 3.2 Details regarding various processing techniques and characterization

Process designation	Processing conditions	Characterization / properties determined
I	Preparation of Al-Cu and Al-Ag master alloys.	Chemical composition analysis.
II	Preparation of cast (2219 Al + Ag) alloys by casting technique.	Microstructure studies, Mechanical property evaluation
III	Cast alloys homogenized at 510 °C for 10 hours followed by furnace cooling.	Chemical composition analysis of the cast alloys,
IV	Cast alloys solutionized at 525 °C for 10 hours followed by water quenching.	Microstructure studies, Mechanical property evaluation, DSC analysis
V	Process–III followed by hot compression tests at various temperatures and constant strain rates.	Flow curve determination and microstructure study for identifying mechanism of instability.
VI	Process–IV followed by age hardening at 150 °C for up to 55 hours.	Microstructure studies, Mechanical property evaluation.
VII	Cast alloys (rectangular shape) homogenized followed by warm rolling. Temperature 230–250 °C, reduction from 8 mm to 4 mm thickness (5 passes).	Microstructure studies, Mechanical property evaluation.
VIII	Process–VII followed by solutionizing at 525 °C for 10 hour and water quenching.	Microstructure studies, Mechanical property evaluation
IX	Process–IX followed by age hardening at 150 °C for up to 45 hours.	Microstructure studies, Mechanical property evaluation

furnace cooling. The homogenized alloy bars were then heated to 250 °C and soaked for 1 hour and immediately rolled to obtain 4 mm thick rectangular bars. The rolling process was carried out in a two high rolling mill (Figure 3.4). Final thickness was achieved after 6 passes. Between each passes, the samples were again soaked at 250 °C for 1 hour. After the final rolling pass, the samples were water quenched to obtain the rolled microstructure.

Figure 3.4 Photograph of the rolling mill

3.1.3 Heat treatment of alloys

The heat treatment processes (process III, IV, VI, VIII and IX) enumerated in Table 3.2 was carried out using a resistance heated muffle furnace. Figure 3.5 shows the photograph of the muffle furnace used for the heat treatment. The Furnace temperature was heated at a rate of 8 °C/minute to the set temperature. During soaking, the temperature was controlled within ± 1 °C till completion of heat treatment. After soaking at the set temperature for the required period, the samples were cooled to room temperature depending upon the process mentioned in Table 3.2.

Figure 3.5 Photograph of the muffle furnace used for heat treatment

3.1.4 Optimization of age hardening process.

Discs of 8 mm thick were sliced from the cast alloys. These were than solutionized at 525 °C for 10 hours followed by water quenching to room temperature. The quenched samples were subsequently age hardened at 150 °C (process-VI) in an oven for a period of up to 55 hours. During the age hardening heat treatment, samples were taken out at 5 hours interval and metallographically polished. The Vickers hardness values of the samples aged for the different time period were measured and time to reach to the peak hardness for each alloy was determined.

3.2 Microstructural characterization of alloys

Microstructural characterization of the alloys was carried out for the different conditions (process-II to process-IX) enumerated in Table 3.2. Samples were prepared by standard metallographic procedure and observed under both optical and scanning electron microscopes, to determine microstructural features, grain sizes, different phases present in the grain boundaries and their compositions. The detailed procedures followed are given below.

3.2.1 Metallographic sample preparation

Samples of dimension 10 mm × 10 mm were sectioned using precision saw (Buehler, ISOMET 4000). The sliced samples were mounted in thermosetting resin using a hot mounting press (Make: Buehler, SimpliMET 2). The mounted samples were then polished using a variable speed grinder-polisher (Buehler, Automet-250). Grinding was carried out using SiC coated papers of various grit sizes (240, 320, 400 and 600) in a progressive sequence. Subsequently, wet cloth polishing was carried out using Silvo polishing solution (Make: Reckitt Benckiser) as the abrasive medium, which was diluted with distilled water. The samples were then ultrasonically cleaned in water, dried and preserved in a vacuum desiccator. Figure 3.6 shows the photograph of the precision saw, mounting press and grinder polisher.

3.2.2 Optical microscopic (OM) investigation

The metallographically polished samples were etched using Keller’s reagent by immersing the sample in the etchant for 8–15 seconds. This was carried out to reveal the grain boundaries and different phases present in the alloy matrix. The chemical composition of the Keller’s reagent used for etching purpose is given in Table 3.3. The samples were then washed in running water and dried.

The polished and etched specimens were observed under an upright optical microscope, Carl Ziess, Axiotech equipped (Figure 3.7) with Axiovision Release 4.2 image analysis system. The morphology of different phases present were studied and its qualitative analysis was carried out. The grain size for each sample was determined by the standard line intercept method.

3.2.3 Scanning electron microscopic (SEM) investigation

The polished samples under the unetched conditions were observed under a scanning electron microscope (SEM, Leo, 1430 VP) under an accelerating voltage range of 10 kV. A few images were also studied using a Field Emission Scanning Electron Microscope (FESEM Make: Zeiss, Model : Sigma). Images were observed

Table 3.3 The chemical composition of Kellar’s reagent [113]

Chemical reagent (concentration)	Percentage composition in every 100 ml reagent (in ml)
Hydrofluoric acid (48%)	1.0
Hydrochloric acid (35%)	1.5
Nitric acid (70%)	2.5
Distilled water	95.0

(a)

(b)

(c)

Figure 3.6 Photographs of (a) precision saw, (b) mounting press and (c) grinder polisher under secondary electron (SE) mode. The composition of different phases present were analyzed using an energy dispersive X-ray spectrometer (EDS, Oxford) attached to the microscopes. The EDS analysis was carried out using high purity cobalt as the reference standard. The surfaces of the samples failed during the tensile loading were also observed under field emission transmission electron microscopic (FESEM) (Figure 3.8) to investigate the fracture mode.

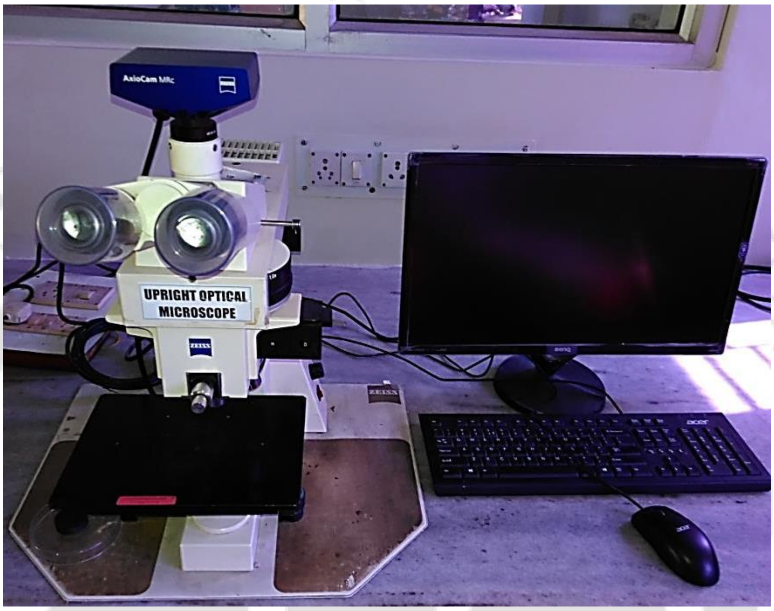

Figure 3.7 Photograph of upright optical microscope

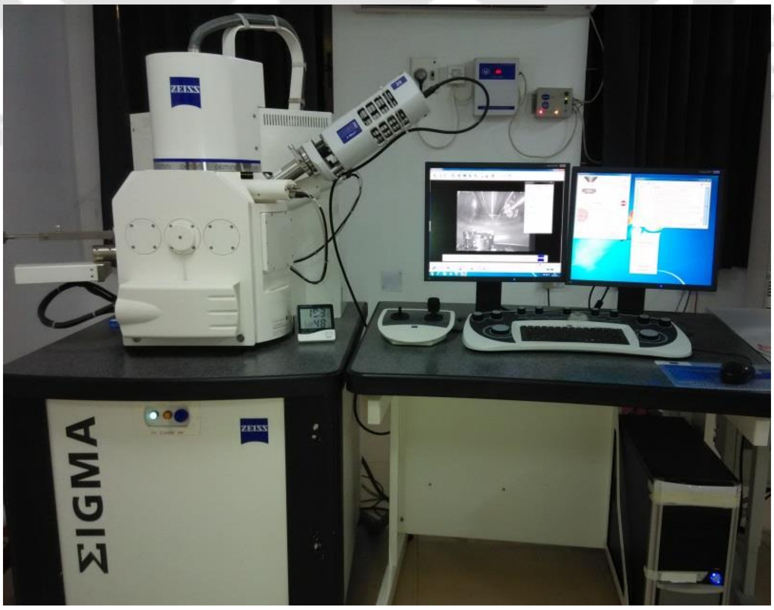

Figure 3.8 Photograph of field emission scanning electron microscope

3.2.4 Field emission transmission electron microscopic (FETEM) investigation

Transmission Electron Microscope (TEM) sample of 0.3 mm thickness was sliced using a precision saw. These were then mechanically polished to obtain 50–80 μm thick foils. Standard specimen of 3 mm diameter was punched out from these foils. These samples were further thinned by twin jet electro-polishing (Make:Fischione Instruments, Model:110) technique using an etchant of 20 vol.% sulfuric acid and 80 vol.% methanol at a voltage of 10 V and 20 mA current at temperature –5 °C. The microstructure of the samples was investigated using Jeol JEM-2100F Field Emission Transmission Electron Microscope (FETEM) attached with an energy dispersive X-ray spectroscope (EDS) and operated at an accelerating voltage of 200 kV. Figure 3.9 and Figure 3.10 are showing the photographs of Field Emission Transmission Electron Microscope and twin jet electro-polishing machine respectively.

Figure 3.9 Photograph of the field emission transmission electron microscope

3.3 Mechanical properties of the alloys

The hardness and tensile properties of the alloys under various process conditions were investigated. The procedure is described in the subsequent sub-sections.

Figure 3.10 Photograph of the twin-jet electro-polisher

3.3.1 Hardness testing

For determining the hardness of the alloys, the sample surfaces were given a mirror finish by dry polishing. The hardness of the samples was determined using Vickers hardness tester (Figure 3.11). Hardness testing was carried out using a diamond pyramid indenter (with 136° included angle) under a constant load of 10 kg applied for 10 s. The diagonal lengths of the square-shaped impression formed in the indention process were measured and the Vickers hardness number (VHN) was determined using the following relation [48]:

$$VHN = \frac{1.854F}{D^2}, \tag{3.1}$$

where F is the applied load in kg and D is the arithmetic mean of the two diagonal lengths of the indentation in mm. The hardness values presented in this thesis are the average of 10 independent indentations under identical loading conditions.

3.1.2 Tensile testing

Tensile testing of the cast as well as rolled alloys was carried out using both cylindrical and flat samples. ASTM standards [114] were followed to prepare the both cylindrical and flat tensile samples. The cylindrical tensile samples having 6 mm gauge diameter were machined from the cast and cast heat treated cylindrical rods i.e. cast, cast + solutionized and cast + solutionized + precipitation hardened rods. Also flat tensile samples were prepared from the rolled and rolled-heat treated alloys i.e.

rolled, rolled + rolled and solutionized + solutionized + precipitation hardened strips. The geometries of the flat and cylindrical tensile specimens are shown in the Figure 3.12.

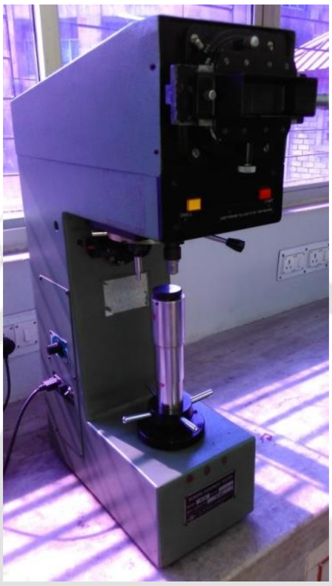

Figure 3.11 Photograph of the vickers hardness tester

Uniaxial tensile tests were performed using a 100 kN capacity servo-hydraulic controlled dynamic universal testing machine (UTM, Instron, 8801) shown in Figure 3.13. Tests were carried out with a constant actuator speed of 0.5 mm/min. A 25 mm gauge length extensometer was used to measure the displacement across the gauge length during the test. The load versus displacement data during the tensile testing was obtained and recorded. From this plot the tensile properties viz., yield strength (YS), ultimate tensile strength (UTS), percentage elongation (% El.), and Young's modulus (*E*) were evaluated. The yield strength was determined by the 0.2 % offset strain method.

3.4 High temperature compression test

The as-cast alloy rods were homogenize annealed at 510 °C for 10 hours to reduce the defects like coring and segregation, which were expected during the casting process. Cylindrical compression specimen of 10 mm diameter and 15 mm height were then machined from these rods. Two concentric circular grooves of 0.2 mm depth were machined on the two parallel surfaces of the compression specimen for adding lubricants. Uniaxial compression tests were carried out at different temperatures and constant true strain rates, using a dynamic 100 kN capacity universal testing machine (make: INSTRON, Model: 8801).

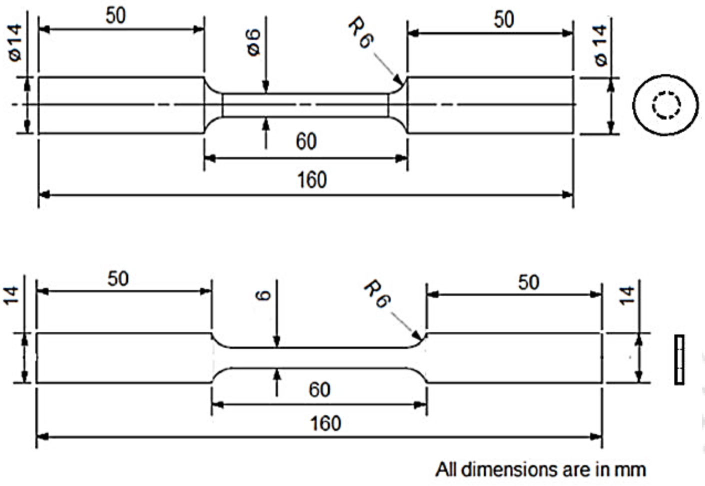

Figure 3.12 Schematic drawing of the flat and cylindrical tensile specimens [114]

Figure 3.13 Photograph of 100 kN capacity servo-hydraulic controlled dynamic universal testing machine

Prior to the test, the samples were heated to the test temperature inside a resistance heated split furnace attached to the testing machine shown in Figure 3.14. The specimen was then soaked at the test temperature for further 15 minutes to ensure uniform temperature across the specimen volume. The temperature of the sample was controlled precisely within ± 3 °C using a Eurotherm temperature controller. MoS_2

paste was applied at the work piece-compression platen interface in order to reduce the friction during the test. Compression tests were carried out at a constant true strain rate, up to a maximum strain of 0.6. For each alloy, 25 numbers of compression tests at different conditions were carried out. The constant true strain rate was maintained during the compression test by varying the cross head velocity using the relation [48]:

$$v = \dot{\varepsilon} L_o \exp(\dot{\varepsilon} t). \tag{3.2}$$

where v is the cross head velocity, $\dot{\varepsilon}$ is the strain rate, L_o is the initial specimen length, and t is the time elapsed. The actuator displacement at any instant of time was controlled by the closed loop servo-hydraulic control of the UTM. MAX^{TM} software was used for controlling the actuator movement. A computer code was used to carry out the test at constant true strain rates ($\dot{\varepsilon}$). The deformation temperatures (T) and strain rates ($\dot{\varepsilon}$) were in the ranges of 300–500 °C and 0.001 s^{-1} – 10 s^{-1}, respectively. Table 3.4 shows the temperatures and strain rates at which the tests were conducted up to a strain of 0.6.

Figure 3.14 Photograph of the high temperature compression testing setup

The load versus displacement data for each compression test was recorded and the true stress (σ) versus true strain (ε) plots (flow curve) obtained. From the flow curve the peak flow stress for each test conditions were determined. The various constitutive model parameters for the hot deformation behavior of the two alloys were also determined.

Table 3.4 Strain rates and temperatures of the compression tests

Constant strain rate (s^{-1})	Test temperature (°C)
0.001, 0.01, 0.1, 01 and 10	300, 350, 400, 450 and 500

3.5 Analysis of high temperature deformation behavior

The hot deformation behavior of all alloys was carried out by two methods: (i) constitutive modeling and (ii) artificial neural network (ANN) technique. The methodologies of these are highlighted below.

3.5.1 Constitutive modeling of hot deformation behavior.

From the flow curves, the peak flow stresses (σ_p) for each combination of $\dot{\varepsilon}$ and T were determined. The constitutive analysis (*cf.* section 2.6.1 and section 4.3.2) was carried out for all the alloys. The activation energy of deformation (Q), Zener-Hollomon parameter (Z) and other parameters of the constitutive model were determined and the effect of silver addition on these parameters was investigated. The relationship between the peak flow stress, temperature and strain rates for all the five alloys were obtained from the analysis and discussed.

3.5.2 Artificial neural network modeling of the flow stress

The flow stress of all alloys was predicted by artificial neural network (ANN) modeling. In order to obtain better prediction of flow stress (σ) during isothermal hot deformation of the investigated alloys, artificial neural network (ANN) modeling was carried out. This was based on the concept that

$$\sigma = \sigma(\varepsilon, \dot{\varepsilon}, T). \tag{2.15}$$

The deformation flow stress flow stress (σ) can be predicted by artificial neural network, which is a data driven model, if sufficient number of data sets is available. A typical artificial neural network (ANN) architecture consists of three layers, *viz.* an input layer consisting of three neurons representing the external parameters of strain (ε), strain rate ($\dot{\varepsilon}$) and temperature (T) a hidden layer containing n numbers of neurons and an output layer with one neuron representing flow stress. Appropriate values for the weight and bias of the network architecture for each alloy was arrived at by training the network using several data sets.

The artificial neural network modeling was carried out by the multiple layer perception (MLP) feed forward back propagation network. The input layer consisting of three neurons ($\dot{\varepsilon}$, ε, and T) and the flow stress (σ), in the output layer formed the data sets for training the network. The 'Neural Network' tool box available with the MATLAB (R2010a) software package was used for the present modeling. Training of the neural network was done using the artificial neural network tool kit of MATLAB software, using 'TRAINLM' function. 'TRAINLM' is a network training function that updates weights and bias values in a back propagation algorithm according to Levenberg–Marquardt optimization. Levenberg–Marquardt algorithm is a highly efficient method for solving non-linear optimization problems [40]. Single layer hidden neurons were used in the network architecture. The number of neurons in the hidden layer, the transfer functions at the input-to-hidden layer and hidden-to-output layer were optimized by trial and error method during the network training and testing stages. The mean square error (MSE) during the training and testing was determined for each trial. The network architecture was finally frozen based on the minimum mean square error value obtained during both the training and testing stages.

During the modeling, strain (ε), temperature (T) and $\ln(\dot{\varepsilon})$ values were transformed to lie within the range of 0.1 and 0.9. When the neural network is trained by minimizing the sum-squared error, the order of the error is independent of the magnitude of the target value. Therefore, it is likely that percentage error may be more in the case of target values of lower magnitude. In order that the percentage error in prediction is more or less uniform for low and high values of flow stress (σ), normalized values of $\ln(\sigma)$ were taken as the output layer of the network. The output was then operated by exponential function to get the values of flow stress (σ). Justification for this can be given as follows [40]: Let us consider that for a particular flow stress value of σ^*, the predicted value is given by $\ln(\sigma^* + e)$ where e is the error in prediction. The corresponding predicted flow stress (σ) value is then obtained by taking the exponential of the $\ln(\sigma^* + e)$ term. Therefore, the percentage error in prediction is expressed as [40]:

$$\frac{\exp(\ln\sigma^* + e) - \sigma^*}{\sigma^*} = \exp(e) - 1. \tag{3.3}$$

Since this percentage error is a function solely of e and is independent of σ^*, the error is expected to be fairly uniform irrespective of the target value.

Modeling of flow stress (σ) for various combinations of strain (ε), strain rate ($\dot{\varepsilon}$) and temperature (T) was carried out by artificial neural network. For each alloy, a total number of 150 input-output data sets (for combination of 5 true strain rates, 5 deformation temperatures and 6 true strain values considered) were obtained from the compression tests. It was decided to use 78 data sets for the network training, 48 data sets for the testing and 24 data sets from the remaining, for validation purpose. The validation data sets were not used earlier for the testing or training purposes. Both training and testing of the network was carried our independently. A number of numerical trials were carried out with single hidden layer neural network. The "*tansig*", "*logsig*" and "*purelin*" transfer functions were tried with while simultaneously varying the number of neurons in the hidden layer, in order to arrive at the best network architecture and processing function for each of the investigated alloys. The root mean square (RMS) functional error used as a measure of performance, can be expressed as

$$\mathrm{RMS}^{\mathrm{f}}_{\mathrm{err}} = \sqrt{\frac{\sum(\sigma - \sigma^*)^2}{n\sigma^2}}, \tag{3.4}$$

where σ is the experimental flow stress value and σ^* is the predicted flow stress value. Both training and testing errors were calculated separately. Effective error for training and testing data is given by:

$$\text{Effective error} = \text{max. of } [\,\mathrm{RMS}^{\mathrm{f}}_{\mathrm{err}} \text{ of training data, } \mathrm{RMS}^{\mathrm{f}}_{\mathrm{err}} \text{ of testing data}]. \tag{3.5}$$

The sum squared training error goal for flow stress (σ) was fixed at 0.00001. After a number of trials with various initial weights and biases, the best neural network architecture was frozen for which (i) functional root mean square (RMS) error was minimum, (ii) minimum number of data sets has a deviation error of 5 %, (iii) maximum deviation during testing and training is within 10 %, Predictability of the trained artificial neural network (ANN) model was verified *viz*. employing standard statistical parameters such as coefficient of determination (R^2). It is expressed as

$$R^2 = 1 - \frac{SS_{residual}}{SS_{total}},$$

$$SS_{residual} = \sum_{i=1}^{n} (E_i - P_i)^2,$$

$$SS_{total} = (n-1) \times s^2, \tag{3.5}$$

$$s^2 = \frac{\sum_{i=1}^{n} (E_i - \bar{E})^2}{n},$$

where s = standard deviation, E_i = Experimental value, P_i = predicted value, n = total number of data and $\bar{E}$ are the average values of E_i. The simulation results are presented and discussed in section 4.4.

3.5.3 Generation of Deformation Processing Maps

The flow stress values predicted by the artificial neural network (ANN) were used to generate the processing maps for all the alloys. The detailed procedure of generating the processing maps by dynamic material model (DMM) has been discussed in section 2.8. The relevant calculations were performed using MATLAB™ software toolkit. The strain rate sensitivity factor m was evaluated using Eq. (2.21). Since the experimental strain rates were differing by one order of magnitude and the test temperatures were at an interval of 50 °C, it was decided to generate a large number of data for the flow stress by artificial neural network simulation at small intervals covering the entire region of the strain rate and temperature experimentally investigated. For a particular strain rate, the flow stress for the neighboring regions of the strain rate values were determined by the following procedure.

Referring to Figure 3.15, let at point A, the value of strain rate is $\dot{\varepsilon}$, corresponding to which the value of σ can be obtained by artificial neural network. The values of the strain rates for the neighboring 8 points were decided as per Table 3.5.

The flow stress (σ) values corresponding to all the above nine different points of strain rate were determined for artificial neural network simulation. Let e be the flow stress value of point A where strain rate value is $\dot{\varepsilon}$. The flow stress value at point B and C is 1.5e and 0.5e respectively. Similarly, flow stress value at the point B_1, B_2, A_1, A_2, C_1 and C_2 were listed in table 3.5 at the particular combination of strain and temperature. The value of strain rate sensitivity (m), power dissipation efficiency and the instability parameters are calculated by Eq. (2.21), Eq. (2.29) and Eq. (2.31), respectively. From the contour plots of strain rate sensitivity (m), power dissipation efficiency (η) and the instability parameters (ξ) were obtained for different combination of strain (ε), strain rate ($\dot{\varepsilon}$) and temperature (T) covering the entire experimental domain.

Table 3.5 The values of strain rates and flow stress corresponding to different points shown in Figure 3.15

Point	Strain rate value	Flow stress value
A	$\dot{\varepsilon}$	e
B	1.5 × value at A	1.5 × value at A
C	0.5× value at A	0.5× value at A
A_1	1.2 ×value at A	1.2 ×value at A
A_2	0.8 × value at A	0.8 × value at A
B_1	1.2 × value at B	1.2 × value at B
B_2	0.8 × value at B	0.8 × value at B
C_1	1.2 × value at C	1.2 × value at C
C_2	0.8 × value at C	0.8 × value at C

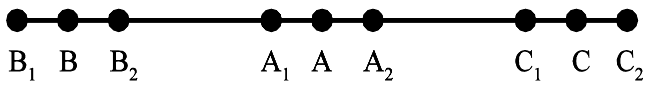

Figure 3.15 Points generated from a single strain rate ($\dot{\varepsilon}$) value for calculation of flow stress (σ) values and strain rate sensitivity (m) parameter

Microstructural observation of the samples was carried out after the compression tests in order to identify the changes induced in the microstructure for a true stain value of 0.6. The results obtained using these experimental and computational procedure are presented and discussed in detail in Chapter 4.

Chapter 4

Results and Discussion

The results obtained from the experiments outlined in Chapter 3 along with discussions are presented in this chapter. This includes results of chemical analysis, microstructure characterization and mechanical properties of the cast as well as cast-rolled alloys under different heat treatment conditions. Age hardening behavior, hot deformation characteristics, artificial neural network (ANN) modeling for the prediction of flow stress and hot deformation processing maps of the alloys are also presented and discussed.

4.1 Microstructure and mechanical properties

2219 aluminum alloy and 2219 aluminum alloy microalloyed with silver (Ag) were prepared from aluminum ingots of commercial purity by casting route. Overall composition analysis of the cast alloys determined by Atomic absorption spectrophotometer (AAS) is listed in Table 4.1. The composition of the base alloy (Alloy-A) is close to 2219 aluminum alloy. Alloy-B to Alloy-E correspond to that of the base alloy microalloyed with 0.03 to 0.1 wt.% silver.

4.1.1 Microstructural studies

Microstructure and grain size of the as-cast and processed alloys have been investigated using optical microscope (OM) and scanning electron microscope (SEM). The compositions of the different phases present in the alloys were determined by energy dispersive X-ray spectra (EDS) analysis. The results and discussions are presented in the following sub-sections.

4.1.1.1 Microstructure of as-cast alloys

Microstructures of all alloys in the as-cast condition have been investigated using optical microscope. Low magnification optical micrographs of the alloys have been shown in Figure 4.1. The micrographs revealed dendrite structure with inter-dendritic segregation at grain boundary regions. Observation under high magnification reveals two types of constituent phases at the grain boundary regions (Figure 4.2): (i) a dark phase (*Phase-A*) having script type morphology and (ii) a white plate type phase

(*Phase-B*) uniformly distributed along the grain boundaries. Analysis reveals that the volume of *Phase-B* remains almost constant in all the alloys whereas the volume of *Phase-A* increased with increase in silver content. Observation of the microstructure under scanning electron microscope (SEM) revealed fine micro-porosities ($\approx 50\mu m$) at grain boundary regions. This is shown in Figure 4.3. Due to the large freezing range of the present alloys, micro-porosities due to shrinkage are expected to form during the casting process.

Typical scanning electron microscope (SEM) images of the as-cast alloys have been shown in Figure 4.4. Microstructure of Alloy-B is shown in Figure 4.5 along with the energy dispersive X-ray spectra (EDS) obtained for *Phase-A* and *Phase-B.* Quantitative analysis of the energy dispersive X-ray spectra (EDS) of all alloys revealed *phase-B* as $CuAl_2$, i.e., "θ" phase, whereas *phase-A* consists of a mixture of aluminum (Al), iron (Fe), copper (Cu), silicon (Si) and manganese (Mn). As per the Al-Cu binary phase diagram [1], $CuAl_2$ phase is expected to form during the solidification of aluminum alloys containing copper in excess of 5.5 wt.%. Results of the composition analysis by energy dispersive X-ray spectra (EDS) for different phases present in the as-cast alloys have been presented in Table 2. The concentration of iron (Fe) and manganese (Mn) in *phase-A* increased with increase in silver content up to 0.07 wt.% in the alloy. With further addition of silver (Ag), concentration of iron and manganese in *Phase-A* decreased.

Table 4.1 Chemical composition (wt.%) of alloys in cast condition

Alloy designation	Composition in wt.%							
	Cu	Mg	Zn	Fe	Mn	Ti	Ag	Al
Alloy-*A*	6.85	0.01	0.68	0.60	0.2	0.06	0.00	Balance
Alloy-*B*	6.78	0.01	0.76	0.62	0.19	0.08	0.03	Balance
Alloy-*C*	6.47	0.01	0.69	0.61	0.19	0.03	0.06	Balance
Alloy-*D*	6.37	0.01	0.66	0.57	0.18	0.06	0.07	Balance
Alloy-*E*	6.84	0.01	0.73	0.61	0.18	0.02	0.1	Balance

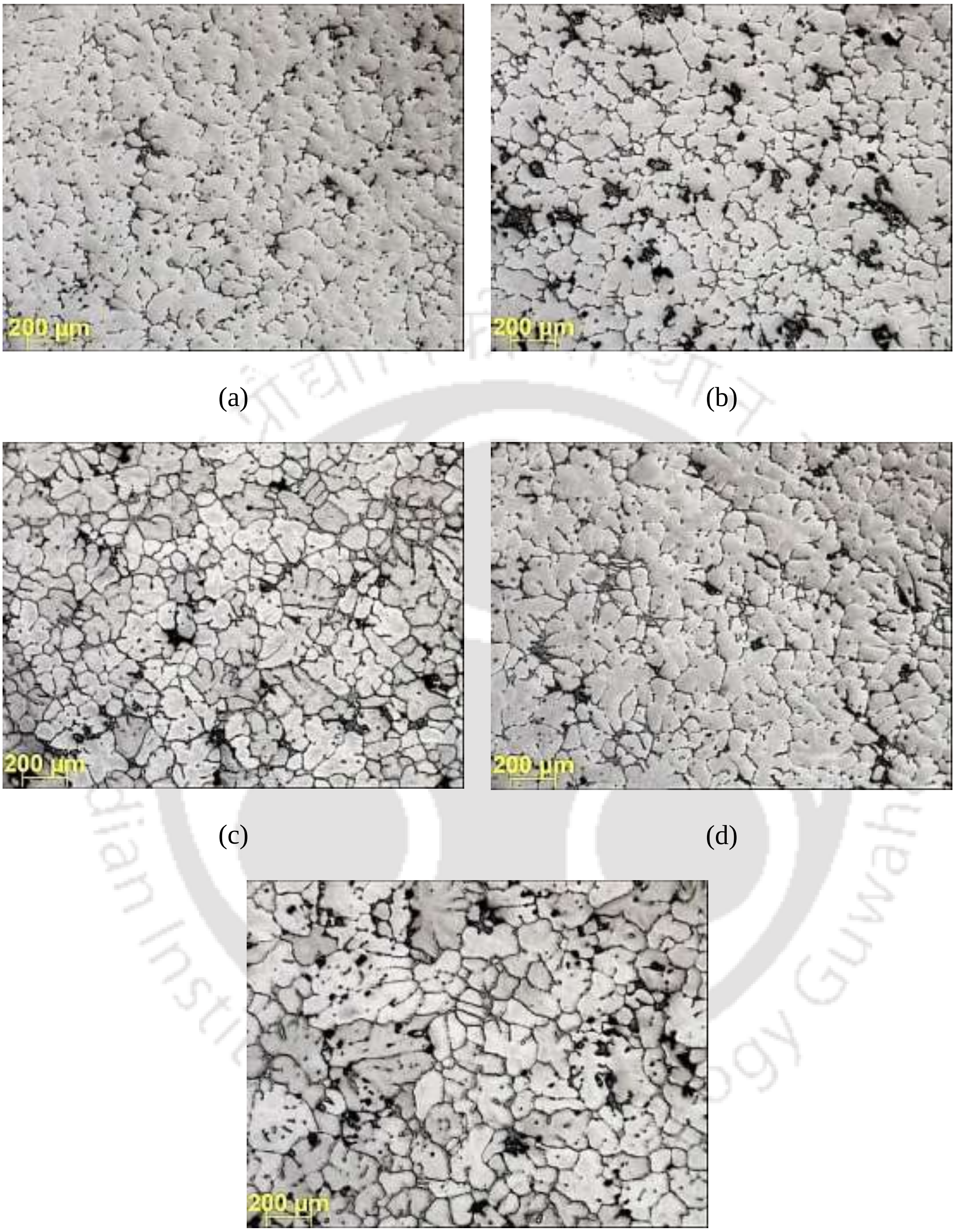

(a) (b) (c) (d) (e)

Figure 4.1 Low magnification (X5) optical micrograph of as-cast of alloys (a) Alloy-A, (b) Alloy-B, (c) Alloy-C, (d) Alloy-D and (e) Alloy-E

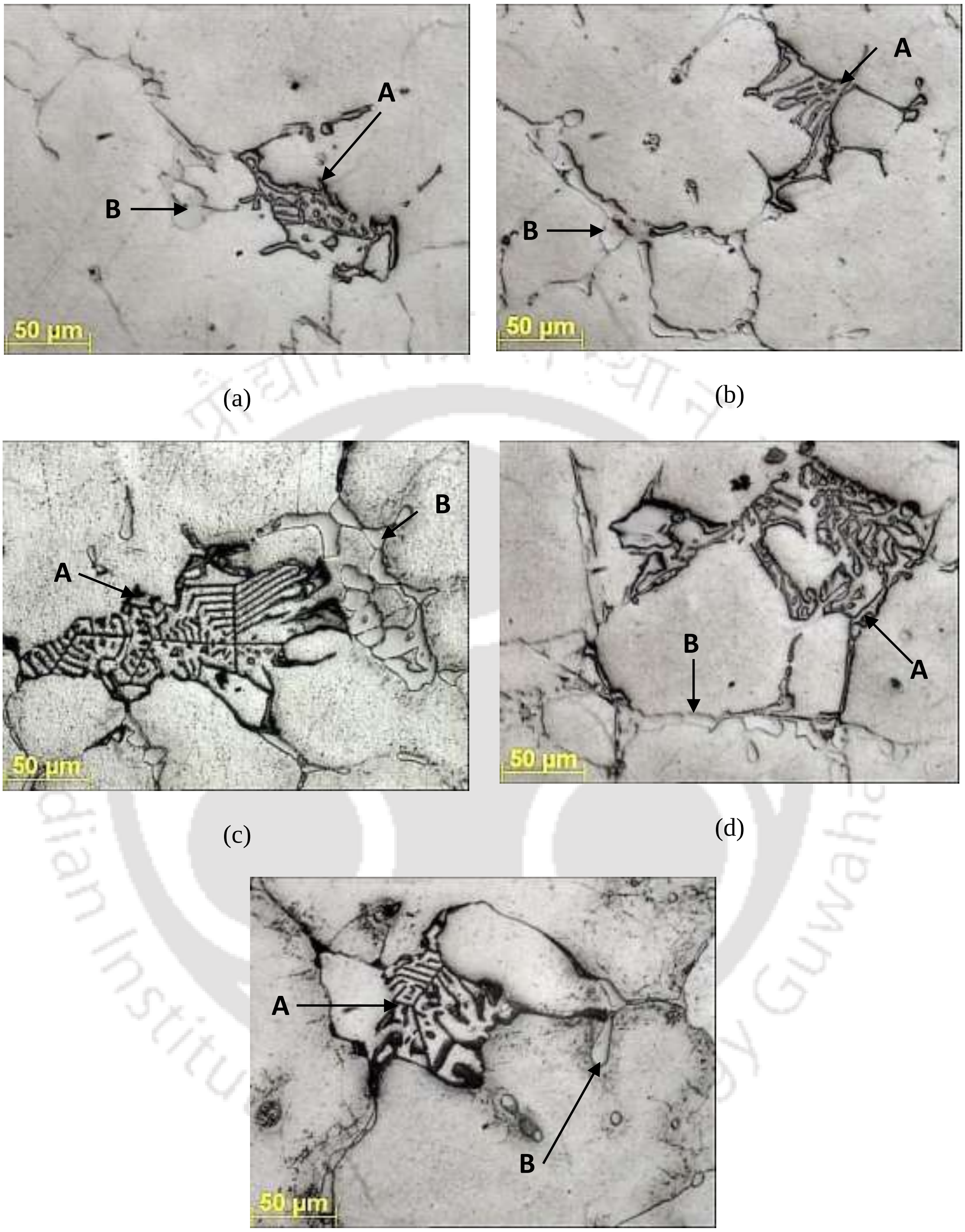

(a) (b) (c) (d) (e)

Figure 4.2 High magnification (X50) optical micrographs of as-cast alloy (a) Alloy-A, (b) Alloy-B, (c) Alloy-C, (d) Alloy-D and (e) Alloy-E

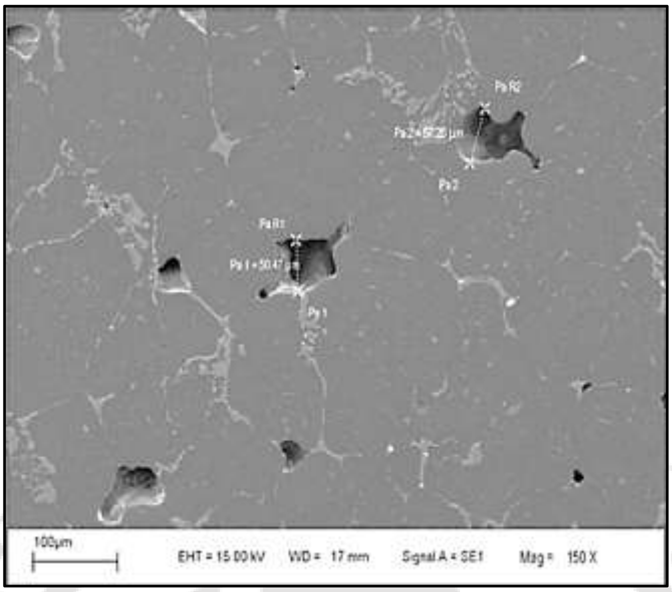

Figure 4.3 Scanning electron microscope (SEM) micrograph of Alloy-A reveling shrinkage porosity

Table 4.2 The composition of different phases observed in the as-cast alloy

Alloy designation	*Phase-A*	*Phase-B*
Alloy-A	$Al_{82}Fe_7Cu_6Si_4Mn_{1.0}$	$CuAl_2$
Alloy-B	$Al_{73}Fe_{13}Cu_4Si_8Mn_2$	$CuAl_2$
Alloy-C	$Al_{68}Fe_{14.5}Cu_6Si_{8.5}Mn_2$	$CuAl_2$
Alloy-D	$Al_{65}Fe_{19.3}Cu_7Si_{5.5}Mn_{3.2}$	$CuAl_2$
Alloy-E	$Al_{67.2}Fe_{11}Cu_3Si_{6.5}Mn_{2.3}$	$CuAl_2$

The microstructure observed can be explained by referring to the Al-Cu binary equilibrium phase diagram shown in Figure 2.3. During cooling, as the temperature of the molten metal crosses the liquidus temperature (~643 °C), the primary solid phase (α-phase) starts nucleating from the melt with simultaneous rejection of solute (Cu) atoms into the liquid. As the temperature is further lowered, more α-phase is formed and the liquid gets enriched with copper. At the solidus temperature, composition of the remaining liquid will attain the eutectic composition. This liquid will solidify by a eutectic transformation resulting in a eutectic mixture of α and θ-phases. Hence, the microstructure of the present alloys is expected to consist of pro-eutectic Al-phase (α-

phase) as the primary phase along with a eutectic mixture of α and θ phases at the grain boundary regions. Iron-rich (Fe) phases have been reported in the microstructure of 2219 aluminum alloys [115]. The iron-rich phase (*Phase-B*) present in the as-cast alloys (with script morphology) can thus be attributed to non-equilibrium solidification.

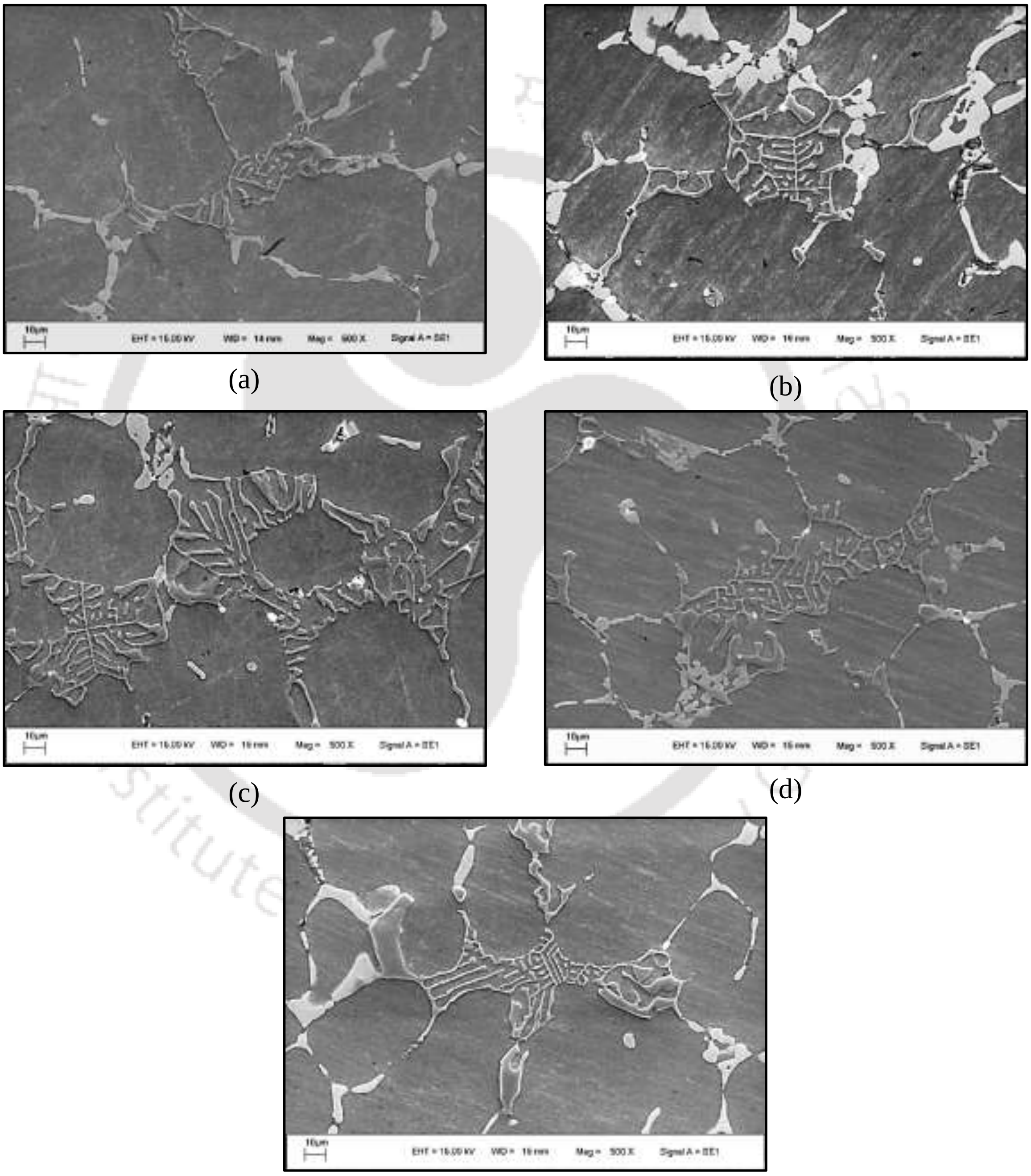
(a)
(b)
(c)
(d)
(e)

Figure 4.4 Scanning electron microscope (SEM) micrographs of as-cast (a) Alloy-A, (b) Alloy-B, (c) Alloy-C, (d) Alloy-D and (e) Alloy-E

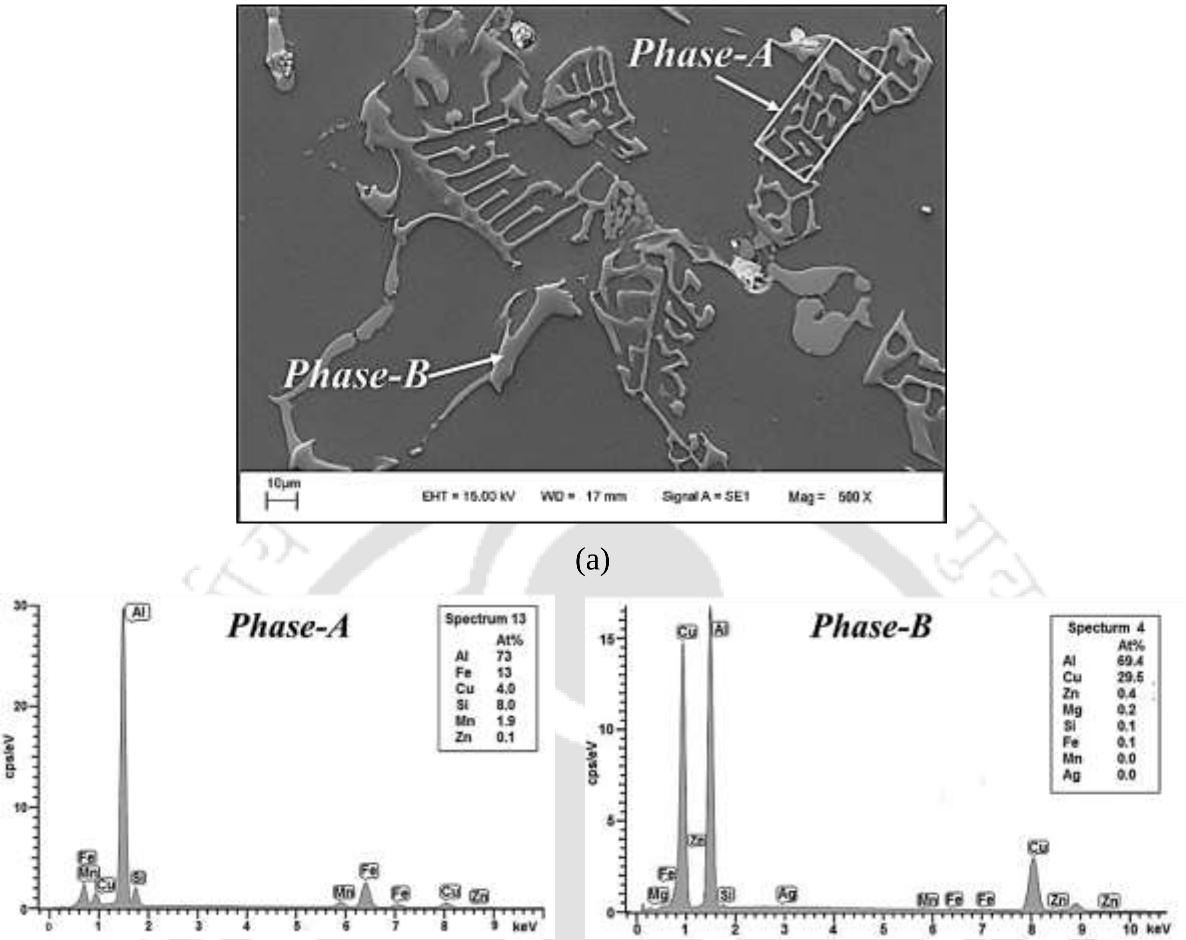

(a)

(b)

(c)

Figure 4.5 (a) Scanning electron microscope (SEM) micrograph of Alloy-B and (b) and (c) energy dispersive spectrum (EDS) of the "*phase A*" and "*phase B*" Respectively

4.1.1.2 Microstructure of cast and solutionized alloys

The optical micrographs of all the cast and solutionized alloys under un-etched and etched condition have been shown in Figure 4.6 and Figure 4.7, respectively. The micrographs reveals presence of $CuAl_2$ (*Phase-B*) along the grain boundary regions. Since the melting point of the intermetallic $CuAl_2$ is about 591 °C [116], dissolution of $CuAl_2$ in the matrix is not possible during the solution temperature at 525 °C. However, "*Phase A*" observed in the as-cast condition (Figure 4.1) is not evident in the micrographs. This indicates dissolution of "*Phase A*" in the matrix during the solutionizing heat treatment. The optical micrographs of the solutionized alloys in the etched condition reveal equiaxed grains. During solution heat treatment, the constituent elements from “*Phase A*” diffuse into the grains resulting in change in the morphology of grains and dissolution of metastable “*Phase A*”.

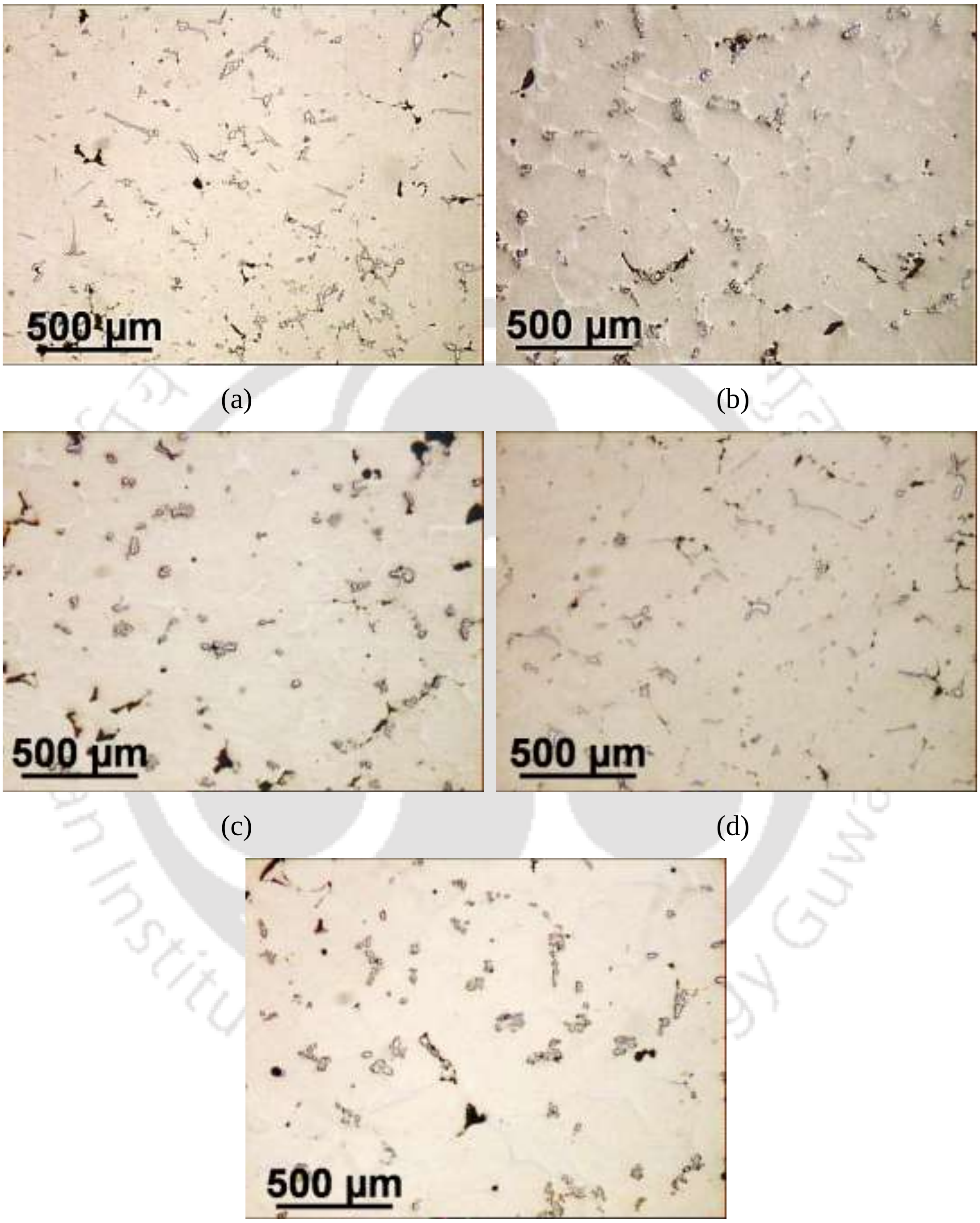

(a) (b)

(c) (d)

(e)

Figure 4.6 Optical micrograph (X5) of (a) Alloy-A, (b) Alloy-B, (c) Alloy-C, (d) Alloy-D and (e) Alloy-E in the cast and solutionized (un-etched) conditions

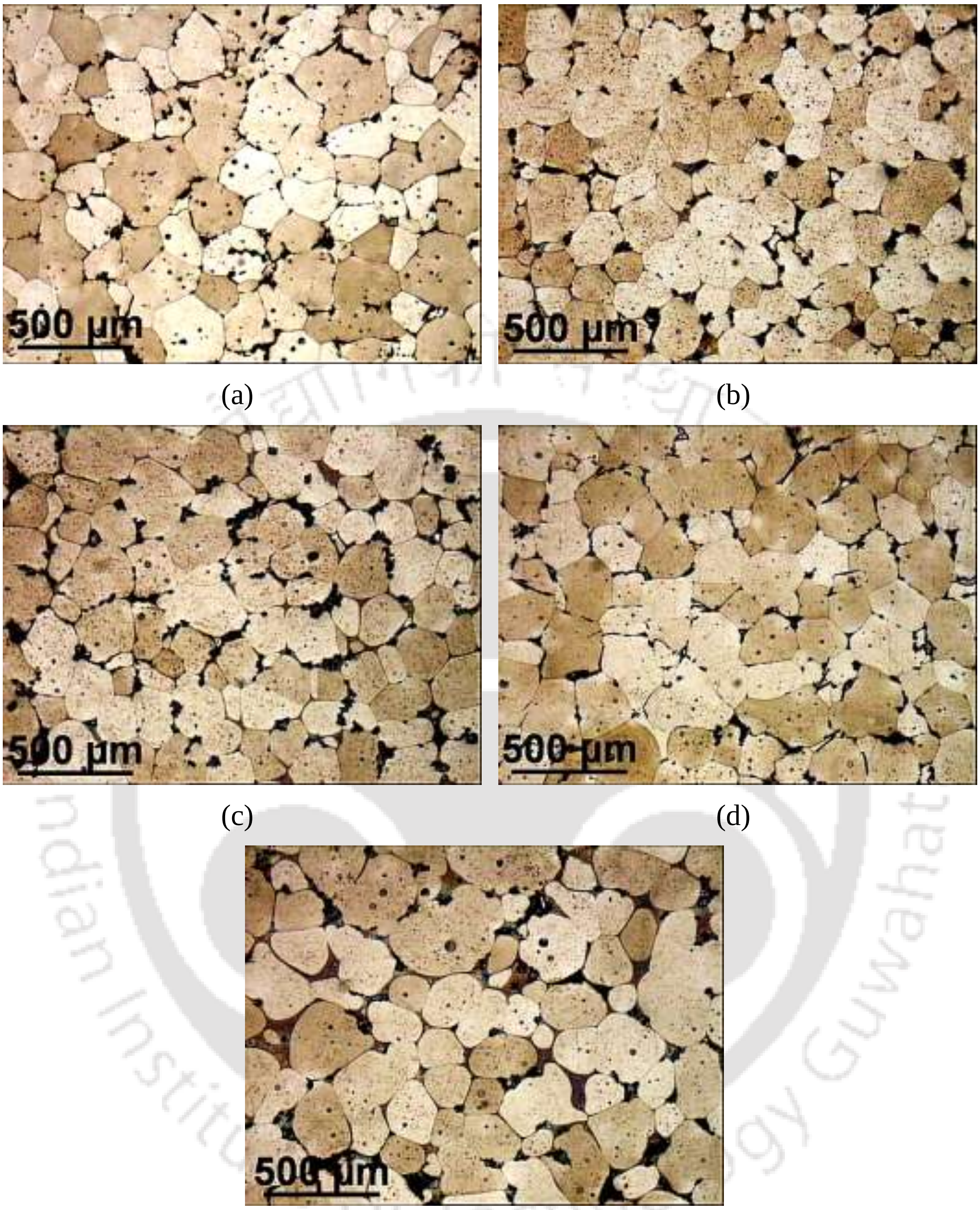

(a) (b) (c) (d) (e)

Figure 4.7 Optical micrograph (X5) of (a) Alloy-A, (b) Alloy-B, (c) Alloy-C, (d) Alloy-D and (e) Alloy-E in the cast and solutionized (etched) conditions

4.1.1.3 Microstructure of rolled and solutionized alloys

The materials under investigation are wrought aluminum alloys. For achieving the best combination of mechanical properties, these alloys were subjected to secondary deformation processing by rolling, forming, drawing etc. followed by heat treatment. Figure 4.8 shows the optical micrographs of Alloy-A and Alloy-E after rolling. The figure shows uniform distribution of fine intermetallic particles in the matrix. The fine size of intermetallic particles indicates considerable particle fracture during the rolling process. Grain boundaries are not observed in as-rolled samples indicating breakage of dendritic structure during plastic deformation. Hence, the grain size determination for the as-rolled samples could not be carried out. Micro-porosities present in the as-cast condition (Figure 4.3) are not evident after rolling. Optical micrographs of the rolled and solution heat treated samples are shown in Figure 4.9. The microstructure of transverse section of the rolled alloys reveals almost equiaxed grains with uniform grain sizes. Second phase particles of $CuAl_2$ phases can be seen at grain boundary regions. From the Al-Cu binary phase diagram (Figure 2.3), 5.6 wt.% copper can dissolve in the aluminum lattice at 548 °C. Solubility of copper in aluminum decreases with decrease in temperature. Copper percentage in the present alloys varies between 6.5–6.8 wt.%. At the solutionizing temperature of 525 °C, the alloy matrix is supersaturated by around 1.5 wt.% copper. Hence excess copper exists as $CuAl_2$ particles at grain boundary regions.

4.1.2 Grain size analysis

The average grain size determined for all alloys under various process conditions has been depicted in Figure 4.10. The grain size of as-rolled alloys could not be resolved even by scanning electron microscope (SEM). Average grain size of the as-cast alloys increases marginally from 89 μm to 94 μm with increase in silver content. This indicates that microalloying of the base alloy with silver has no significant effect on the grain size during solidification. It has been reported that the addition of trace amounts of tin or titanium did not influence the grain size of cast Al-Cu alloys significantly [17, 18].

Quantitative analysis reveals considerable grain coarsening (by ≈ 2.3 times) during solution heat treatment compared to the as-cast microstructure. The grain size of the rolled samples after solution heat-treatment is found to be fine and ranges between 51 μm to 62 μm. Grain size of rolled and heat treated alloys increased with increase in silver content. Grain size of rolled and solution heat treated specimen increases by around 22% as the silver content in the alloy increases from 0.0 wt.% to 0.1 wt.%. However, age hardening heat treatment at 150 °C did not affect the grain size of the alloy.

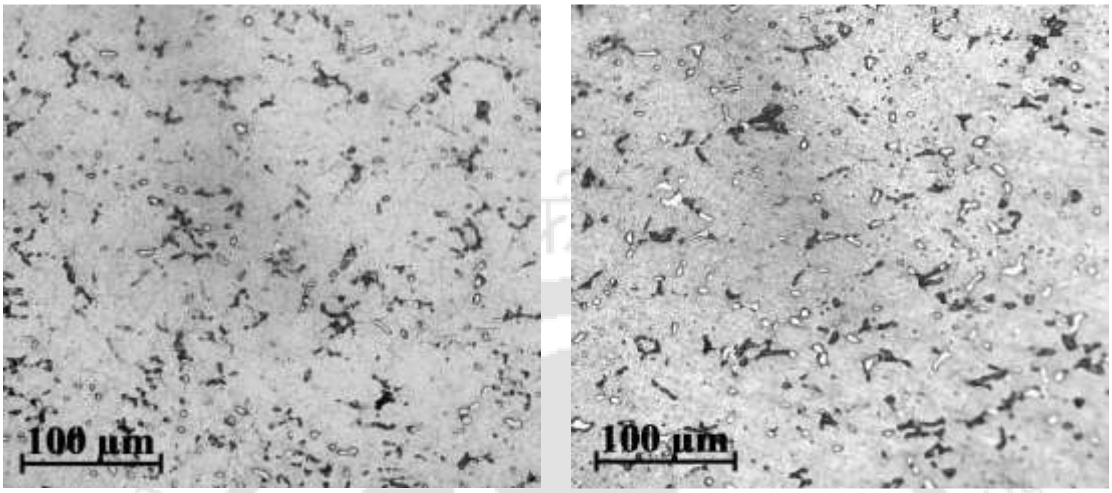

(a) (b)

Figure 4.8 Optical micrograph (X20) of rolled (a) Alloy-A and (b) Alloy-E

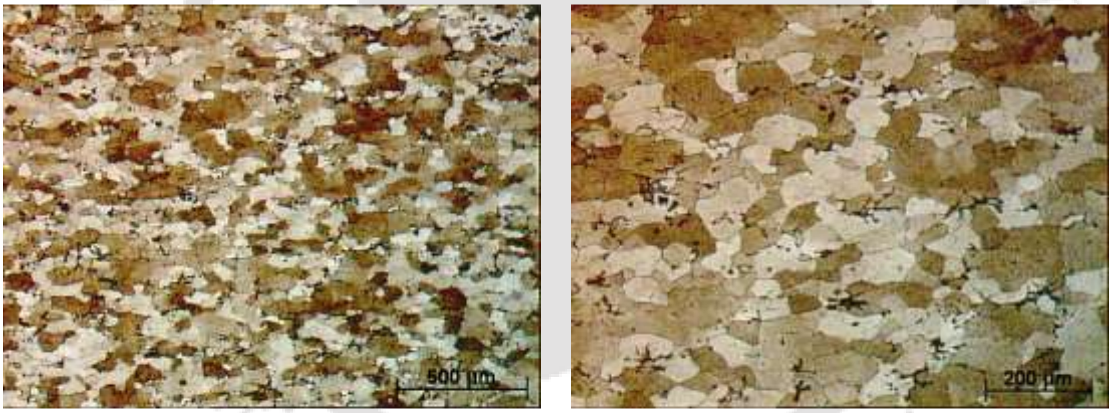

(a) (b)

Figure 4.9 Optical micrograph of rolled and solutionized alloy-A at (a) low magnification (X5) and (b) high magnification (X10)

4.1.3 Age hardening behavior

Plots of hardness versus ageing time for all alloys during isothermal ageing at 150 °C has been depicted in Figure 4.11. The hardness of all alloys increases with increase in time during the pre-aging stage. After attaining a maximum value (peak ageing), the hardness decreases with time (over ageing stage). Hardness increases with increase in silver content up to 0.07 wt.% (Alloy-D) in the alloy and decreases with further increase in silver content. This trend is similar to the variation of the hardness with the silver content in the Al-alloys after the solution heat treatment. The peak hardness for all alloys was achieved when aged for ~35 hours. Ageing, for time periods in the range 35-45 hours, reveals only marginal variations in hardness. Subsequent ageing results in decrease in hardness with aging time. The maximum hardness is observed for Alloy-D (containing 0.07 wt.% silver) when aged for 45 hours showing 99% increase in hardness value compared to the solutionized alloy. In the base alloy (Alloy-A), this increase was only 86%.

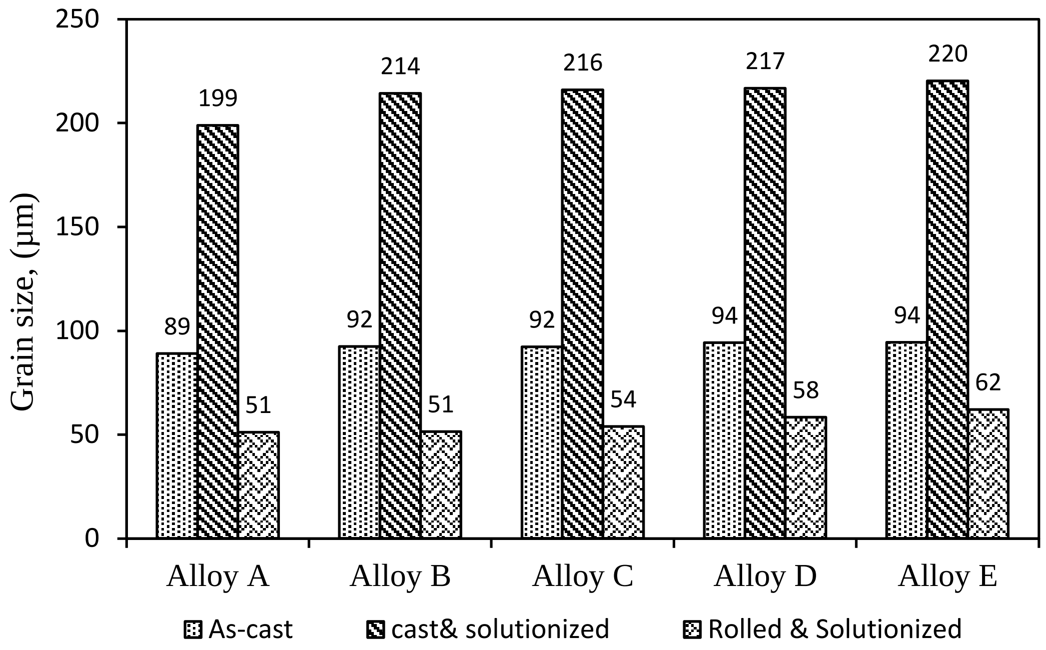

Figure. 4.10 Grain size variation of the alloys under different process conditions (Note: Error bar is not shown due to very low deviation)

Murayama at al. [117] reported that silver addition has no role in the nucleation kinetics of Al-Cu-Li-Mg-Ag alloy, although Mg is essential for enhancing the precipitation hardening behavior. The precipitation sequence in Al-Cu alloys having high Cu:Mg ratios generally occur by the formation of *S* or *S'* (Al_2CuMg) cluster. However, addition of silver results in the formation of Mg-Ag co-cluster which diffuse into the *S* phase during precipitation hardening treatment leading to increase in hardness [117–118]. Results of the present study reveals 99% increase in hardness during aging by addition of 0.07 wt.% silver. Since the present alloys contain 0.01 wt.% magnesium and silver ≤ 0.1 wt.%, it can be inferred that silver addition up to

0.07 wt.% enhances the alloy hardness. Also the kinetics of precipitation hardening of the alloys is not affected by addition of silver.

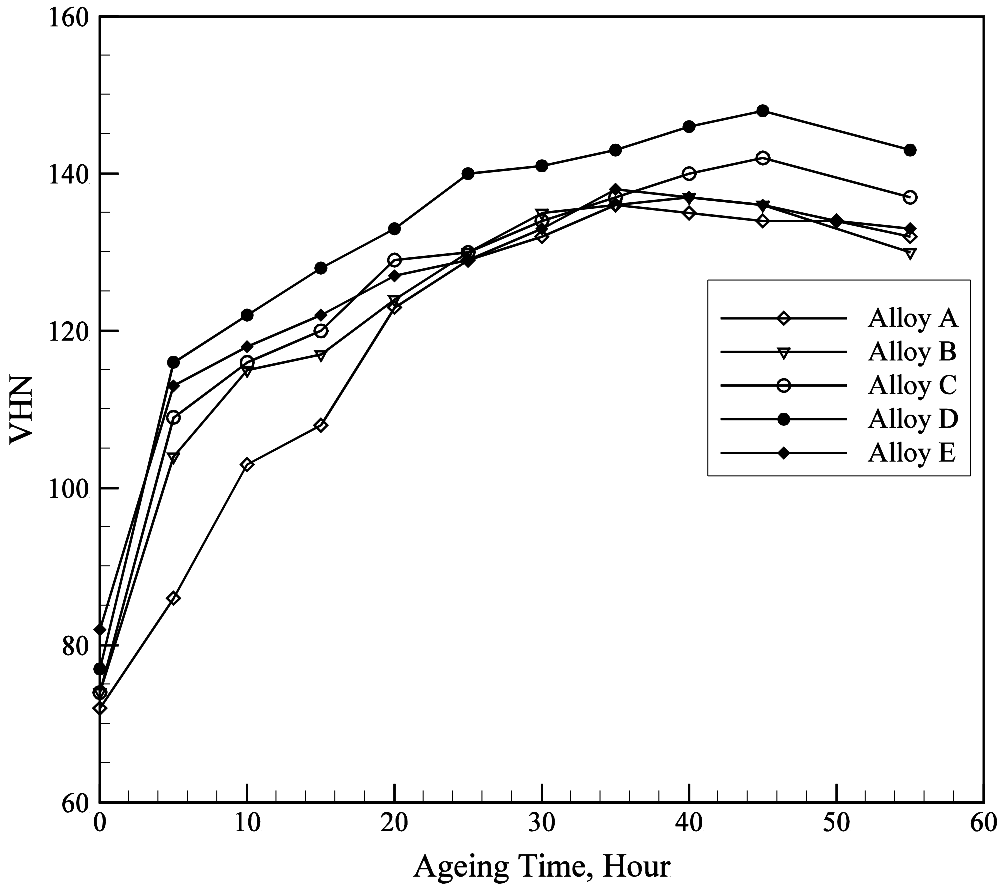

Figure 4.11 Plots of hardness versus aging time of all alloys

X-ray elemental mapping of Alloy-E for elements aluminum (Al), copper (Cu), magnesium (Mn), manganese (Mg), iron (Fe) and silver (Ag) at peak aged condition has been shown Figure 4.12. Presence of copper (Cu) in the $CuAl_2$ phase is evident in the figure. In addition, small quantities of copper are also seen uniformly distributed in the aluminum matrix which is expected from the present alloy. Silver is found to be distributed uniformly in the aluminum matrix. Since the atomic diameters of silver and aluminum are almost same (diameters of 286 pm for aluminum and 288 pm for silver), silver cannot occupy the interstitial lattice site of aluminum and therefore exists as a substitutional impurity in aluminum matrix. X-ray mapping indicates that manganese is uniformly distributed in the aluminum matrix after precipitation treatment. Though manganese was found to be present in “*Phase A*” of cast alloy, subsequent heat treatments did not reveal “*Phase A*” indicating that manganese has dissolved in the aluminum matrix. The figure also reveals that iron is distributed mainly at grain boundary regions. The study reveals that the solutionized heat treatment resulted in strong interaction between silver and vacant lattice sites of aluminum leading to their retention in the supersaturated solid solution of Al-Cu alloy containing 0.1 wt.% silver [118–119].

The initial stage of age hardening in the present alloys is very rapid. Figure 4.11 reveals that around 76% of the peak hardness values were achieved during the first 5 hours of ageing for all alloys containing silver (Ag). Subsequent ageing resulted in increase in hardness, but at a slow rate till the peak hardness was achieved. Earlier studies revealed that during the age hardening process, co-clustering of silver and magnesium occurs in the Al-Cu alloys containing silver and the co-cluster do not include copper atoms [118–119]. Silver exists as a substitutional impurity in aluminum lattice. Since the main diffusion mechanism in substitutional solid solution alloys is either by direct interchange mechanism or Zener ring mechanism, diffusion of silver through the aluminum lattice is rugged. Hence addition of silver below 0.1 wt.% does not have much influence on the kinetics of precipitation hardening in the base alloy.

Differential scanning calorimetric (DSC) investigation

Differential scanning calorimetric (DSC) studies were carried out to investigate the kinetics of the precipitation reaction. Experiments were carried out from 40 °C to 560 °C at heating rates of 5 °C/min, 10 °C/min, 15°C/min, and 20 °C/min. Figure 4.13 (a) to (c) shows the differential scanning calorimetric (DSC) curves obtained for Alloy-A for the four heating rates along with derivatives. The figures indicate exothermic peaks in the range 194 °C – 219 °C and 239 °C to 255 °C.

In addition, endothermic peaks at temperatures above 520 °C were observed that can be attributed to the dissolution of the low melting point phase at the grain boundaries. The two exothermic peaks between 200 °C to 300 °C corresponded to the precipitation process. Banerjee [120] attributed the presence of two exothermic peaks in Al-Cu alloy to precipitation at the grain boundaries and precipitation inside the grains. The two well-resolved exothermic peaks in the present differential scanning calorimetric (DSC) curves of Alloy-A indicate a two-step precipitation mechanism. The first peak corresponds to precipitation at the grain boundaries whereas the second peak corresponds to precipitation inside the grains.

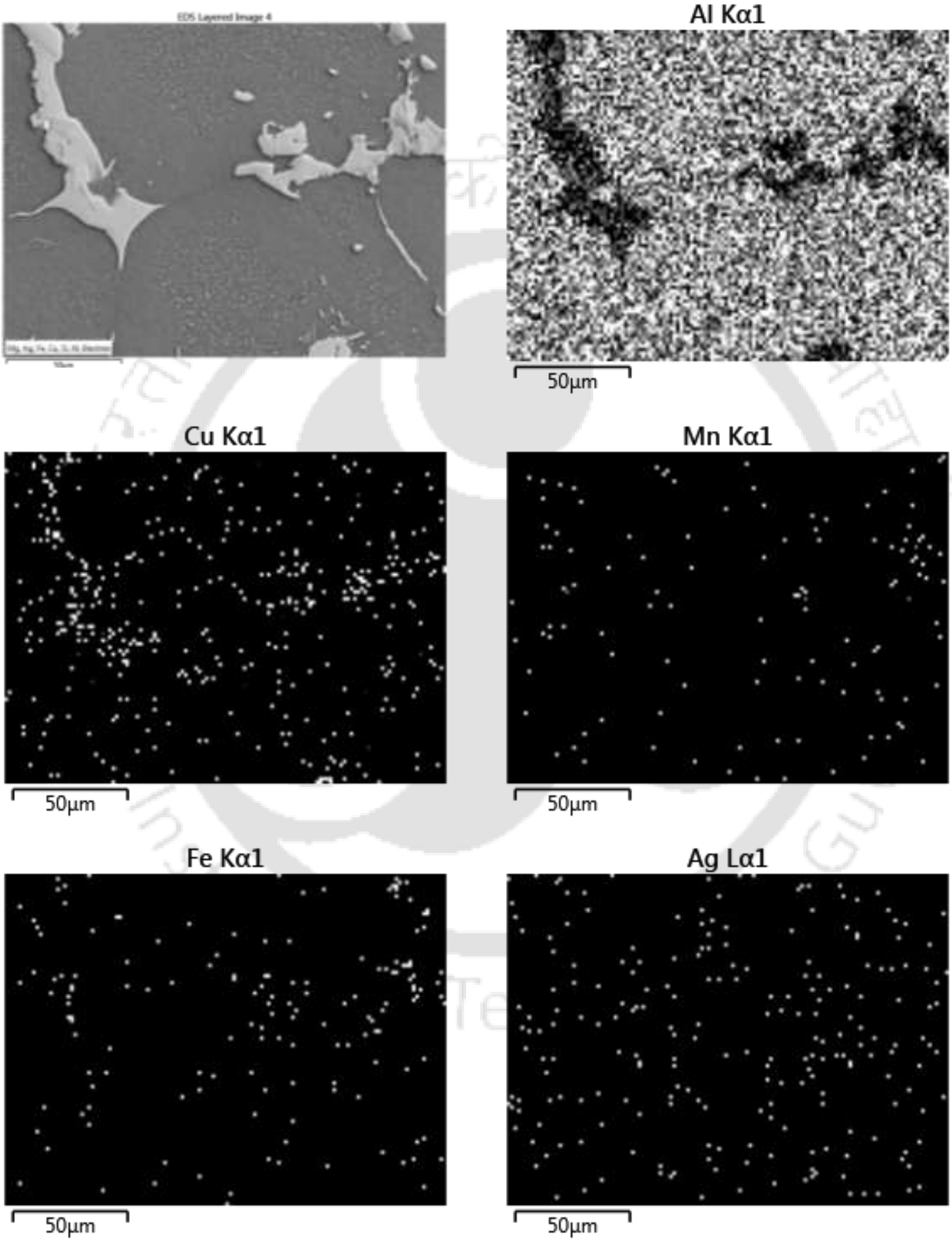

Figure 4.12 Scanning electron microscope (SEM) image and elemental mapping for aluminum (Al), copper (Cu), manganese (Mn), iron (Fe), and silver (Ag) of Alloy-D in the peak aged condition

The observed peaks shift toward the right at higher heating rates indicates that the reaction is rate controlled. The differential scanning calorimetric (DSC) curves obtained for other alloys heated at a heating rate of 10 °C/min have been shown in Figure 4.14. The two exothermic peaks are not observed in these alloys though differential scanning calorimetric (DSC) studies were carried out at all the four heating rates. To check the authenticity of the results, experiments were also carried out using two different equipment. Hence the influence of silver addition on the kinetics of the precipitation reaction could not be established.

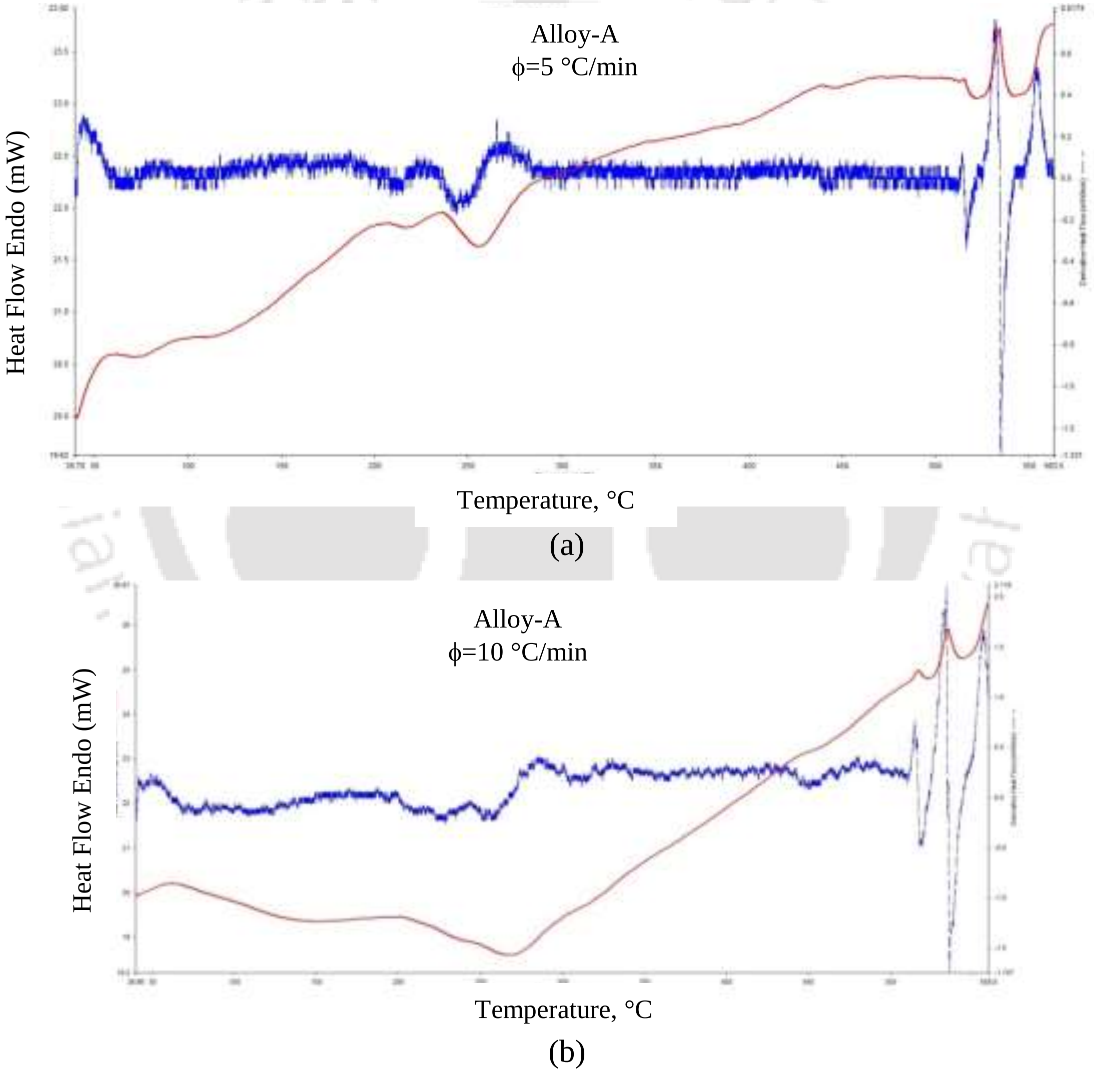

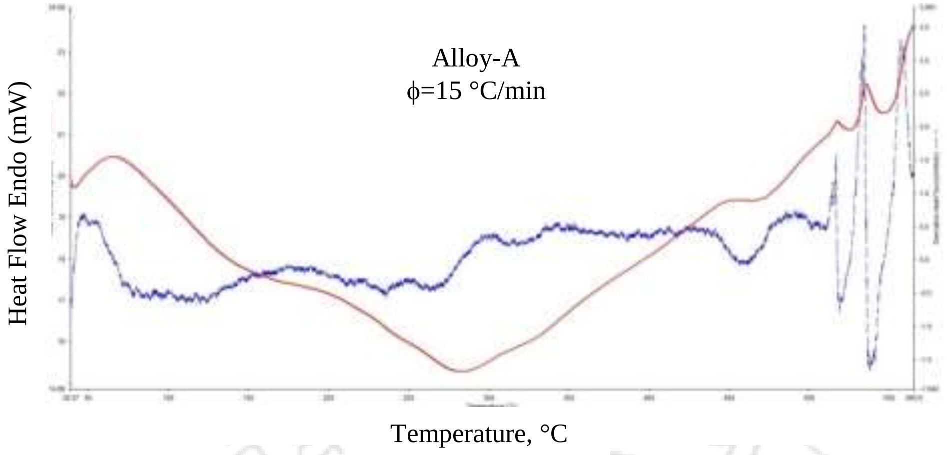

(c)

Figure 4.13 Differential scanning calorimetric (DSC) curves obtained for Alloy-A (a) ϕ=5 °C/min, (b) ϕ=10 °C/min and (c) ϕ=15 °C/min

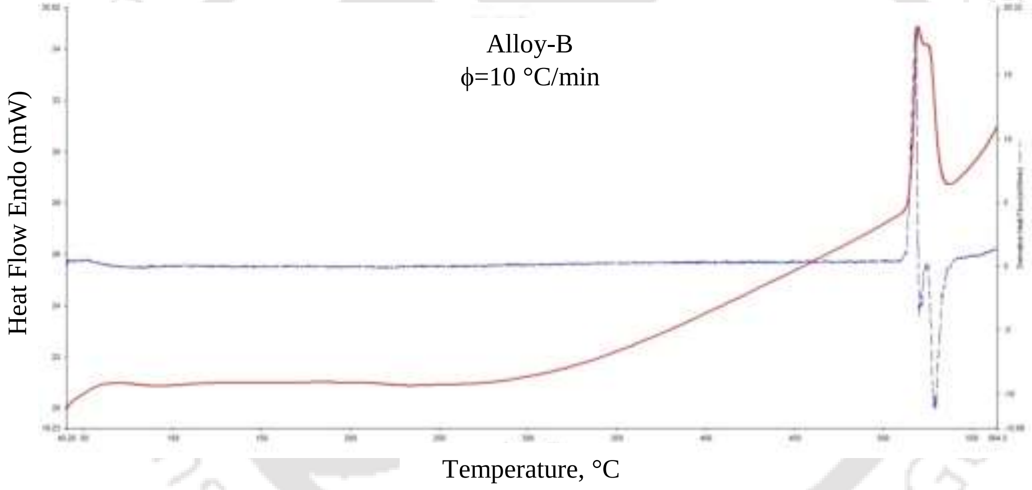

(a)

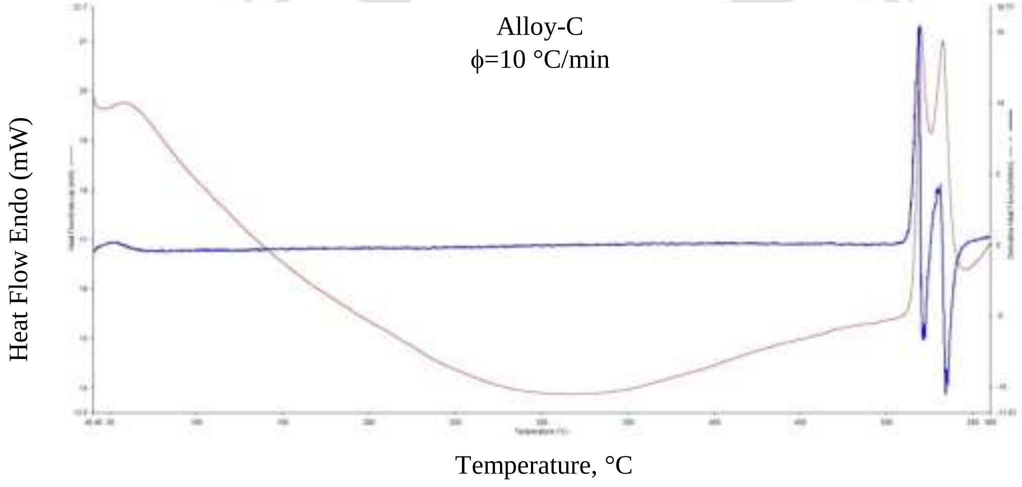

(b)

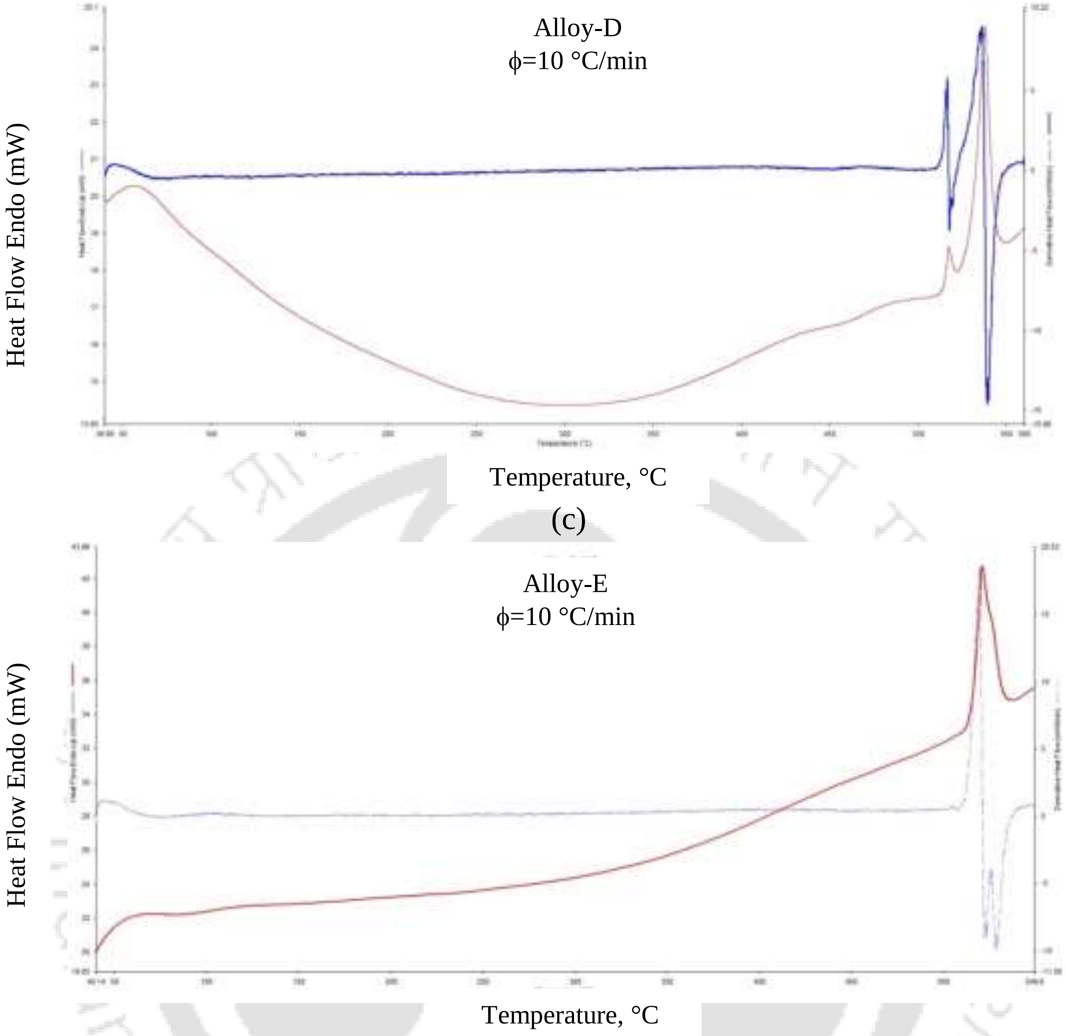

(c)

(d)

Figure 4.14 Heat flow curves obtain by differential scanning calorimeter (DSC) for (a) Alloy-B, (b) Alloy-C, (c) Alloy-D and (d) Alloy-E

4.1.4 Transmission electron microscope (TEM) analysis

Bright field transmission electron microscope (FETEM) micrographs and corresponding energy dispersive X-ray spectra (EDS) results of Alloy-A at solution heat treated condition and peak aged conditions have been depicted in Figure 4.15 (a) and (b) respectively. Fine precipitates homogeneously distributed in the solution heat treated alloy matrix (α phase) can be observed in Figure 4.15(a). Microstructure of the peak aged sample shown in Figure 4.15(b) reveals an increase in the precipitate size. Energy dispersive X-ray spectra (EDS) analysis of the precipitate in the peak aged condition reveals these particles as $CuAl_2$ phase.

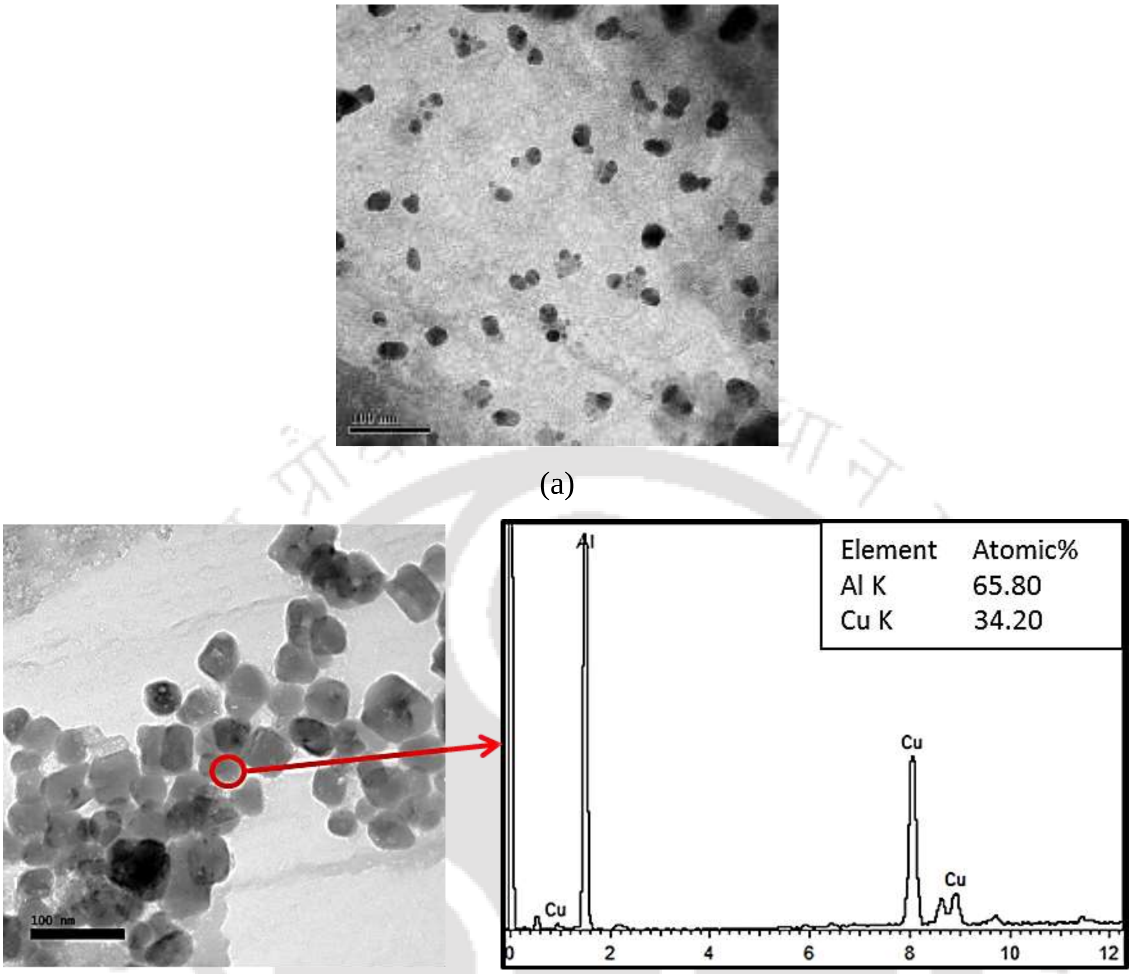

(a)

(b)

Figure 4.15 Bright field transmission electron microscope (TEM) image, micrograph and energy dispersive X-ray spectra (EDS) of matrix of Alloy-A after (a) solution heat treatment and (b) at peak ageing

Bright field TEM micrographs of Alloy-D after solution heat treatment and peak ageing have been shown in Figure 4.16 (a) and (b) respectively. The energy dispersive X-ray spectra (EDS) analysis results of the matrix region and precipitates are also depicted in the respective figures. Precipitates present in solution heat treated Alloy-D is identified as Al-Cu-Ag phase with the 0.13 at.% silver Figure 4.16(a). Energy dispersive X-ray spectra (EDS) analysis of the precipitates after peak aging reveals the precipitate as $CuAl_2$ containing 0.73 at.% silver. However, the silver content in the matrix remains almost the same during age hardening. The result indicates enrichment of precipitate by silver due to diffusion from the matrix. Comparison of the TEM micrographs of Figure 4.15 (b) and Figure 4.16 (b) reveal a morphological change in the precipitate from plate shape to disc shape in the peak aged condition due to the addition of silver.

The transmission electron microscope (TEM) investigation of as-quenched Al-1.7Cu-0.5 Mg and Al-1.7Cu-0.5Mg-0.1Ag alloys by Hono at al. [119] revealed presence of high density of dislocation loops which were formed due to condensation of vacancies in the ternary alloy. However, these were absent in the alloy containing silver. The authors concluded that the presence of high binding energy between silver atoms and vacancies facilitate rapid diffusion resulting in the formation of GP-zones in the silver containing aluminum alloy in the as-quenched condition. In the present study dislocation loops were not observed in any of the alloys. This is attributed to the high Cu:Mg ratio in the investigated alloys which falls in the $\alpha+\theta$ region of the Al-Cu-Mg ternary phase diagram.

4.2 Mechanical properties

Mechanical properties of cast, rolled and different heat treated alloys were determined. Details of Vickers hardness, uniaxial tensile properties and age hardening behavior of alloys are discussed in this section.

4.2.1 Hardness

The plots of hardness of the cast alloys under different processing conditions are shown in Figure 4.17. The hardness in the as-cast condition remains almost constant till the silver content is increased beyond 0.06 wt.% (Alloy-C). An increase in hardness is observed in the alloy with further increase in silver content up to 0.1 wt.%. As the silver content is increased from 0.06 wt.% to 0.1 wt.%, the hardness increases by ~ 35%. Solution heat treatment resulted in further increase in the hardness of the as-cast alloys. The hardness of the solution treated samples increases gradually with increase in silver content. The hardness variation with silver (Ag) content after solution heat treatment followed the similar trend as that of as-cast alloys. The maximum hardness value of 82 VHN was observed for Alloy-E after solution heat treatment indicating an increase in hardness of around ~ 11% compared to that of the as-cast alloy. The hardness of the cast alloys after precipitation heat treatment was discussed in Section 4.1.3.

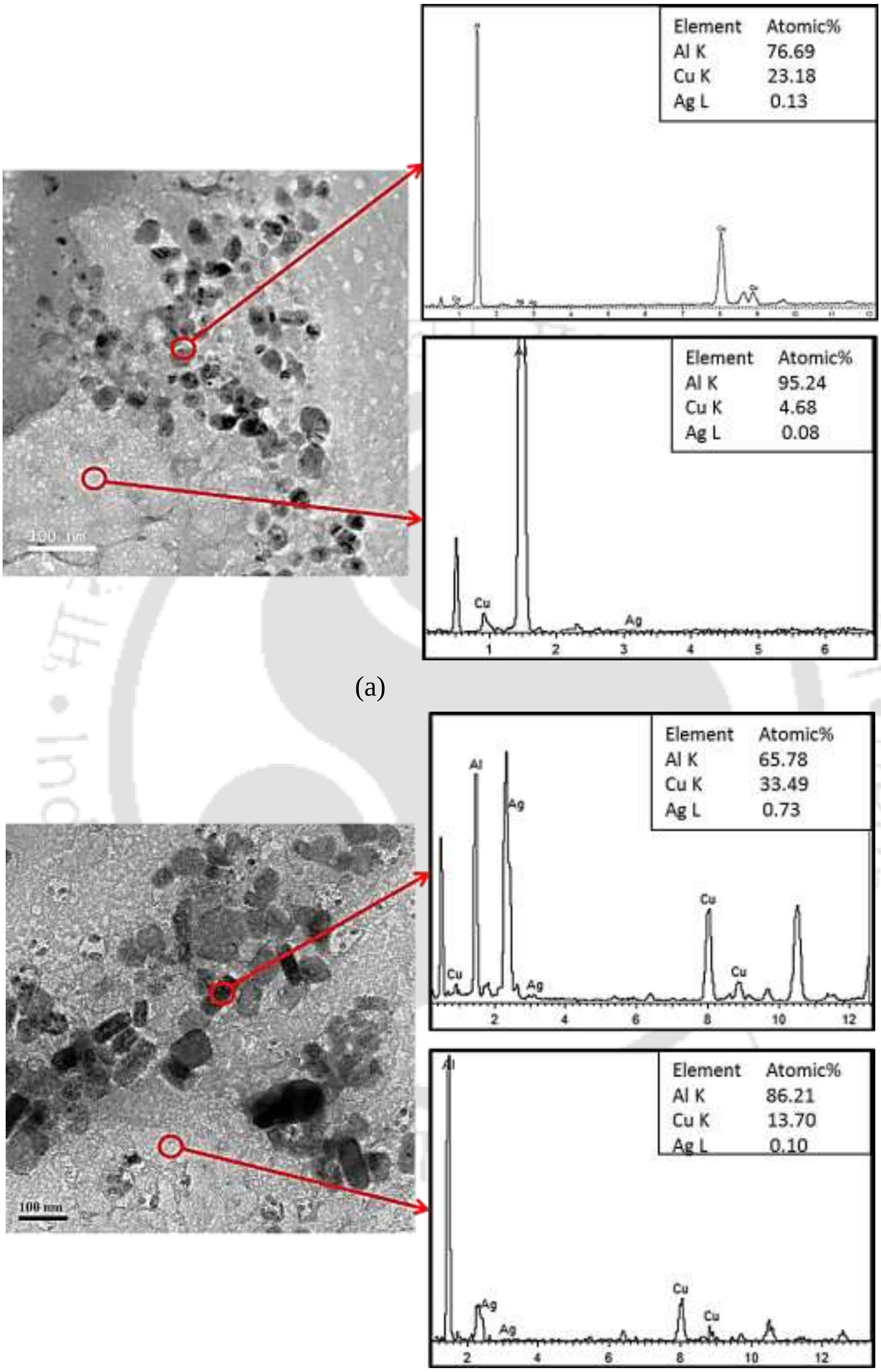

(a)

(b)

Figure 4.16 Bright field transmission electron microscope (TEM) precipitates phase, micrograph and energy dispersive X-ray spectra (EDS) of matrix of Alloy-D after (a) solution heat treatment and (b) at peak ageing

The microstructures of the cast alloys reveal the lower of the script-like second phase which could be observed in the cast alloys as well as in the solutionized (Figure 4.6 and Figure 4.7). During solution heat treatment, the low melting point phases present in the cast alloys (Figure 4.1, 4.2 and 4.4) dissolve in the matrix forming a super-saturated solid solution. The cooling rate is very fast during the water quench. Due to this the alloying elements from the super saturated solution do not have sufficient time to diffuse out and is retained in the solid solution resulting in a strained matrix. The high hardness values observed for the solution heat treated alloys are attributed to the supersaturated solid solution. The increasing trend in hardness value with silver addition is due to higher level of supersaturation resulting in higher lattice strain. It is possible for elemental silver to segregate at the grain boundary region. Since silver addition was in trace amounts, the amount of hardness increase was not substantial.

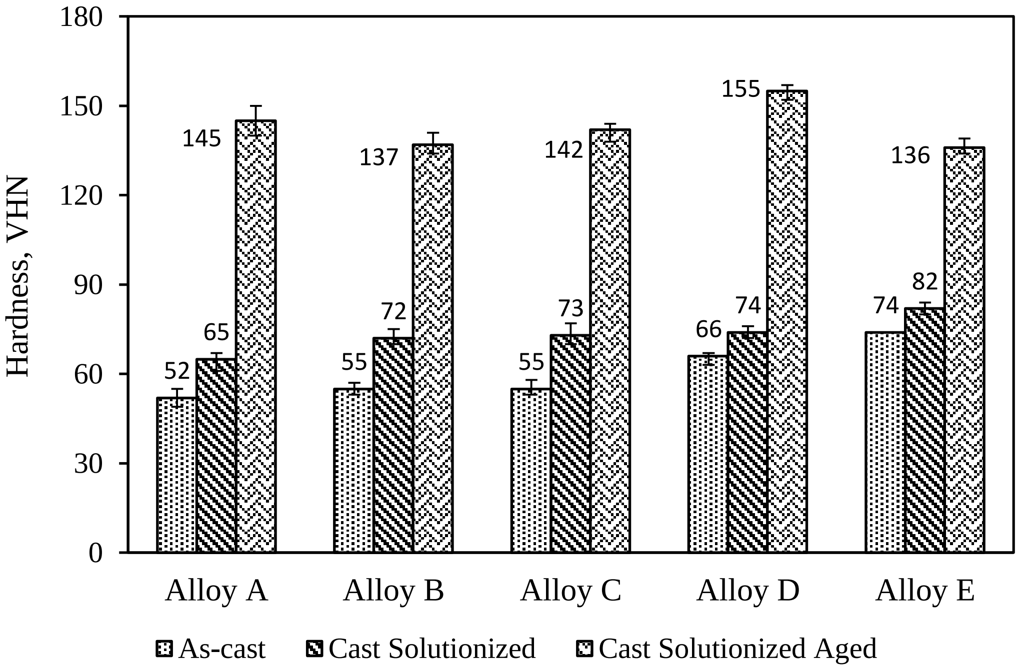

Figure 4.17 Variation of hardness for the cast alloys under different heat treatment conditions

Rolling results in an increase in hardness of the alloys. No significant variation in hardness versus sliver content of alloys is observed in the as-rolled condition (Figure 4.18). Solution heat treatment resulted in substantial increase in the hardness of the rolled alloys. The hardness of the rolled and solution heat treated alloys increases with increase in wt.% silver. The hardness of as-rolled Alloy-A and Alloy-E increased by 48% and 70%, respectively after solution heat treatment. The trend in the hardness variation of the rolled alloys indicates that silver addition increases the hardness of the aluminum alloys by solid solution strengthening. Age hardening heat treatment resulted in further increase in hardness for all the alloys. The variation in the hardness versus silver (Ag) content in the alloy after age-hardening was only marginal. The maximum increase in hardness was achieved for the Alloy with 0.07 wt.% silver (Alloy-D). The results indicate maximum hardness was achieved for all alloys in the precipitation hardened conditions.

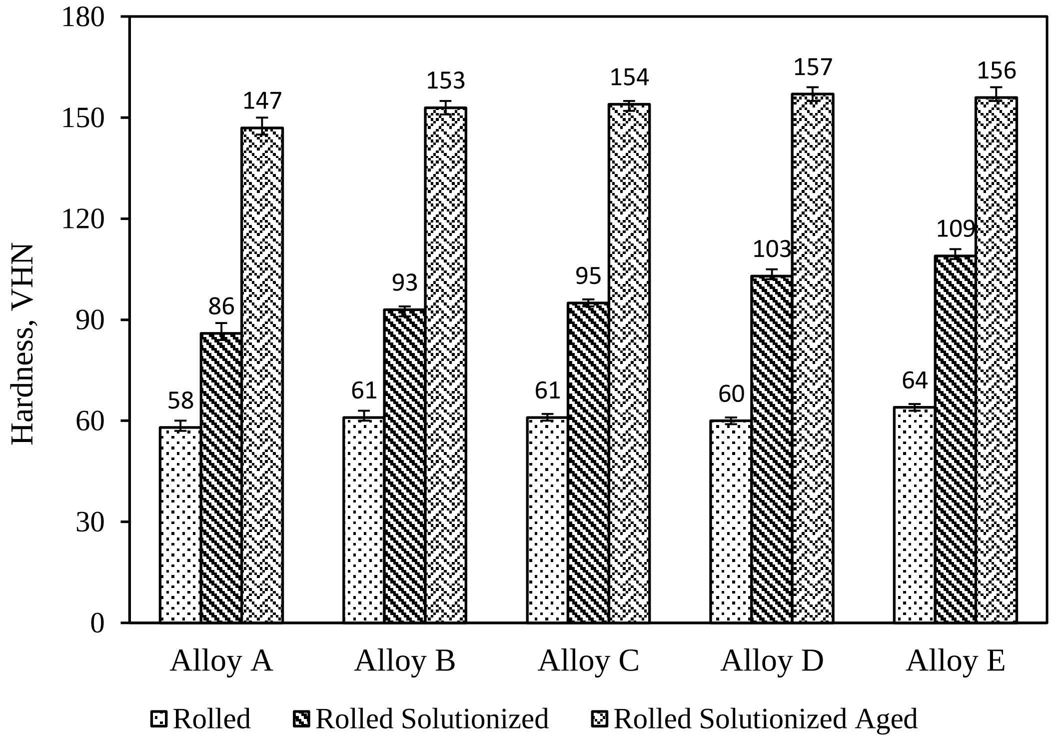

Figure 4.18 Variation of hardness for the rolled alloys under different heat treatment conditions

Earlier studies revealed that the solutionizing heat treatment resulted in strong interaction between silver and vacant lattice sites of aluminum leading to their retention in the supersaturated solid solution of Al-Cu-Mg alloy containing 0.1 wt.% silver [25]. The initial stage of age hardening in the present alloys is very rapid. Figure 4.11 reveals that around 76% of the peak hardness values were achieved during the first 5 hours of ageing for all alloys containing silver. Subsequent ageing resulted in increase in hardness but at a slow rate till the peak hardness was achieved. The study also revealed that age hardening in Al-1.1Cu-1.7Mg-(0.1Ag) alloy which falls within the α+S phase of the ternary phase diagram, occurs in two distinct stages. The first stage of hardening is very rapid which occurs by cluster hardening and is completed within a very short time interval [25].

During the age hardening of Al-Cu-Mg-alloys containing silver, co-clustering of silver and Mg occurs and the co-clustering does not include copper atoms [24, 25]. Binary Al-Ag phase diagram [116] indicates silver as a substitutional impurity in aluminum lattice which can result in solid solution strengthening. Age hardening results in diffusion of silver into the precipitates from the matrix resulting in further increase in hardness for the alloys.

4.2.2 Tensile test results

Uniaxial tensile tests of cast, rolled and different heat treated alloys were carried out using a 100 kN capacity universal testing machine. The details of the tensile tests have been described in Section 3.1.2. The tensile test results and mode of factures are discussed in this section.

4.2.2.1 Tensile test results for the cast alloys

The tensile test results for the cast alloys are shown in Table 4.3. Figures 4.19 (a), (b) and (c) shows the plots of the variation of yield strength (YS), ultimate tensile strength (UTS) and percentage elongation versus wt.% of silver in the cast alloys under different heat treatment conditions. The plots do not indicate any specific trend in the variation of yield strength and ultimate tensile strength with silver content in the as-cast condition. In the solutionized condition, the yield strength (YS) of the alloy increases slowly with increase in silver content. With the addition of 0.1 wt.% (Alloy-E), the yield strength of the alloy increases by 10%. The variation of ultimate tensile strength of the alloy in the cast and solutionized condition is also not showing any specific trend with silver content in the alloy. Figure 4.19 (c) shows the variation of percentage elongation versus silver content in the cast alloy at different heat treatment conditions. The ductility of the as-cast alloys are below 2%. Though the ductility of the cast alloy after solutionizing is higher than the as cast alloy, no specific trend in the variation of the ductiity can be observed. The ductility of the cast alloys are observed to be the lowest in the precipitation hardened condition. The variation in the yield strength, ultimate tensile strength and percentage elongation in the cast alloys not showing any specific trend may be due the presence of micro-porosities in the alloy matrix formed during the casting process.

4.2.2.2 Tensile test results for the rolled alloys

Tensile properties of the rolled alloys have been presented in Table 4.4. Rolling results in considerable increase in yield strength (YS) and ultimate tensile strength (UTS) of the as cast alloys. Figure 4.20 shows the variation of yield strength with wt.% silver for the as-rolled Al-alloys. Yield strength increases with increase in wt.% silver in the alloy. As the silver content increases from 0 wt.% to 0.1 wt.% the yield strength increases from 106 MPa to 138 MPa, i.e. an increase of around 30% is observed. Rolling results in improvement of the microstructure by: (i) elimination of the porosities ; (ii) fracturing of the intermetallic phases to form fine particles in the matrix and (iii) uniform dispersion of the fine intermetallic phases in the matrix. This results in increased strength of alloy, in addition to the increase in with increase in silver content. The ultimate tensile strength of as-rolled alloys with the silver addition is found to be lower than that of the base alloy.

The yield strength of rolled alloys increase with solution heat treatment with the exception of Alloy-D containing 0.07 wt.% silver (Table 4.4). The reason for this trend is the same as that of the variation in hardness explained in Section 4.2.1. It may be noted that the grain size of the solution heat treated alloy is higher than the as-rolled alloys. As per the Hall-Petch relationship, lower yield strength is expected for the solution treated alloy. However, the higher yield strength observed for the solution heat treated alloys indicates higher solid solution strengthening effect for the present alloys. Solution heat treatment results in increased ultimate tensile strength for all the alloys. However, only a marginal variation in the ultimate tensile strength was observed with the addition of silver in the alloy matrix.

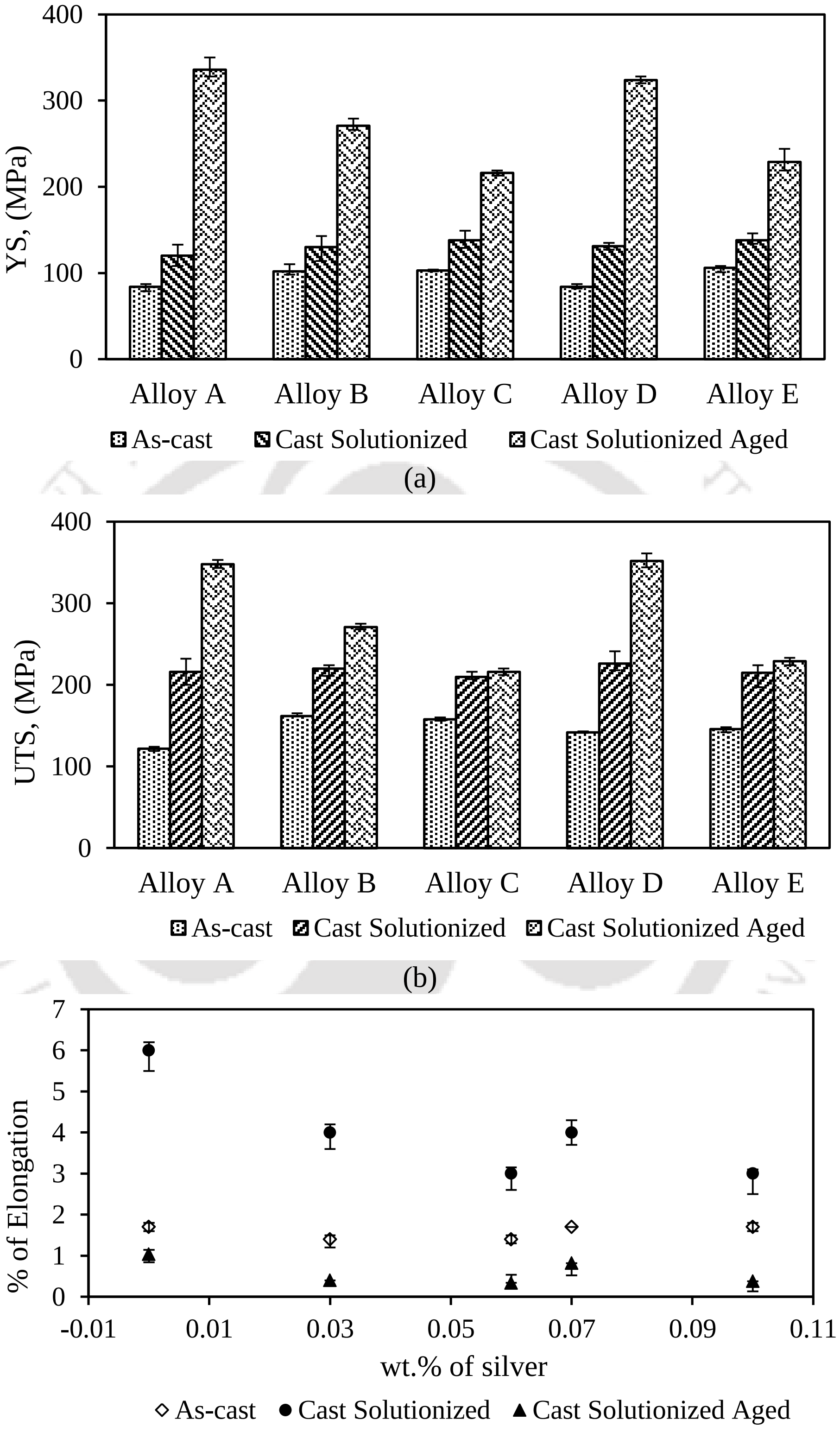

(a)

(b)

(c)

Figure 4.19 Histogram plots of (a) yield strength and (b) ultimate tensile strength and (c) percentage elongation of the cast alloys under different cast and heat treated condition

Figure 4.20 indicates that the yield strength of the solution heat treated cast and rolled alloys increases considerably by age hardening. As the silver content into the alloy increases from 0 wt.% to 0.07 wt.%, the yield strength increases from 328 MPa to 376 MPa. Yield strength decreases with further addition of silver in the alloy. During the age hardening process, the dissolved elements precipitate out of the super saturated matrix resulting in fine second phase precipitates. The present trend of increase in yield strength with up to 0.07 wt.% silver (Alloy-D) in the alloy indicates the contribution of silver in the age hardening process. Age hardening results increase in ultimate tensile strength for all the alloys compared to the solution heat treated alloy. The maximum ultimate tensile strength of the age hardened alloy was observed for the Alloy-D, where the heat treatment resulted in an increase of ultimate tensile strength by 34% compared to the base alloy.

It can be seen from Table 4.3, that the elongation to failure for the as-cast alloys are less 2% indicting poor ductility. Solution heat treatment improves the ductility of the as-cast alloys. The maximum ductility after solutionizing is observed for Alloy-A. The ductility decreases with increase in silver content in the alloy. It is seen that rolling results (Table 4.4) in improvement of the ductility of the cast and solutionized alloys. Alloy-D exhibits the maximum ductility in the as-rolled condition where, the elongation to failure is 16%. Solution heat treatment results in an increase in the ductility for all the rolled alloys. The ductility of the rolled and solution heat treated alloy remained almost same with silver content up to 0.07 wt.%. Further increase in the silver content results in sharp decrease in the ductility. It is observed that the ductility of the rolled and solutionized alloys decreases after age hardening. Alloy-D exhibits the maximum ductility after age hardening with 10% elongation.

Silver addition into the base alloy has two effects: (i) it acts as a substituitonal impurity in the α phase as evident from 4.16 and (ii) it aids in co-clustering resulting in the formation of GP-zones which is coherent with the matrix during the quench stage. Both these effects enhance the strength by solid solution strengthening. The energy dispersive X-ray spectra (EDS) result (Figure 4.16) of Alloy-D after ageing for 45 hours reveals further enrichment of $CuAl_2$ phase with silver (0.73 at.% silver). This occurs by the diffusion of silver into the $CuAl_2$ phase from the matrix. Age

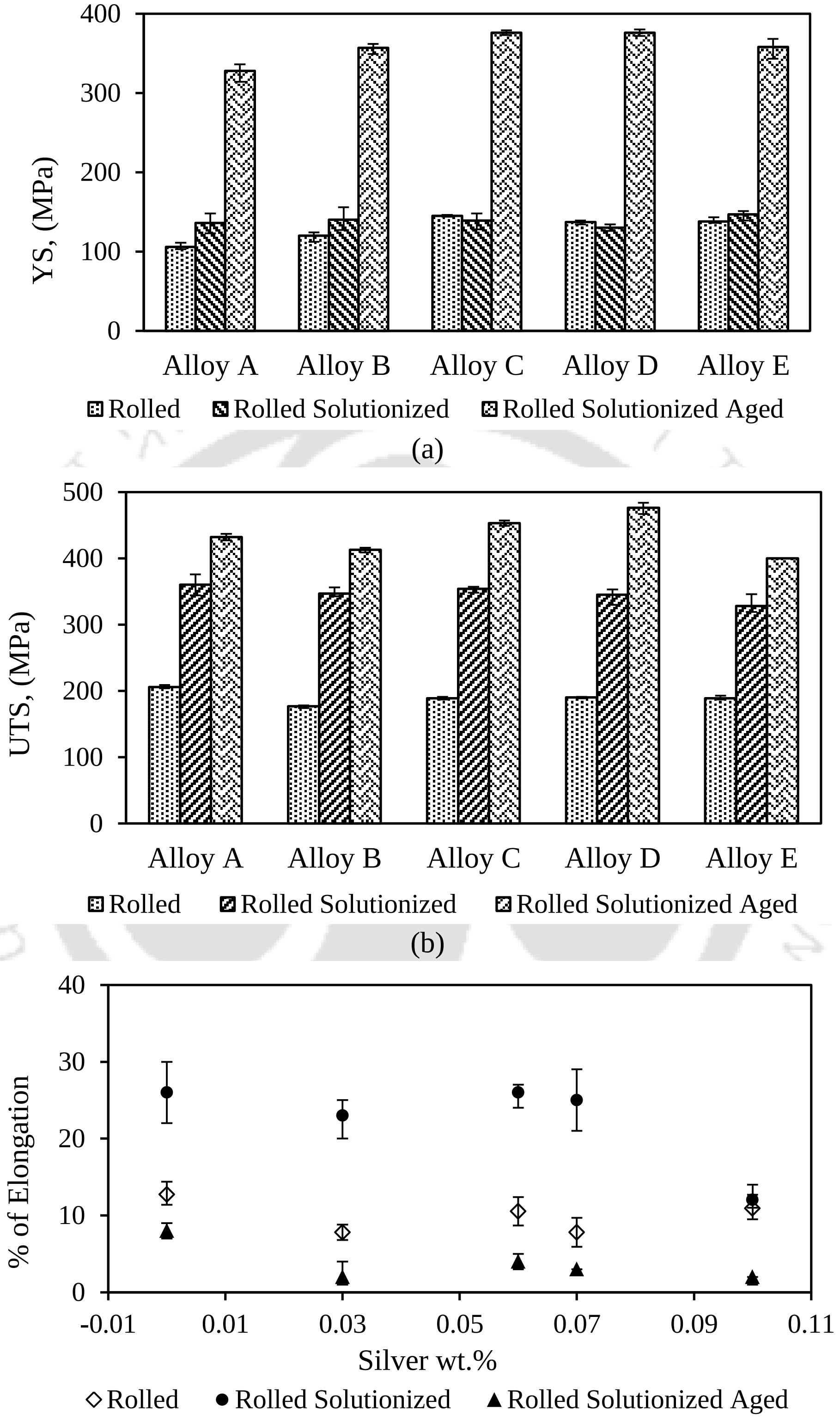

(a)

(b)

(c)

Figure 4.20 Histogram plots depicting (a) yield strength and (b) ultimate tensile strength and (c) percentage elongation of the rolled alloys under different heat treated condition hardening results in coarsening of the precipitates accompanied by a morphological change. The coherent precipitate-matrix interface during the initial stage of hardening changes to a semi-coherent interface while attaining the peak hardness. With extended ageing, the precipitate size increases and the particles are no longer coherent with the matrix resulting in decrease in the strength during the over-aging stage. The highest strength is achieved for the alloys when age hardened for 45 hours.

The mechanical properties of the alloy with 0 wt.% silver is almost same as that reported for the 2219 Al alloy [1]. The best combination of mechanical properties is obtained for Alloy-D, where an increase of around 15% increase in the yield strength and ultimate tensile strength along with good ductility is observed compared to the base alloy.

4.2.2.3 Fractography

Tensile fracture surface observation using scanning electron microscope (SEM) revealed similar fracture features for all alloys under the same processing conditions. Figure 4.21 (a) & (b) shows the fractographs of as-cast Alloy-D. Low magnification observation revealed a brittle or cleavage mode of fracture features. The fracture features indicate inter-granular failure. Voids at the second phase particle-matrix interface regions are also evident. The presence of very fine micro-porosities is expected from this wrought alloy in the as-cast condition. The microstructure of the samples (Figure 4.3) also reveals very fine micro-porosities/shrinkage cavities at grain boundary regions, which are formed during the solidification process. It has been reported that coarse brittle phases along the grain boundaries and any pre-existing shrinkage cavities are possible sites of failure initiation during the tensile loading. Presence of large number of micro-shrinkage cavities, coarse $CuAl_2$ phases and other intermetallic phases at grain boundary regions (Figure 4.2) in present as-cast alloys act as failure initiating micro-cracks. During the tensile loading these micro-cracks propagate through the grain boundaries resulting in inter-granular fracture. Crack propagation through the grain boundaries are faster compared to that through the grains. Since the sizes of the shrinkage porosities were large, the material failed at low strains resulting in the low ductility associated with the cast alloys.

Tensile fractographs of Alloy-D has been shown in Figure 4.21 (c) & (d) of rolled and solution heat treated condition. The features exhibits dimple features typical of ductile failure mode. High magnification image, as seen from Figure 4.21 (d) shows fine intermetallic particles at dimple regions indicating the failure process by micro-void coalescence, typical of ductile failure. The microstructure of the rolled and solution heat treated samples (Figure 4.7) reveals uniform distribution of fine intermetallic second phase particles in the alloy matrix. During the tensile loading, voids nucleate at the particle-matrix interface regions. Further loading results in the growth of these voids through the grains and finally coalesce to cause the final failure. The growth of the micro-voids before the final failure results in improved ductility for alloys. This is in agreement with the increased elongation values for the rolled and solution heat treated specimens.

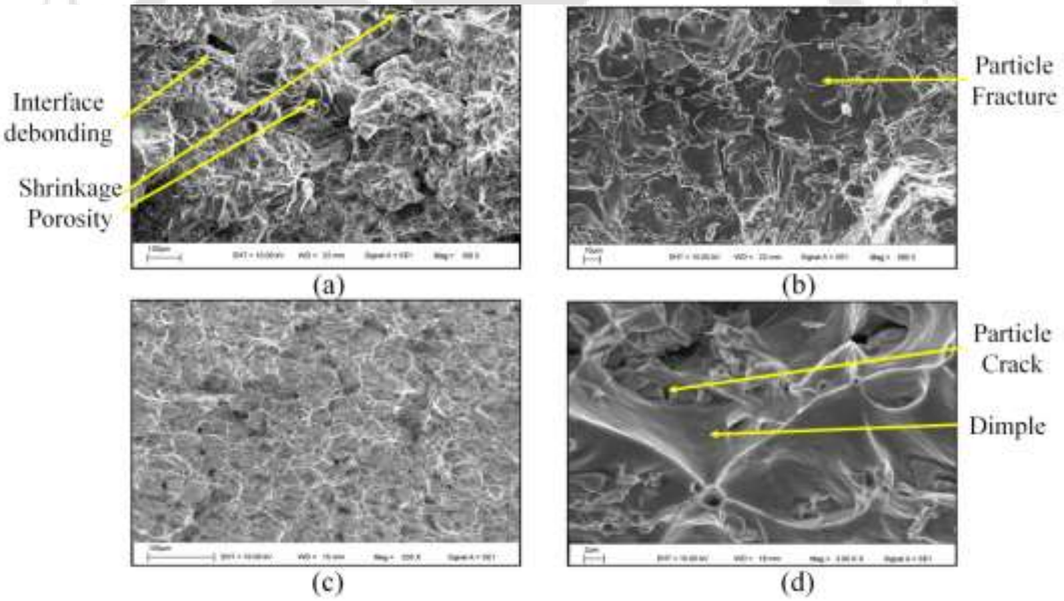

Figure 4.21 Tensile fractographs of Alloy-D in the (a) & (b) as-cast condition, (c) & (d) rolled and solutionized condition

Table 4.3 Variation of tensile properties with addition of silver (Ag) of alloys in cast and cast-heat treated conditions

Ag content (wt.%)	As-cast alloy				Cast and solutionized alloy				Cast- solutionized-Aged			
	YS (MPa)	UTS (MPa)	Elongation (%)	E (GPa)	YS (MPa)	UTS (MPa)	Elongation (%)	E (GPa)	YS (MPa)	UTS (MPa)	Elongation (%)	E (GPa)
0	84	133	1.57	68.2	126	243	6.0	70	336	348	1.04	72.5
0.03	101	166	1.79	74.3	130	231	3.8	74	271	271	0.4	73.3
0.06	103	158	1.4	72.1	138	210	3	69.7	216	216	0.34	70.1
0.07	77	130	1.75	76.6	131	226	3.7	68.8	324	352	0.82	68.6
0.1	90	146	1.72	72.7	138	215	2.4	74.2	229	229	0.38	67.4

Table 4.4 Variation of tensile properties with addition of silver (Ag) of alloy in rolled and rolled heat treated conditions

Ag content (wt.%)	As-Rolled				Rolled and Solutionized				Rolled- solutionized-Aged			
	YS (MPa)	UTS (MPa)	Elongation (%)	E (GPa)	YS (MPa)	UTS (MPa)	Elongation (%)	E (GPa)	YS (MPa)	UTS (MPa)	Elongation (%)	E (GPa)
0	106	206	14.4	80.3	136	344	26.0	77	328	421	8.5	71.3
0.03	120	176	13.3	76.5	140	356	22.5	84	357	412	3.6	83
0.06	145	189	10.5	77.4	139	354	26.0	76.6	376	453	4	76.1
0.07	137	190	16.0	80.8	130	353	25.3	77	376	476	10.5	83.5
0.1	138	189	12.7	76.6	147	346	12.3	78	358	400	1.5	87

4.3 Hot deformation behavior

The results of hot compression tests at various strain rates and temperatures of 2219 aluminum alloys microalloyed with silver are illustrated and discussed in the following subsection by means of flow curves. Different stages of flow curves are described in detail. The development and the analysis of the constitutive equation relating flow stress (σ), deformation temperature (T), strain rate ($\dot{\varepsilon}$), Zener–Hollomon parameter (Z) and activation energy for deformation (Q) are discussed.

4.3.1 Flow stress behavior

The true stress versus true strain (σ–ε) curves obtained for the alloys during compression testing at various strain rates and temperatures are shown in Figure 4.22 to 4.26. The flow cure for all the alloys for a particular combination of strain rate and temperature follows the same trend. However, the flow stress for Alloy-A is always higher than the alloys containing silver for all combination of strain rate, strain and temperature.

At 300 °C and 350 °C for strain rate 0.001 s^{-1}, the flow stress increases with strain till a maximum value is reached. Further increase in strain results in a gradual decrease in flow stress. For the same temperatures range and at higher strain rates, the flow stress increases continuously with increase in strain. At 400 °C and strain rate of 0.001 s^{-1}, the flow curves shows a continuous increase in flow stress till a strain of 0.2. The flow stress decreases with further increase in strain. At strain rates $\geq$ 0.01 s^{-1} and 400 °C, the flow stress increases with strain and after attaining a peak value remains almost constant. For deformations above 400 °C and strain rates $\geq$ 0.01 s^{-1}, after reaching a maximum value the flow stress started decreasing slowly with increase in strain, indicating flow softening. The flow softening increased with increase in temperature. The figure also indicates that the strain to reach the peak flow stress decreased with increase in temperature.

From the flow curves flow stress increases with strain (up to a certain value) is due to strain hardening. Strain hardening occurs due to the generation of dislocations explained by Frank-Read source and pile up of dislocation on the slip planes at barriers. The barriers for the movement of dislocations are generally immobile dislocations, second phase particles in the matrix, fine second phase precipitates, grain boundaries in polycrystalline materials, twin boundaries, etc. The pile up of dislocation results in the existence of back stresses which opposes the applied stress on the slip plane resulting in strain hardening. At lower temperatures the strain hardening is more pronounced due to the above mentioned phenomenon. As temperature is increased, various thermal assisted mechanism starts operating leading to reduction in the dislocation density in the material resulting in flow softening. At this stage, dislocations can surpass the obstacles by various mechanisms like dislocation climb, annihilation of dislocations when dislocations with opposite nature meets and also by diffusion of elements along the crystal lattice due to the increased density of vacancies. Researchers have attributed that at high temperatures flow softening occurs due to one or more of phenomena like dynamic recovery, dynamic recrystallization and superplastic deformation; this can offset the effect of work hardening.

The early stages of plastic deformation are accompanied by rapid dislocation multiplication resulting in work hardening leading to a rapid rise in the flow stress. As dislocation density increases with further deformation, rate controlled phenomenon like dynamic softening occurs that offsets the effect of work hardening [121–123]. Due to this the flow stress increases at a decreasing rate until it attains a peak value. With further increase in strain the flow stress almost remained constant indicating a balance between working hardening rate and softening rate. For a constant strain, the flow stress increased with decrease in temperature. For deformations above 400 °C and strain rate 10^{-2} s^{-1}, after reaching the maximum value the flow stress decreased gradually with increase in strain, indicating flow softening. The flow softening increased with increase in temperature. The figure also indicates that the strain to reach the peak flow stress decreased with increase in temperature. For a given strain rate the driving force for dynamic softening, which counteracts work hardening, increases with increase in temperature. This results in a decrease in the peak stress and the overall flow stress at higher temperatures [121–123].

The peak flow stress versus temperature plots for Alloy-A and Alloy-E for different strain rates has been shown in Figure 4.27. The peak stress decreases linearly with increase in temperature for all strain rates. It is evident from Figure 4.23 to Figure 4.26 that the flow stress decreased with addition of silver into Alloy-A, for any combination of temperature, strain and strain rate.

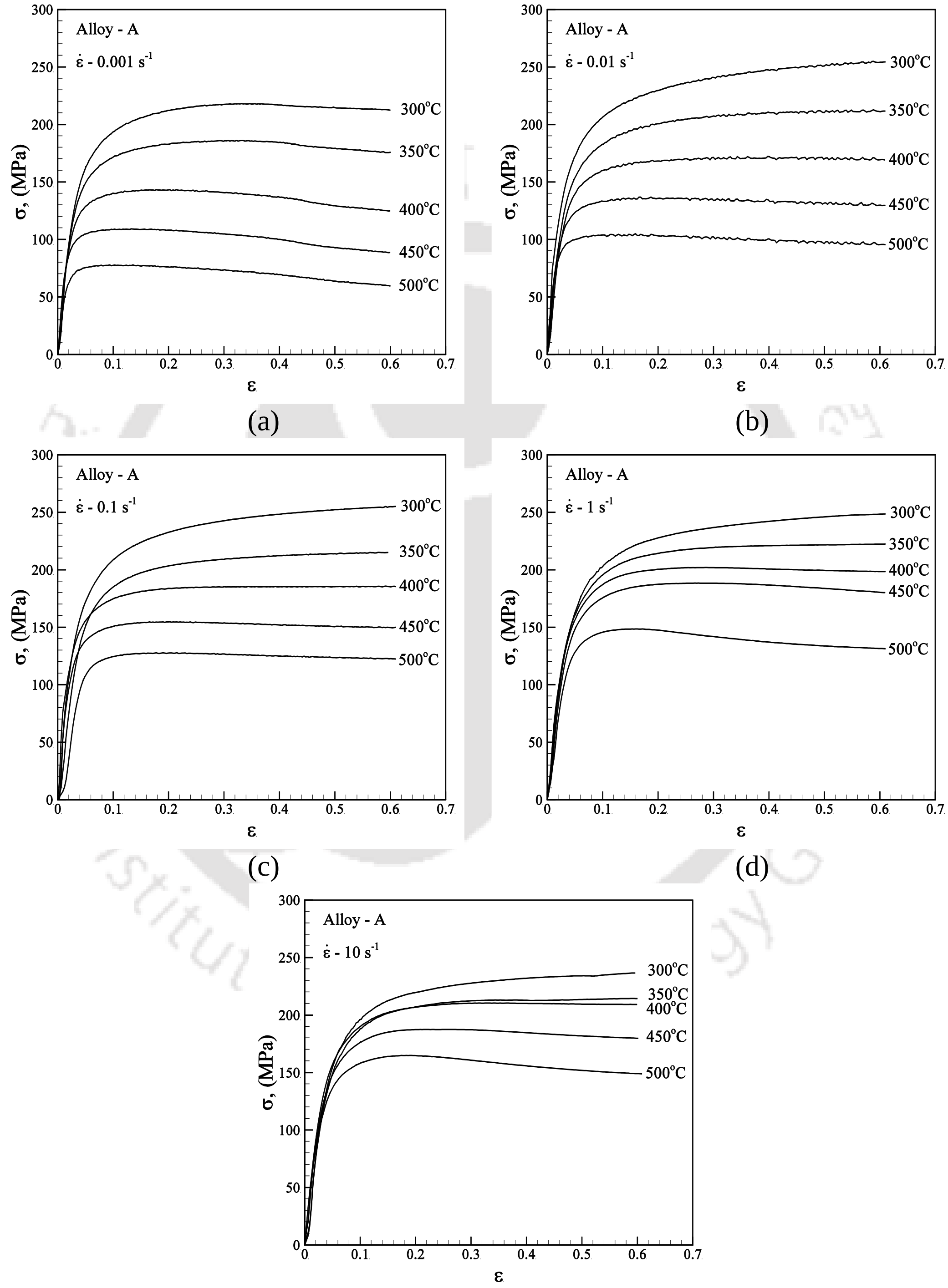

(a) (b) (c) (d) (e)

Figure 4.22 Stress strain (σ vs. ε) curves for Alloy-A at strain rates (a) 0.001 s^{-1}, (b) 0.01 s^{-1}, (c) 0.1 s^{-1}, (d) 1 s^{-1} and (e) 10 s^{-1}

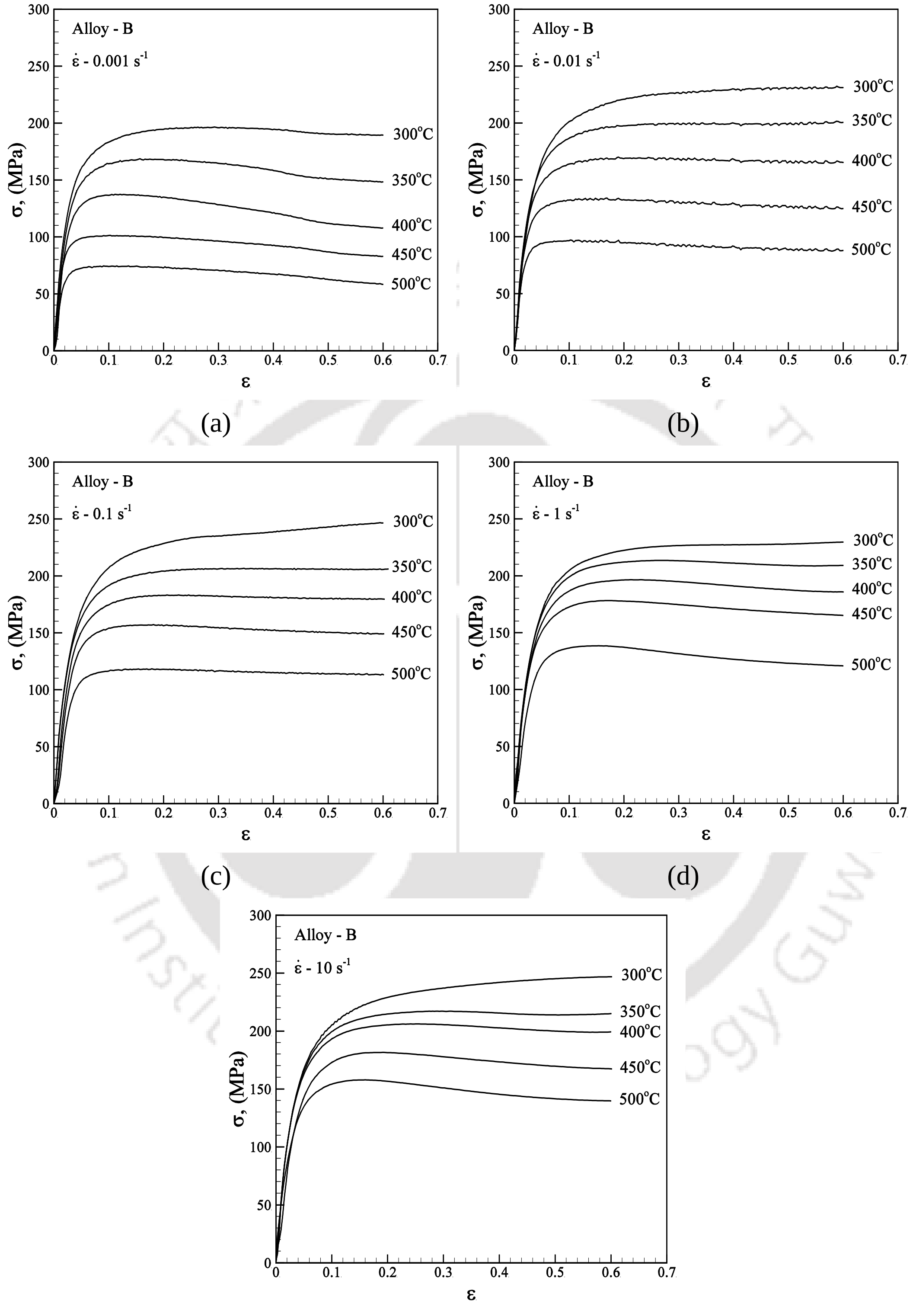

(a)

(b)

(c)

(d)

(e)

Figure 4.23 Stress strain (σ vs. ε) curves for Alloy-B at strain rates (a) 0.001 s^{-1}, (b) 0.01 s^{-1}, (c) 0.1 s^{-1}, (d) 1 s^{-1} and (e) 10 s^{-1}

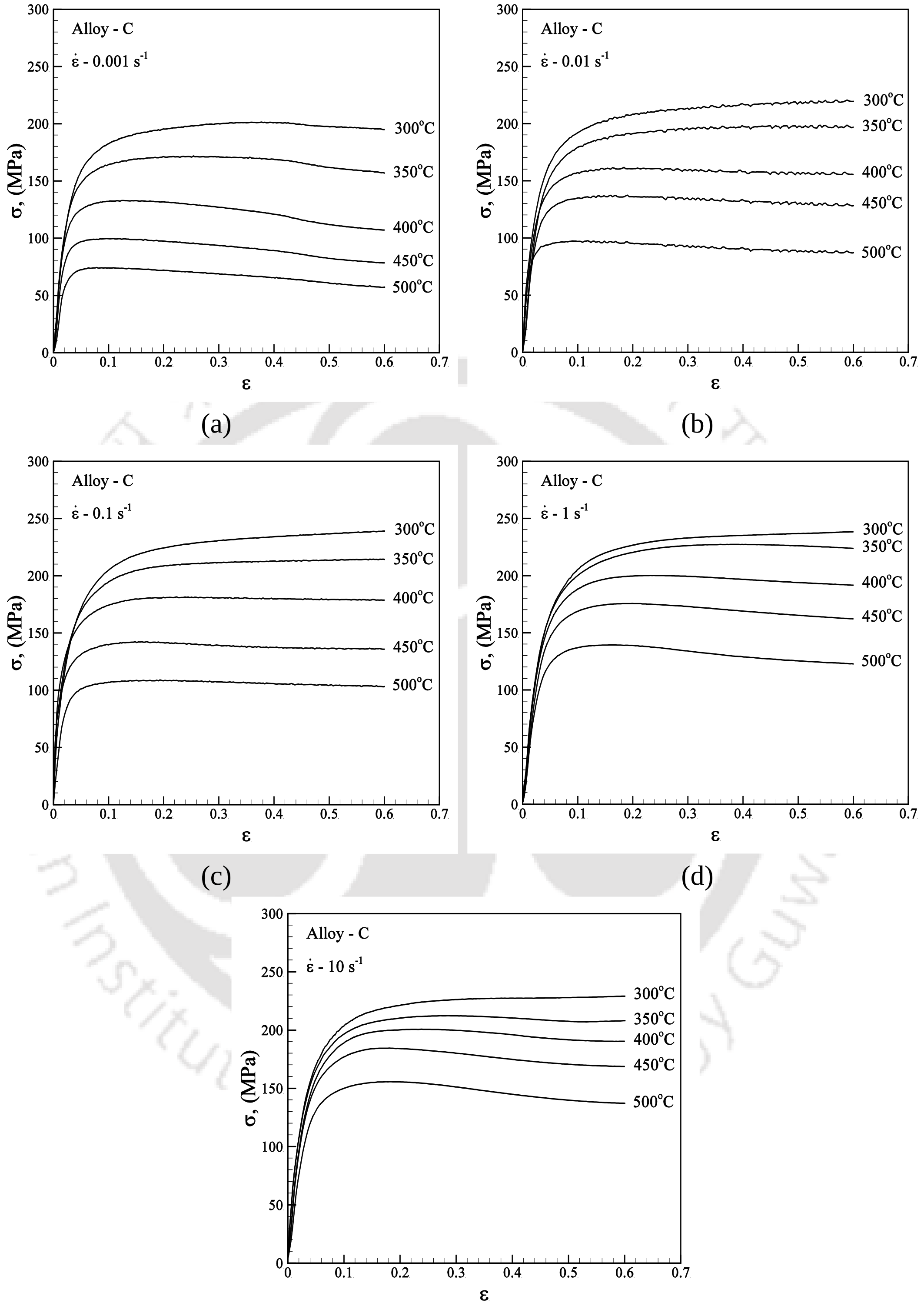

(a) (b)

(c) (d)

(e)

Figure 4.24 Stress strain (σ vs. ε) curves for Alloy-C at strain rates (a) 0.001 s^{-1}, (b) 0.01 s^{-1}, (c) 0.1 s^{-1}, (d) 1.0 s^{-1} and (e) 10 s^{-1}

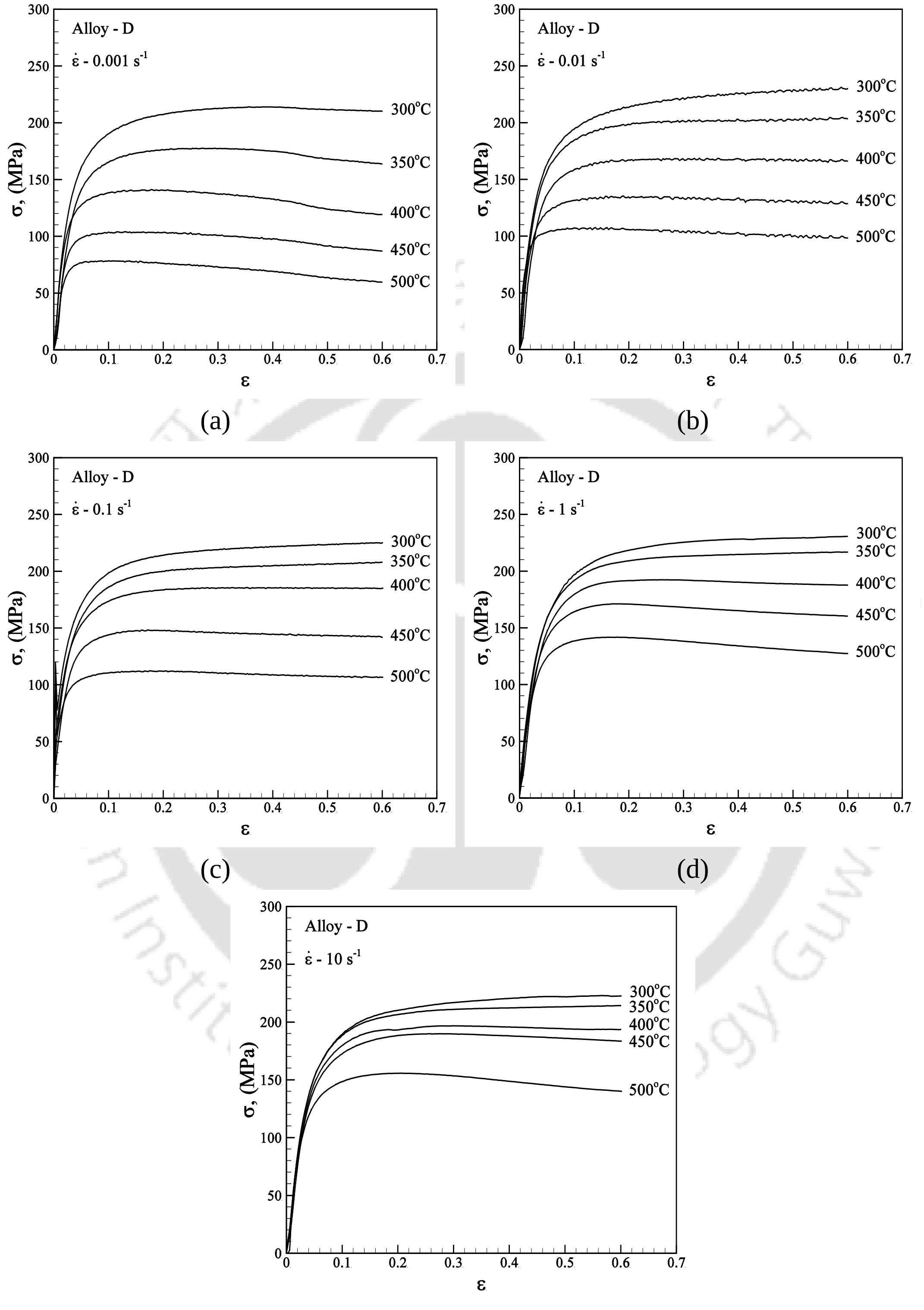

(a) (b) (c) (d) (e)

Figure 4.25 Stress strain (σ vs. ε) curves for Alloy-D at strain rates (a) 0.001 s^{-1}, (b) 0.01 s^{-1}, (c) 0.1 s^{-1}, (d) 1 s^{-1} and (e) 10 s^{-1}

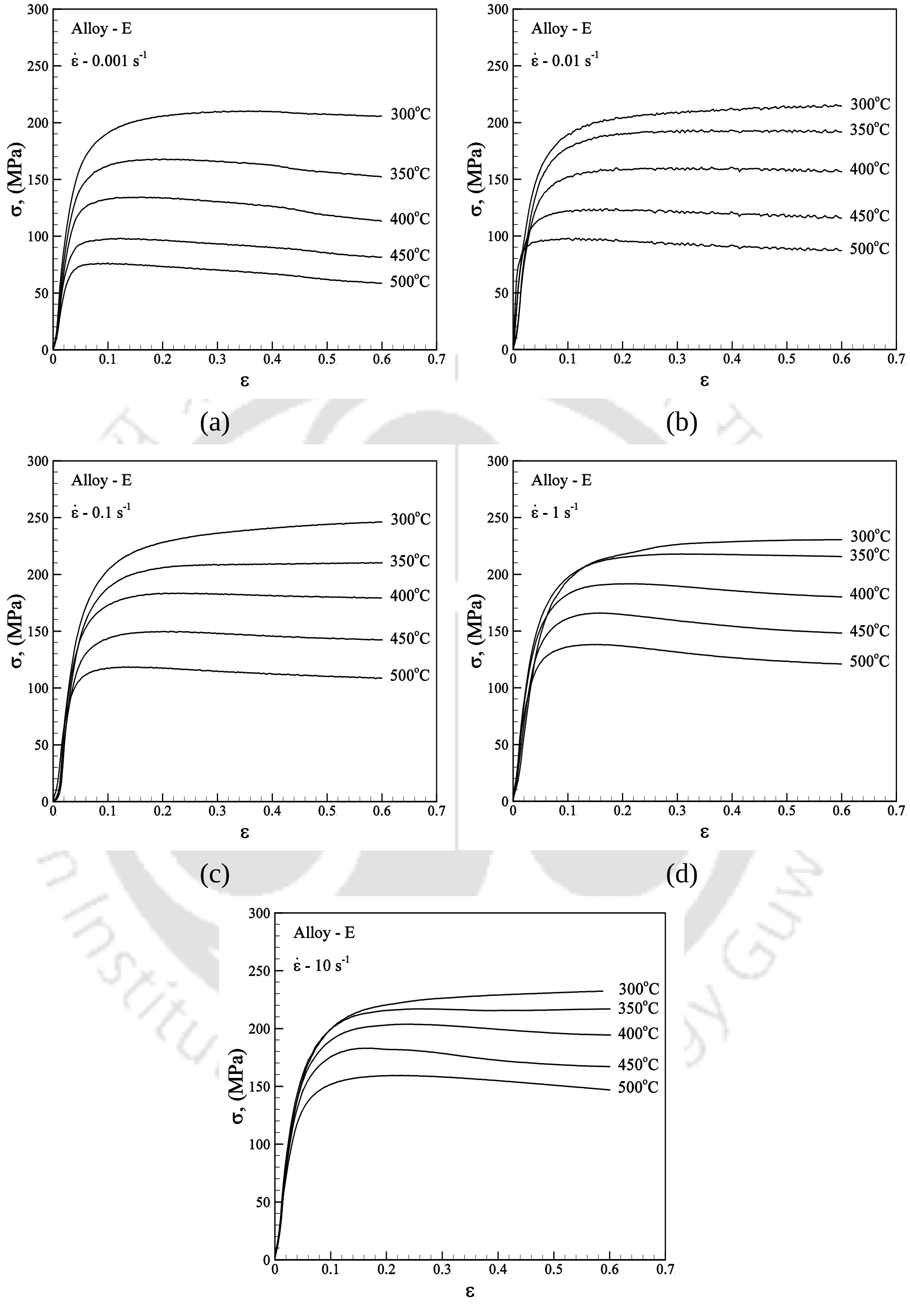

(a)

(b)

(c)

(d)

(e)

Figure 4.26 Stress strain (σ vs. ε) curves for Alloy-E at strain rates (a) 0.001 s^{-1}, (b) 0.01 s^{-1}, (c) 0.1 s^{-1}, (d) 1 s^{-1} and (e) 10 s^{-1}

However, the variation of decrease in flow stress with silver content is small. The average decrease in flow stress between alloy-A and Alloy-E is 5%, with a maximum decrease in flow stress being 15%, when tested at 400 °C and strain rate of 0.01 s^{-1}. Extensive transmission electron microscopic studies by Murayama et al. [117] revealed that addition of 0.1 wt.% silver in Al-Cu-Mg alloy resulted in a drastic decrease in dislocation density. Silver forms substiutional alloy in aluminum matrix. This results in decrease in dislocation density leading to lower flow stress with the addition of silver.

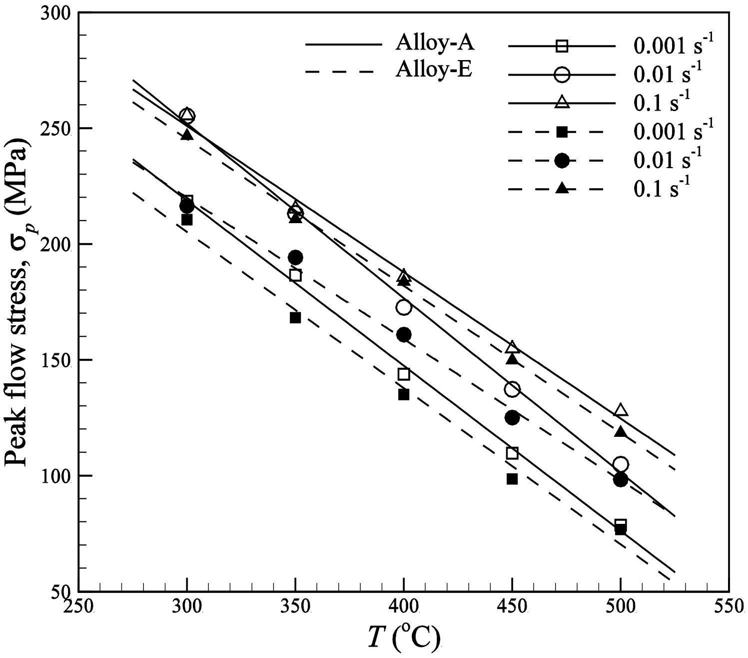

Figure 4.27 Peak flow stress versus temperature plots for Alloy-A and Alloy-E

Stress-strain curves of Alloy-A and Alloy-E at 400 °C for different strain rates are plotted in Figure 4.28 (a) and Figure (b), respectively. The curves indicate continuous increase in flow stress during the deformation for both alloys at strain rates above 10^{-2} s^{-1}. The peak flow stress is highest when strained at a strain rate of 10^{1} s^{-1} and decreases with decrease in strain rates. For deformations carried out at strain rate of 10^{-3} s^{-1} the flow stress increased up to a strain of around 0.3 and decreased with further increase in strain. The initial work hardening stages was followed by flow softening, when deformed at very low strain rate. For a given temperature, the greater the strain rate, the higher the peak flow stress. It has been reported that at higher strain rates dislocation generation rate increases during the plastic deformation. This leads to the formation of dislocation tangles which act as barrier for dislocation movement resulting in higher peak stress at higher strain rates and lower temperatures [121–123].

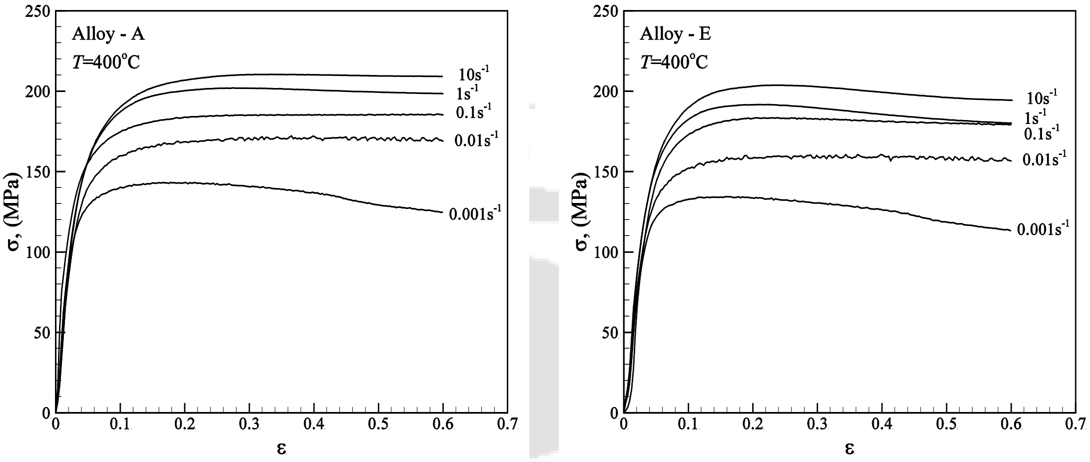

(a) (b)

Figure 4.28 Stress-strain (σ vs. ε) plots at 400 °C temperature and different strain rates for (a) Alloy-A and (b) Alloy-E

The stress-strain plots for Alloy-A and Alloy-E, when deformed at 500 °C for various strain rates are shown in Figure 4.29 (a) and Figure (b) respectively. All the curves indicate that the flow curves initially increases with strain, reaches a maximum value and then decreases with further increase in strain. It is attributed that at high

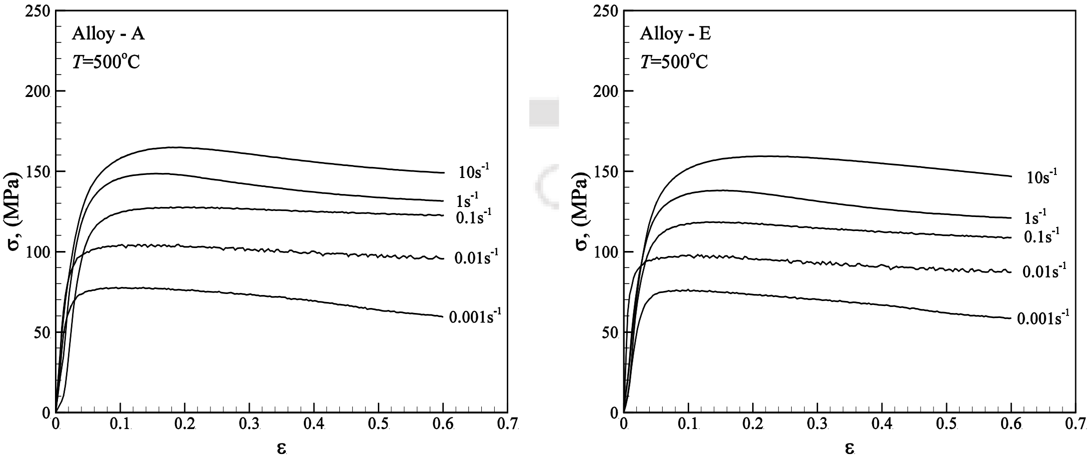

(a) (b)

Figure 4.29 Stress-strain (σ vs. ε) plots at 500 °C temperature and different strain rates for (a) Alloy-A and (b) Alloy-E temperatures, flow softening occurs due to dynamic recovery or dynamic recrystallization and this can offset the effect of work hardening. Dynamic softening is a common phenomenon during deformation of aluminum alloys at elevated temperature.

4.3.2 Constitutive equations

Various models have been proposed to describe the high temperature deformation behavior of metallic materials. The constitutive models establishes the functional relationship between variables viz., strain rate ($\dot{\varepsilon}$), deformation temperature (T), activation energy (Q) and flow stress (σ). During isothermal compression at elevated temperatures, the general flow behavior can be expressed by the Arrhenius type of equation expressed (*cf*. section 2.6.1) as [19, 61]

$$\dot{\varepsilon} = Af(\sigma)\exp\left(-\frac{Q}{RT}\right), \tag{2.8}$$

where Q is the activation energy for deformation, R is the universal gas constant, T is the deformation temperature (in K), $f(\sigma)$ is a function of stress and A is a constant. Researchers have proposed various expressions for the stress function $f(\sigma)$. However, depending on the alloy, any of following expressions (*cf*. section 2.6.1) have been found suitable [19, 27, 60]:

$$f(\sigma) = \sigma^{n_1}. \tag{2.9}$$

$$f(\sigma) = \exp(\beta\sigma). \tag{2.10}$$

$$f(\sigma) = \left[\sinh(\alpha\sigma)\right]^{n}. \tag{2.11}$$

where n, n_1, and β are the constants and α is the stress multiplier. The power law relation, Eq. (2.9), is valid only for high temperature and low strain rates, where the stresses are low (i.e. $\alpha\sigma < 0.8$) and breaks down at low temperatures and high stain rates. Equation (2.10) is valid for deformations at low temperatures and high strain rates where the stresses are high ($\alpha\sigma > 1.2$) and breaks down at conditions of high temperature and low strain rates. Over a wide range of stresses, the most suitable expression for aluminum alloys is found to be the hyperbolic sine function given by

Eq.(2.11). Substituting Eq.(2.11) into Eq.(2.8), the following constitutive equation is obtained for the high temperature deformation behavior of aluminum alloys:

$$\dot{\varepsilon} = A\left[\sinh(\alpha\sigma)\right]^{n} \exp\left(-\frac{Q}{RT}\right). \qquad (2.14)$$

For modeling the deformation behavior of the present alloys it is necessary to determine the constants α, β, Q, n and A of Eq. (2.14). Taking the natural logarithm of Eq. (2.14) the following expression is obtained:

$$\ln\left[\sinh(\alpha\sigma)\right] = \frac{\ln\dot{\varepsilon}}{n} + \frac{Q}{nRT} - \frac{\ln A}{n}, \qquad (4.1)$$

The constants in Eq. (4.1) were determined by the procedure followed by researchers [19, 33, 34]. In the present work, the peak stress (σ_p) is substituted for the value of σ in Eq. (4.1). The stress multiplier α is the ratio of β/n_1 where, β is the average slope of ln($\dot{\varepsilon}$) versus σ_p plots and n_1 is the average slope of ln($\dot{\varepsilon}$) versus ln(σ_p) plots [19, 33, 34]. Figure 4.30 and Figure 4.31 shows the plots of ln($\dot{\varepsilon}$) versus σ_p and ln($\dot{\varepsilon}$) versus ln(σ_p) respectively. The values of α for all the alloys obtained from the plots are indicted in table 4.5.

The constant n is obtained by differentiating Eq (4.1) with respect to strain rate ($\dot{\varepsilon}$) at constant temperature (T) and is expressed as

$$n = \left.\frac{\partial \ln\dot{\varepsilon}}{\partial \ln\left[\sinh(\alpha\sigma)\right]}\right|_{T}. \qquad (4.2)$$

In the present study n value is determined as the average value of the slope of ln($\dot{\varepsilon}$) versus ln[sinh($\alpha\sigma_p$)] plots shown in Figure 4.32. The activation energy for deformation (Q) is determined by differentiating Eq. (4.1) with respect to temperature (T) at constant strain rate ($\dot{\varepsilon}$) resulting in the expression [19, 27, 66]

$$Q = nR\left[\frac{\partial \ln\{\sinh(\alpha\sigma)\}}{\partial\left(1/T\right)}\right]_{\dot{\varepsilon}} = \left[\frac{\partial \ln\dot{\varepsilon}}{\partial \ln\{\sinh(\alpha\sigma)\}}\right]_{T} R\left[\frac{\partial \ln\{\sinh(\alpha\sigma)\}}{\partial\left(1/T\right)}\right]_{\dot{\varepsilon}}, \qquad (4.3)$$

During deformation at a particular strain rate, the value of S is the slope of the line of the ln[sinh($\alpha\sigma$)] versus (1000/T) plot, where T is in K. The plots are shown in Figure

4.33. Activation energy *Q* is determined by multiplying the mean value of the slopes of these lines with *n*R.

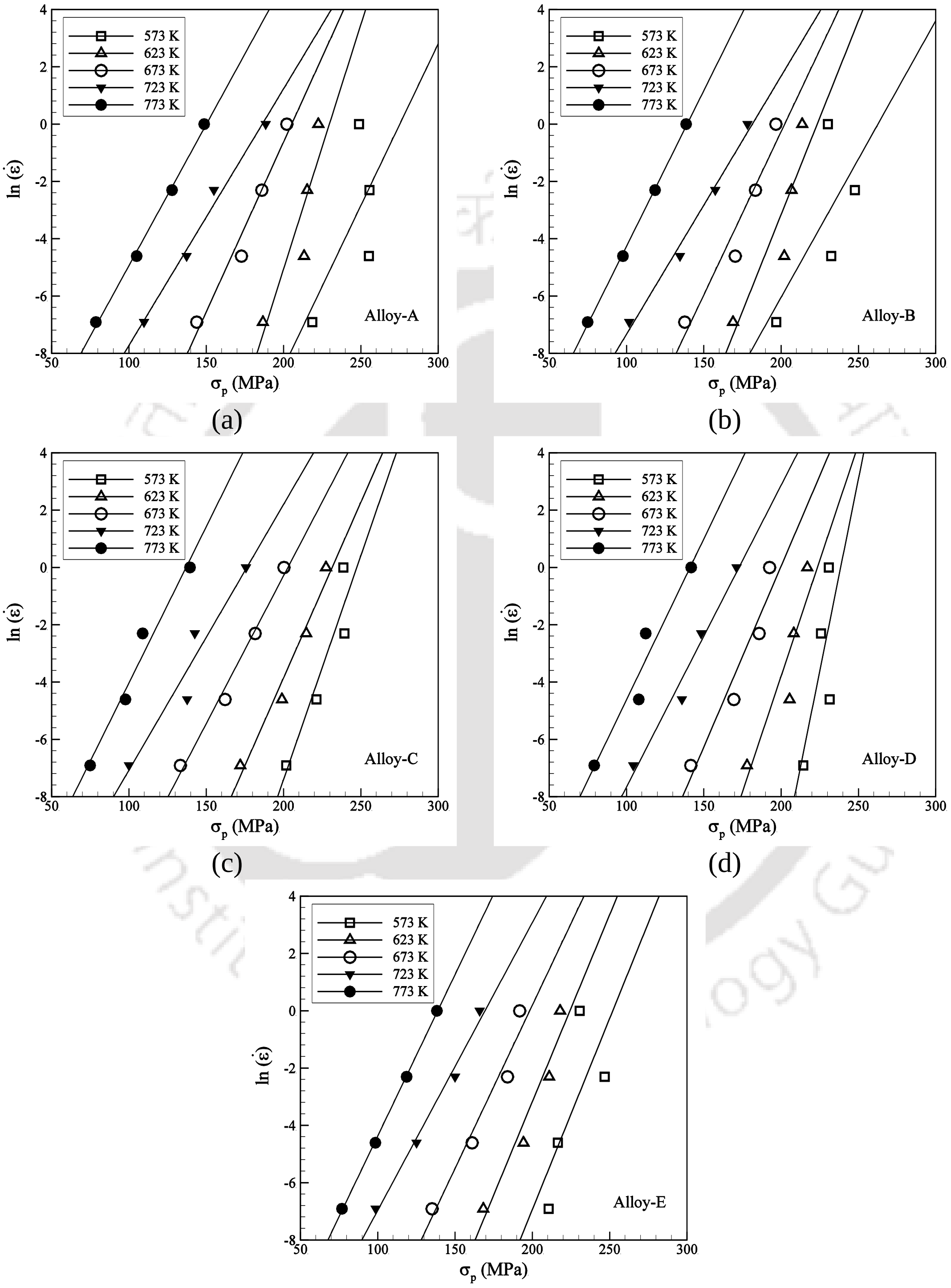

(a) (b) (c) (d) (e)

Figure 4.30 Plots ln($\dot{\varepsilon}$) versus peak flow stress, σ_p for (a) Alloy-A, (b) Alloy-B, (c) Alloy-C, (d) Alloy-D and (e) Alloy-E

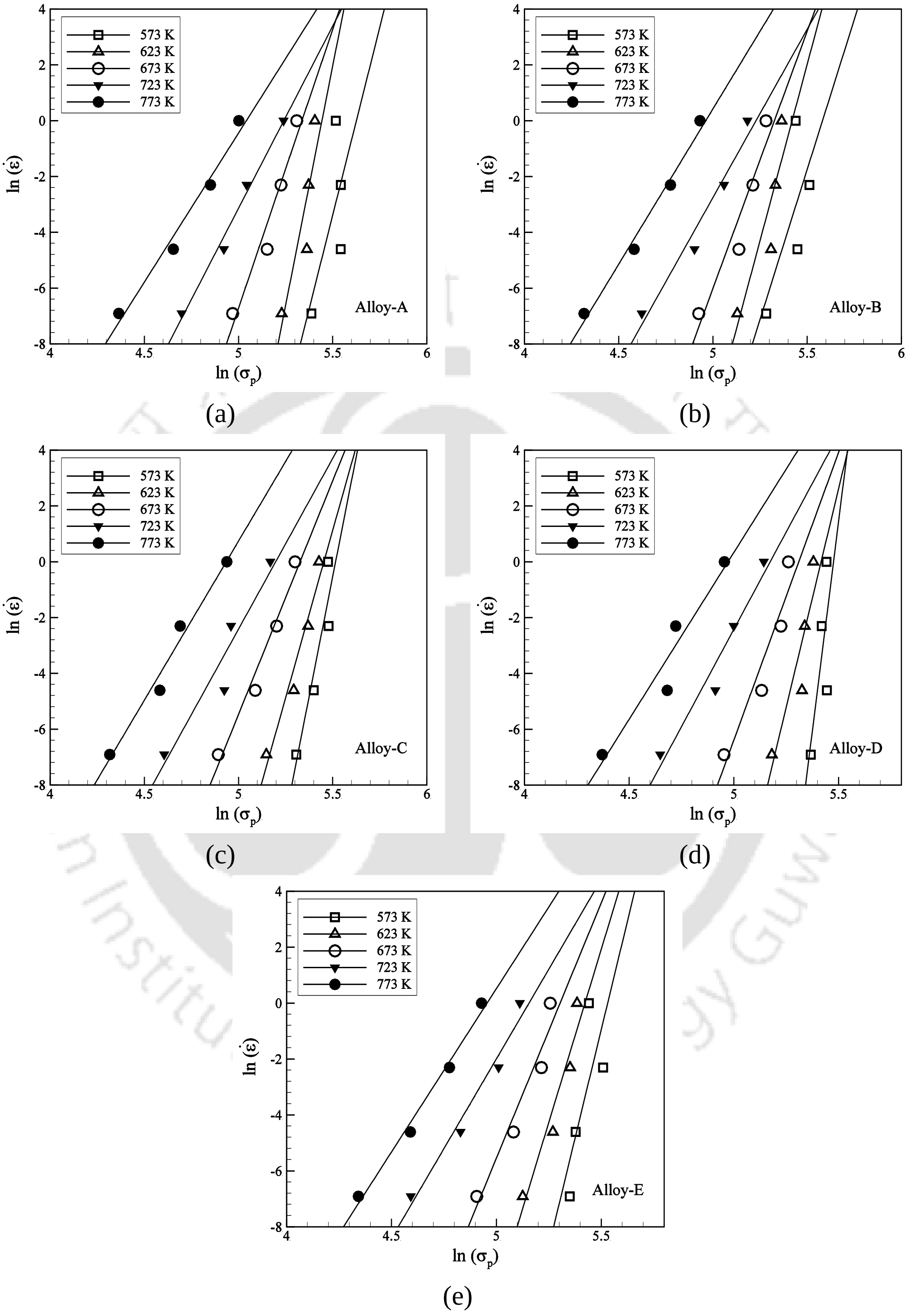

(a) (b) (c) (d) (e)

Figure 4.31 Plots of $\ln(\dot{\varepsilon})$ versus $\ln(\sigma_p)$ for (a) Alloy-A, (b) Alloy-B, (c) Alloy-C, (d) Alloy-D and (e) Alloy-E

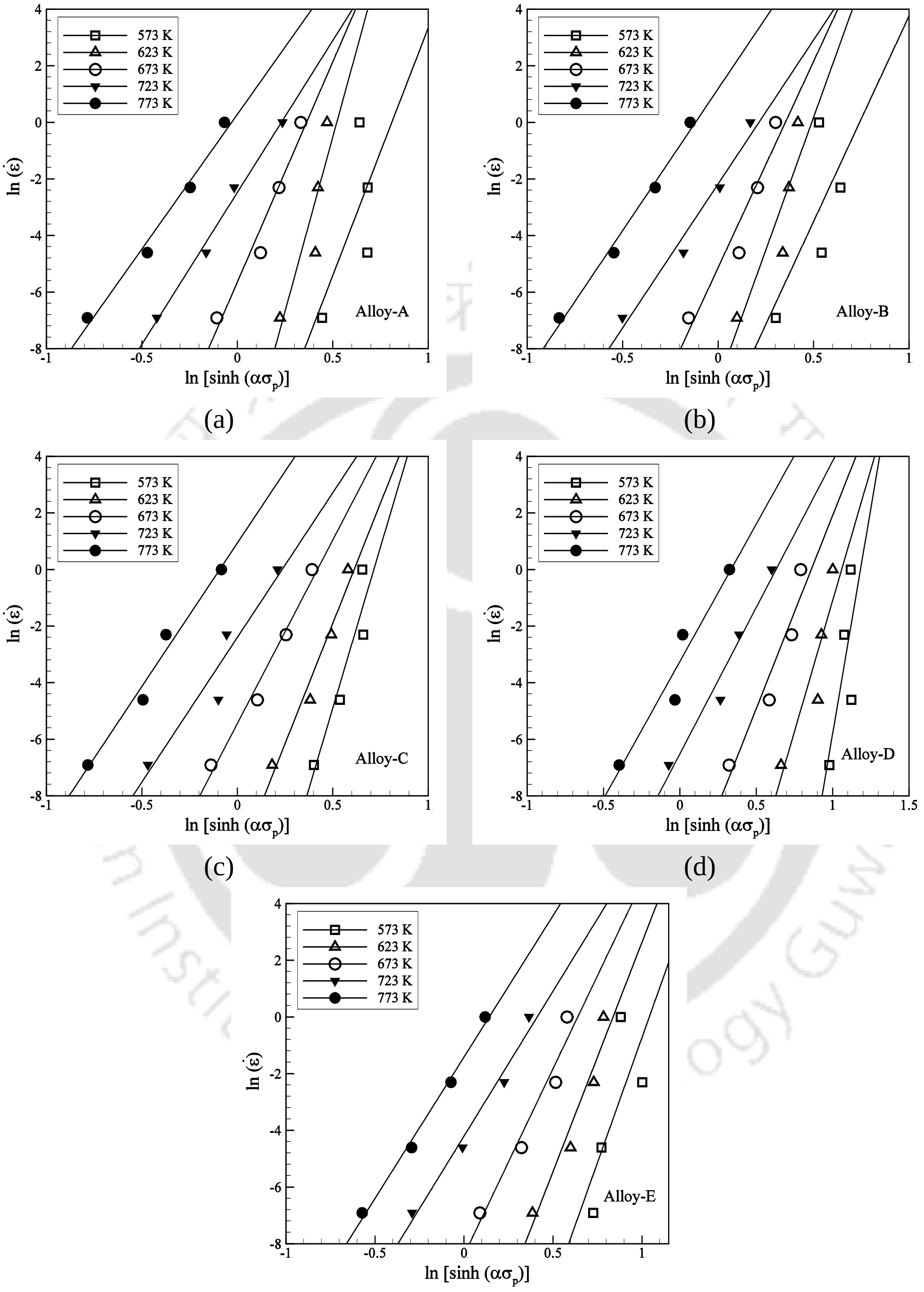

(a) (b) (c) (d) (e)

Figure 4.32 Plots of ln($\dot{\varepsilon}$) versus ln[sinh($\alpha\sigma_p$)] for (a) Alloy-A (b) Alloy-B (c) Alloy-C (d) Alloy-D and (e) Alloy-E

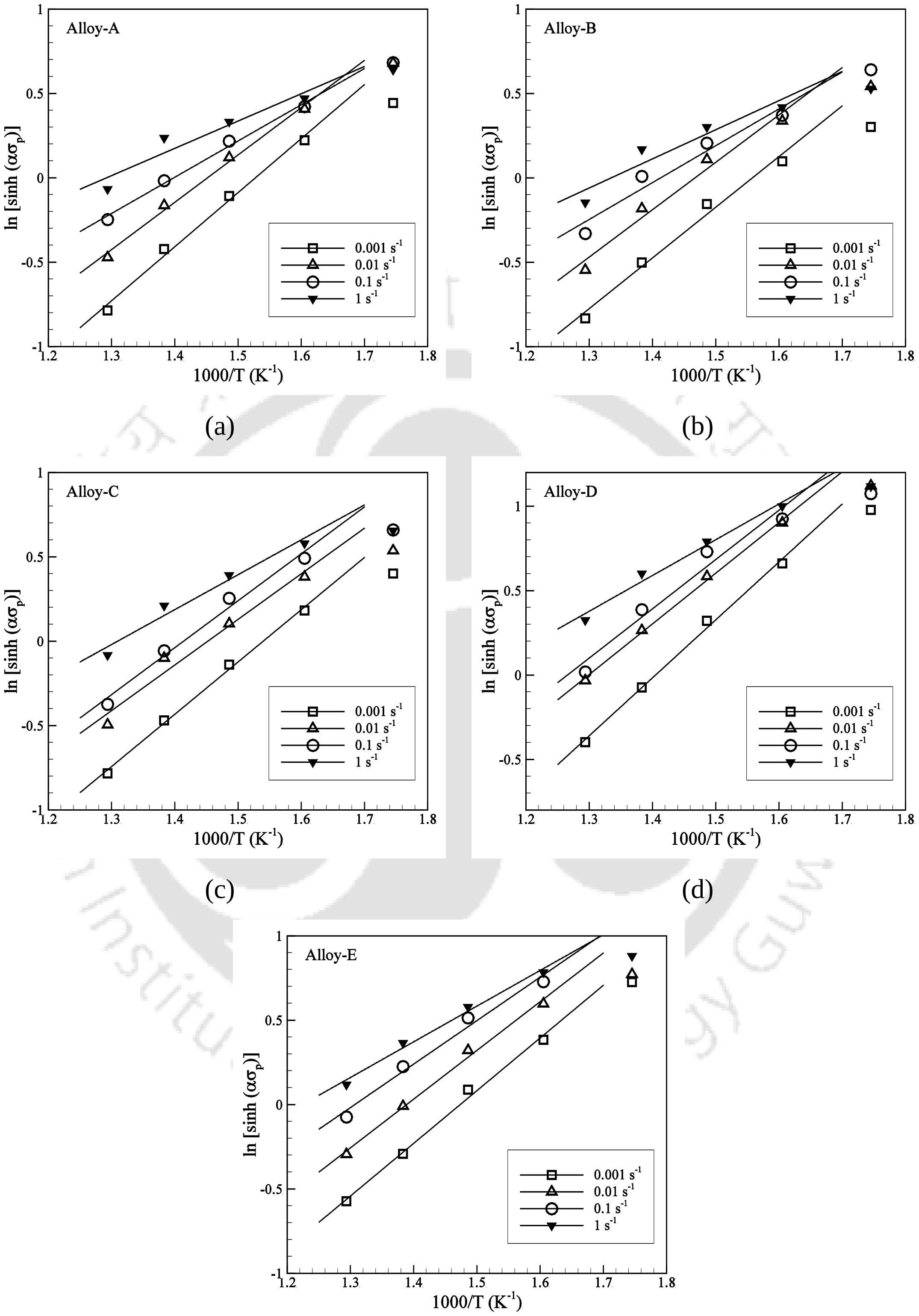

(a)

(b)

(c)

(d)

(e)

Figure 4.33 Plots of ln[sinh(ασ)] versus 1000/T for (a) Alloy-A, (b) Alloy-B, (c) Alloy-C, (d) Alloy-D and (e) Alloy-E

Zener-Hollomon parameter

Zener-Hollomon parameter (Z) expressed by Eq. (2.17) describes (*cf.* section 2.6.2) the variation of strain rate with deformation conditions [17].

$$Z = \dot{\varepsilon} \exp\left(Q/RT \right) = A\left[\sinh(\alpha\sigma)\right]^{n} \tag{2.17}$$

Taking the natural logarithm of both sides, Eq. (2.17) can be written in the form

$$\ln(Z) = \ln(A) + n\ln\left[\sinh(\alpha\sigma)\right] \tag{4.4}$$

where A and n can be obtained from the plots $\ln(Z)$ versus $\ln[\sinh(\alpha\sigma)]$. Figure 4.34 shows the $\ln(Z)$ versus $\ln[\sinh(\alpha\sigma)]$ plots, indicating a fairly good linear fit for all the alloys. As per Eq. (2.17), the Zener-Hollomon parameter (Z) increases with increase in flow stress. Since the flow stress increases with increase in strain rate and decrease in temperature, the trend in the variation of Zener-Hollomon parameter (Z) is similar to the variation of the peak flow stress (σ_p). Higher scatter in the graphs are seen for high strain rate ($\dot{\varepsilon}$ =10 s^{-1}) conditions. Good linear fit seen in the Figures 4.34, for strain rates below 0.1 s^{-1} are comparable to that reported by others [17, 21, 33].

Conventional strain rates employed for hot deformation processing of aluminum alloys are generally in the range 0.01–0.1 s^{-1}. Literature indicates that low Z values favors dynamic recrystallization which correspond to low strain rates and high deformation temperatures. The values of $\ln(Z)$ obtained for all alloys at various combinations of temperatures and strain rates are presented in Table 4.6 to Table 4.10. From the tables it is evident that the variation of Z value for each alloy shows the same trend as that of the peak flow stress. i.e increases with increase in strain rate and decrease in temperature. From the values of Z, the values of A are obtained using Eq. (4.4). Values of constitutive parameters n, A, α, S and Q determined for all alloys are shown in Table 4.5.

The constitutive equation for the peak flow stress for various combinations of strain rate and temperature can be obtained using the values of α, n, A and Q. The Q value obtained for Alloy-B, Alloy-C, Alloy-D and Alloy-E is lower compared to Alloy-A. This indicates that addition of silver in the alloy lowers the stress required for plastic deformation within the domain of temperature and strain rates investigated in the present study. The temperature and strain rate dependent peak flow stress (σ_p) for all alloys was evaluated using the constitute parameters of Eq. (4.5).

Table 4.5 The values of the material constants α, n, *S*, *Q* and *A*

Alloy Designation	α	*n*	*S*	*Q* (kJ/mol–*K*)	*A* (s^{-1})
Alloy-A	0.0056	15.59	2.18	282.6	7.21×10^{19}
Alloy-B	0.0056	13.61	2.29	259.1	2.93×10^{18}
Alloy-C	0.0059	14.62	2.18	265.9	4.78×10^{18}
Alloy-D	0.0079	13.06	2.42	262.7	1.17×10^{16}
Alloy-E	0.0069	13.43	2.32	259.0	9.75×10^{16}

Table 4.6 Values of ln (*Z*) for Alloy-A at various deformation conditions

$\dot{\varepsilon}$ (s^{-1})	*T* (K)				
	573	623	673	723	773
0.001	44.14	40.04	36.55	33.55	30.93
0.01	46.44	42.34	38.85	35.85	33.23
0.1	48.74	44.65	41.16	38.15	35.53
1.0	51.04	46.95	43.46	40.45	37.84
10	53.35	49.25	45.76	42.76	40.14

Table 4.7 Values of ln (*Z*) for Alloy-B at various deformation conditions

$\dot{\varepsilon}$ (s^{-1})	*T* (K)				
	573	623	673	723	773
0.001	54.15	49.25	45.08	41.48	38.35
0.01	56.46	51.55	47.38	43.79	40.66
0.1	58.76	53.86	49.68	46.09	42.96
1.0	61.06	56.16	51.99	48.39	45.26
10	63.36	58.46	54.29	50.69	47.56

Table 4.8 Values of ln (*Z*) for Alloy-C at various deformation conditions

$\dot{\varepsilon}$ (s^{-1})	*T* (K)				
	573	623	673	723	773
0.001	41.34	37.47	34.17	31.33	28.86
0.01	43.64	39.77	36.47	33.63	31.16
0.1	45.94	42.07	38.77	35.93	33.46
1.0	48.25	44.37	41.08	38.24	35.76
10	50.545	46.68	43.38	40.54	38.06

Table 4.9 Values of ln (*Z*) for Alloy-D at various deformation conditions

$\dot{\varepsilon}$ (s^{-1})	*T* (K)				
	573	623	673	723	773
0.001	50.58	45.97	42.04	38.66	35.71
0.01	52.86	48.27	44.34	40.96	38.01
0.1	55.19	50.57	46.64	43.26	40.31
1.0	57.49	52.88	48.95	45.56	42.61
10	59.79	55.18	51.25	47.87	44.91

Table 4.10 Values of ln (*Z*) for Alloy-E at various deformation conditions

$\dot{\varepsilon}$ (s^{-1})	*T* (K)				
	573	623	673	723	773
0.001	51.03	46.38	42.42	39.01	36.04
0.01	53.33	48.68	44.72	41.31	38.34
0.1	55.63	50.98	47.02	43.61	40.64
1.0	57.94	53.27	49.33	45.92	42.95
10	60.24	55.59	51.63	48.22	45.25

$$\sigma_p = \frac{1}{\alpha}\sinh^{-1}\left[\frac{\dot{\varepsilon}\exp\left(Q/RT\right)}{A}\right]^{\frac{1}{n}}. \tag{4.5}$$

Peak flow stress, σ_p obtained from the model was compared with the experimental values for validation of the constitutive equations. Figure 4.35 (a) to Figure 4.35 (e) shows the plots of experimental values of peak flow stress versus the peak flow stress determined by the constitutive equations. The line inclined at 45° to the horizontal shown in figures indicates a line of perfect prediction whereas the two dashed line represents the boundaries of ±12.5% deviation values. Most of the points lie very close to the line of perfect prediction.

It is evident from Figure 4.35 (a) that 3 out of the 25 data points for Alloy-A falls outside the ±12.5% deviation line. i.e 88% of the σ_p values could be predicted within an accuracy of ±12.5% deviation. Most of the point outside the dashed line corresponds to the deformations carried out at very high strain rate (10 s^{-1}) or highest test temperature (500 °C). For any function fitting technique, few error is expected if the data used for the validation lie at the boundaries of the input domains. The data with high errors lie on the boundary of the input domains i.e. high strain rate or high

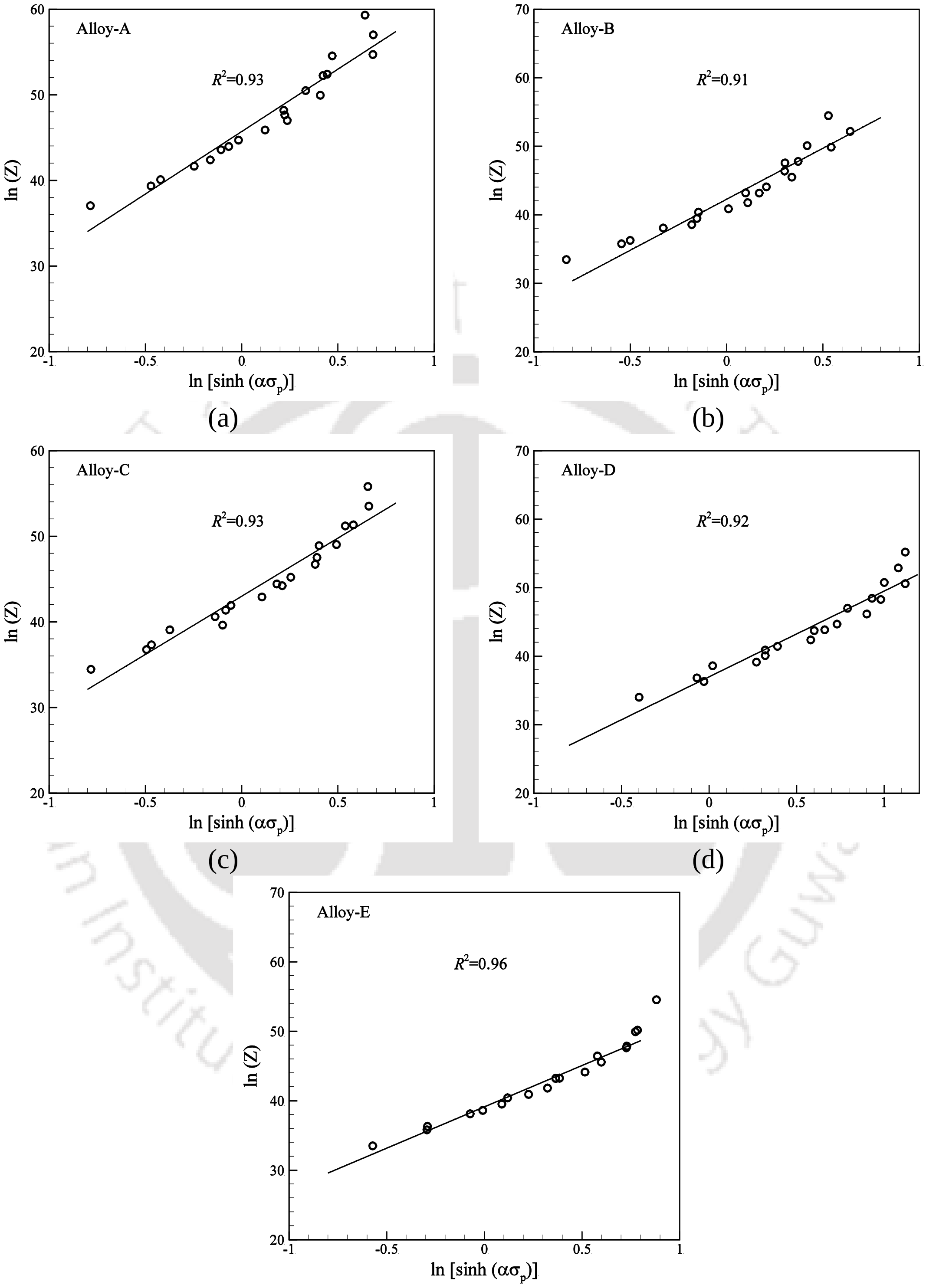

(a) (b) (c) (d) (e)

Figure 4.34 Plots of ln(Z) versus ln[sinh($\alpha\sigma_p$)] of (a) Alloy-A, (b) Alloy-B, (c) Alloy-C, (d) Alloy-D and (e) Alloy-E temperature. Figure 4.35(b), 4.35(c), 4.35(d) and 4.35(e) indicates that 88%, 92%,96% and 96% of peak flow stress values could be predicted within ±12.5% deviation for Alloy-B, Alloy-C, Alloy-D and Alloy-E, respectively. The present models providing maximum ±12.5% error in about 88% cases establishes the confidence in the predictive capabilities using the proposed constitutive equations.

4.4 Prediction of flow stress by artificial neural network modeling

Artificial neural network (ANN) modeling was carried out to obtain better prediction of flow stress (σ) of the investigated alloys during the isothermal deformation. This was based on the concept that

$$\sigma = \sigma\,(\varepsilon,\ \dot{\varepsilon},\ T)\ . \qquad (2.15)$$

After a number of trials using the training and testing data-sets, as per the procedure mentioned in section 3.5.2, the best neural network architecture was frozen for which (i) functional RMS error was minimum, (ii) minimum number of data sets has deviation error ≤ ±5%, (iii) maximum deviation during testing and training is within ±10%, and (iv) minimum variation in RMS functional error during training and testing. Table 4.11 shows the details of the artificial neural network (ANN) architecture for all the investigated alloys. The values of experimental flow stress, predicted flow stress by artificial neural network (ANN) and the calculated errors during the training and testing for all the alloys are shown in Appendix I to Appendix X.

Once the network was frozen, it was required to establish the confidence in the network architecture for the prediction of σ. Therefore, the trained network was used for prediction of flow stress (σ) using the 24 validation data sets. Table 4.12 gives the values of maximum absolute error, maximum percentage error and RMS error calculated for all alloys during training, testing and validation stages separately. Table 4.13 to Table 4.17 give the detailed experimental and predicted flow stress (σ) values along with the associated errors, for all alloys, during the validation of the artificial neural network (ANN) technique.

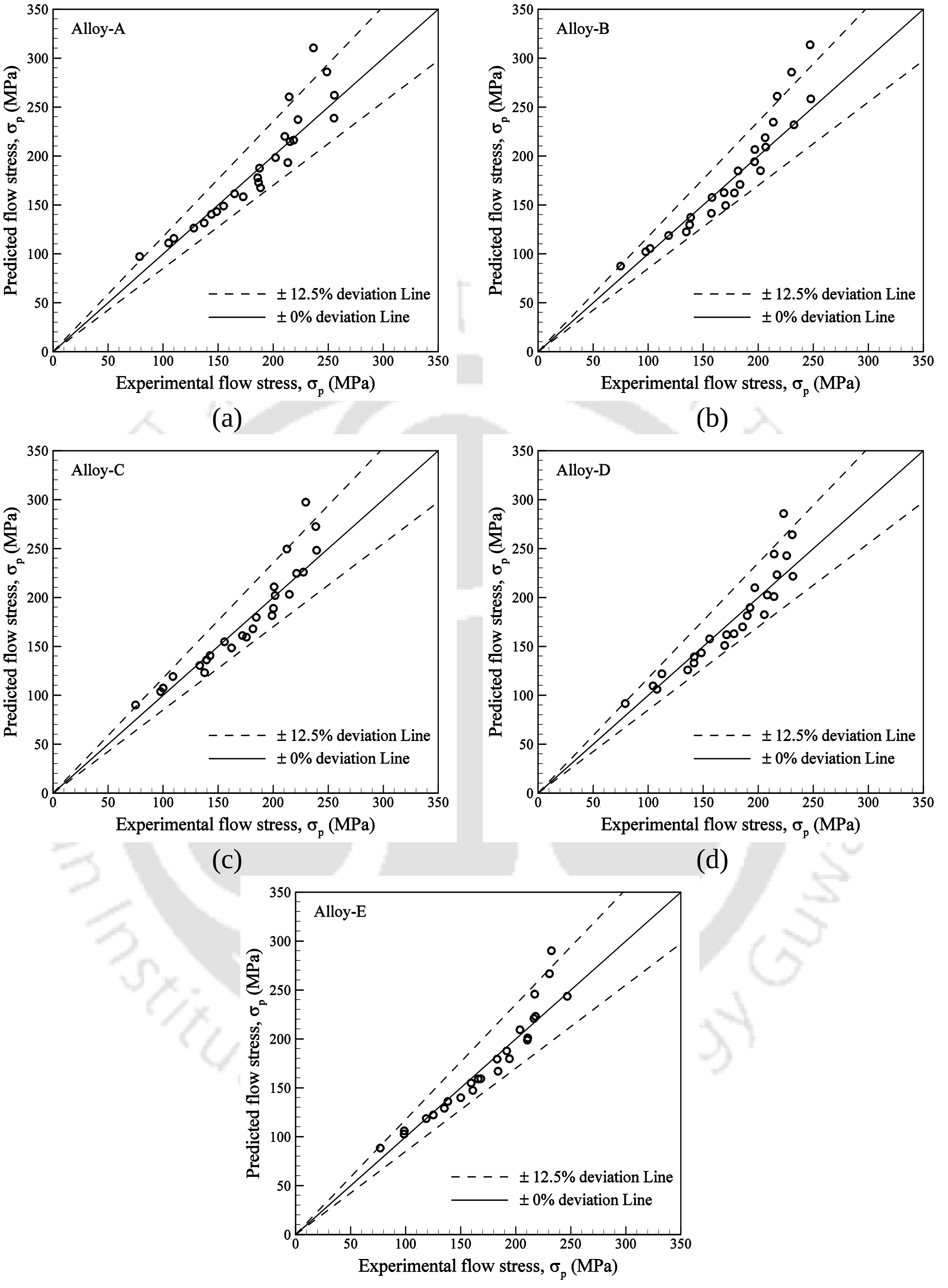

(a) (b) (c) (d) (e)

Figure 4.35 Plot of predicted flow stress versus experimental flow stress for (a) Alloy-A, (b) Alloy-B, (c) Alloy-C, (d) Alloy-D and (e) Alloy-E

Table 4.11 Best fit network architectures for the investigated alloys.

Sample ID	Hidden neurons	1st transfer function	2nd transfer function
Alloy-*A*	5	*logsig*	*purelin*
Alloy-*B*	7	*logsig*	*purelin*
Alloy-*C*	6	*tansig*	*purelin*
Alloy-*D*	7	*tansig*	*purelin*
Alloy-*E*	6	*logsig*	*purelin*

Table 4.12 Maximum absolute error, maximum percentage error and RMS error obtained for the alloys during training, testing and validation

	Training			Testing			Validation		
Alloy ID	Max. Error (MPa)	Max. % Error	RMS Error (MPa)	Max. Error (MPa)	Max. % Error	RMS Error (MPa)	Max. Error (MPa)	Max. % Error	RMS Error (MPa)
Alloy-A	9.57	4.53	2.92	11.73	5.04	3.92	10.17	5.68	5.34
Alloy-B	9.04	5.08	3.79	–10.02	6.68	3.18	–13.94	7.46	4.70
Alloy-C	9.20	5.24	4.08	8.59	5.80	2.89	–7.53	4.95	4.96
Alloy-D	–7.35	3.65	2.57	8.73	8.19	6.4	–10.63	5.95	5.74
Alloy-E	–5.75	3.82	2.65	–13.37	6.29	5.78	–8.42	5.11	4.40

Table 4.13 Comparison of experimental and predicted values of flow stress (σ) during validation for Alloy-A

Sl No.	Experimental flow stress (MPa)	Predicted flow stress (MPa)	Error (MPa)	Error (%)
1	159.7	161.0	–1.3	0.81
2	179.2	189.4	–10.2	5.69
3	150.9	158.4	–7.5	4.97
4	187.2	188.2	–1.0	0.53
5	168.1	170.1	–2.0	1.19
6	201.9	206.9	–5.0	2.48
7	154.6	163.8	–9.2	5.95
8	200.3	200.8	–0.5	0.25
9	171.3	171.0	0.3	0.18
10	208.6	213.8	–5.2	2.49

11	153.7	163.5	–9.8	6.38
12	201.8	204.0	–2.2	1.09
13	172.1	168.8	3.3	1.92
14	211.8	214.8	–3.0	1.42
15	152.2	161.3	–9.1	5.98
16	200.7	203.8	–3.1	1.54
17	169.6	165.8	3.8	2.24
18	213.7	214.2	–0.5	0.23
19	150.8	158.4	–7.6	5.04
20	199.4	202.7	–3.3	1.65
21	169.4	162.3	7.1	4.19
22	214.8	213.1	1.7	0.79
23	149.7	154.8	–5.1	3.41
24	198.5	201.0	–2.5	1.26

Table 4.14 Comparison of experimental and predicted values of flow stress (σ) during validation for Alloy-B

Sl No.	Experimental flow stress (MPa)	Predicted flow stress (MPa)	Error (MPa)	Error (%)
1	164.0	162.6	1.4	0.85
2	186.8	200.7	–13.9	7.44
3	152.5	151.9	0.6	0.39
4	186.6	186.1	0.5	0.27
5	168.8	167.2	1.6	0.95
6	203.5	208.2	–4.7	2.31
7	156.7	152.8	3.9	2.49
8	196.3	193.3	3.0	1.53
9	169.1	167.5	1.6	0.95
10	206.4	210.5	–4.1	1.99
11	154.7	150.6	4.1	2.65
12	194.8	194.9	–0.1	0.05
13	168.4	165.7	2.7	1.60
14	206.2	210.6	–4.4	2.13
15	152.4	148.9	3.5	2.30
16	191.1	191.3	–0.2	0.10
17	165.0	162.0	3.0	1.82
18	206.0	211.3	–5.3	2.57
19	150.7	148.2	2.5	1.66
20	187.5	188.5	–1.0	0.53
21	165.4	156.1	9.3	5.62
22	205.7	213.6	–7.9	3.84
23	148.9	146.3	2.6	1.75
24	185.8	189.4	–3.6	1.94

Table 4.15 Comparison of experimental and predicted values of flow stress (σ) during validation for Alloy-C

Sl No.	Experimental flow stress (MPa)	Predicted flow stress (MPa)	Error (MPa)	Error (%)
1	155.9	159.0	–3.1	1.99
2	189.5	196.7	–7.2	3.80
3	138.1	142.9	–4.8	3.48
4	188.2	183.6	4.6	2.44
5	160.8	166.2	–5.4	3.36
6	207.7	210.8	–3.1	1.49
7	142.1	146.5	–4.4	3.10
8	199.6	192.9	6.7	3.36
9	160.2	167.4	–7.2	4.49
10	211.3	216.8	–5.5	2.60
11	139.9	146.1	–6.2	4.43
12	199.4	195.5	3.9	1.96
13	159.3	165.8	–6.5	4.08
14	212.6	217.6	–5.0	2.35
15	137.4	144.2	–6.8	4.95
16	196.7	195.0	1.7	0.86
17	155.7	163.2	–7.5	4.82
18	213.5	216.6	–3.1	1.45
19	136.8	141.9	–5.1	3.73
20	193.9	193.6	0.3	0.15
21	155.6	160.4	–4.8	3.08
22	214.3	215.0	–0.7	0.33
23	135.9	139.5	–3.6	2.65
24	191.6	191.7	–0.1	0.05

Table 4.16 Comparison of experimental and predicted values of flow stress (σ) during validation for Alloy-D

Sl No.	Experimental flow stress (MPa)	Predicted flow stress (MPa)	Error (MPa)	Error (%)
1	158.6	162.6	–4.0	2.52
2	178.4	189.0	–10.6	5.94
3	139.2	147.6	–8.4	6.03
4	179.6	180.5	–0.9	0.50
5	166.5	172.4	–5.9	3.54
6	198.5	204.4	–5.9	2.97
7	147.8	152.3	–4.5	3.04
8	191.6	194.2	–2.6	1.36
9	168.6	174.7	–6.1	3.62

10	202.7	208.0	–5.3	2.61
11	146.6	152.0	–5.4	3.68
12	192.1	195.5	–3.4	1.77
13	168.9	174.5	–5.6	3.32
14	204.1	209.7	–5.6	2.74
15	144.7	151.0	–6.3	4.35
16	190.2	194.2	–4.0	2.10
17	166.0	173.3	–7.3	4.40
18	206.1	211.5	–5.4	2.62
19	143.8	149.1	–5.3	3.69
20	188.6	194.0	–5.4	2.86
21	166.0	171.7	–5.7	3.43
22	207.3	213.8	–6.5	3.14
23	142.8	146.7	–3.9	2.73
24	187.7	194.2	–6.5	3.46

Table 4.17 Comparison of experimental and predicted values of flow stress (σ) during validation for Alloy-E

Sl No.	Experimental flow stress (MPa)	Predicted flow stress (MPa)	Error (MPa)	Error (%)
1	152.2	153.7	–1.5	0.99
2	188.0	192.6	–4.6	2.45
3	143.7	145.4	–1.7	1.18
4	182.4	179.9	2.5	1.37
5	159.2	157.1	2.1	1.32
6	205.9	207.8	–1.9	0.92
7	149.5	146.9	2.6	1.74
8	191.5	190.1	1.4	0.73
9	159.9	155.0	4.9	3.06
10	208.6	214.8	–6.2	2.97
11	148.2	146.5	1.7	1.15
12	189.6	191.2	–1.6	0.84
13	160.5	152.3	8.2	5.11
14	208.9	217.3	–8.4	4.02
15	145.7	145.6	0.1	0.07
16	185.6	189.2	–3.6	1.94
17	157.2	150.7	6.5	4.13
18	209.5	217.0	–7.5	3.58
19	143.9	143.4	0.5	0.35
20	182.3	186.3	–4.0	2.19
21	156.9	150.0	6.9	4.40
22	210.2	214.4	–4.2	2.00
23	142.4	139.7	2.7	1.90
24	180.1	183.2	–3.1	1.72

Plots of experimental flow stress versus predicted flow stress value for all alloys during training, testing and validation has been shown in Figures 4.36, 4.37 and 4.38, respectively. Dashed lines representing the boundaries of ±5% deviations are also shown in the figures. Figures reveal that most of the points lie very close to the line of prefect prediction. During validation, it was observed that 19, 22, 24, 22 and 23 out of 24 data points fall within ± 5% deviation line for Alloy-A, Alloy-B, Alloy-C, Alloy-D and Alloy-E, respectively. Though the percentage errors in prediction were comparatively high for the few data with deviations above ±5%, their absolute errors were low, especially in the cases of low flow stresses.

The observation that 5, 2, 0, 2 and 1 out of 24 data points fall outside ± 5% deviation line respectively for Alloy-A, Alloy-B, Alloy-C, Alloy-D and Alloy-E, respectively indicates very good prediction of flow stress by artificial neural network (ANN) modeling. This observation together with the low RMS error highlight the superior prediction capability of this technique.

Simulation of Flow curve by artificial neural network (ANN) technique

After establishing the confidence in the prediction capability by artificial neural network (ANN), it was decided to predict the flow curve for a particular combination of strain rate and temperature. For this purpose experimental data at 400 °C under all strain rates were not considered for the network training and testing of each alloy. These data were used only for the validation purpose. This was to authenticate the flow curve prediction capability of artificial neural network (ANN) for unknown conditions. The input–output data sets obtained from the remaining 20 experiments (i.e. combinations of T = 300 °C, 350 °C, 450 °C and 500 °C at strain rates of 0.001 s^{-1}, 0.01 s^{-1}, 0.1 s^{-1}, 1.0 s^{-1} and 10 s^{-1}) of each alloy were extracted from the experimental flow curves. New artificial neural network (ANN) architecture was developed for this purpose by a number of simulation trials using the method discussed in the previous section. The flow curves for each alloy at 400 °C was predicted for all the 5 strain rates and compared with the experimental values. The statistical parameter, i.e. the coefficient of determination (R^2) value, was determined for each flow curve as per the following equations mentioned in Chapter 3.5.2.

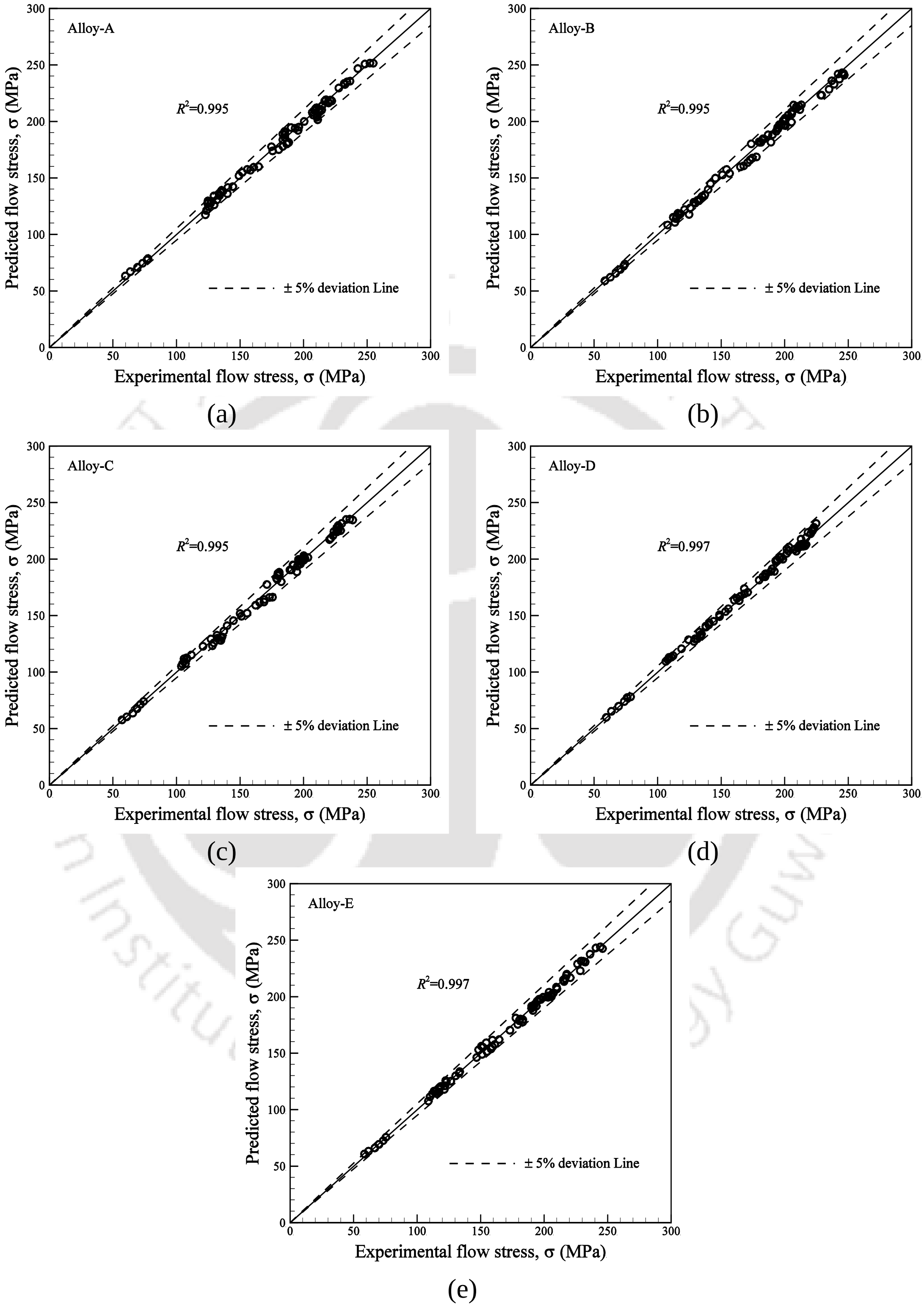

Figure 4.36 Plot showing predicted flow stress versus experimental flow stress during training

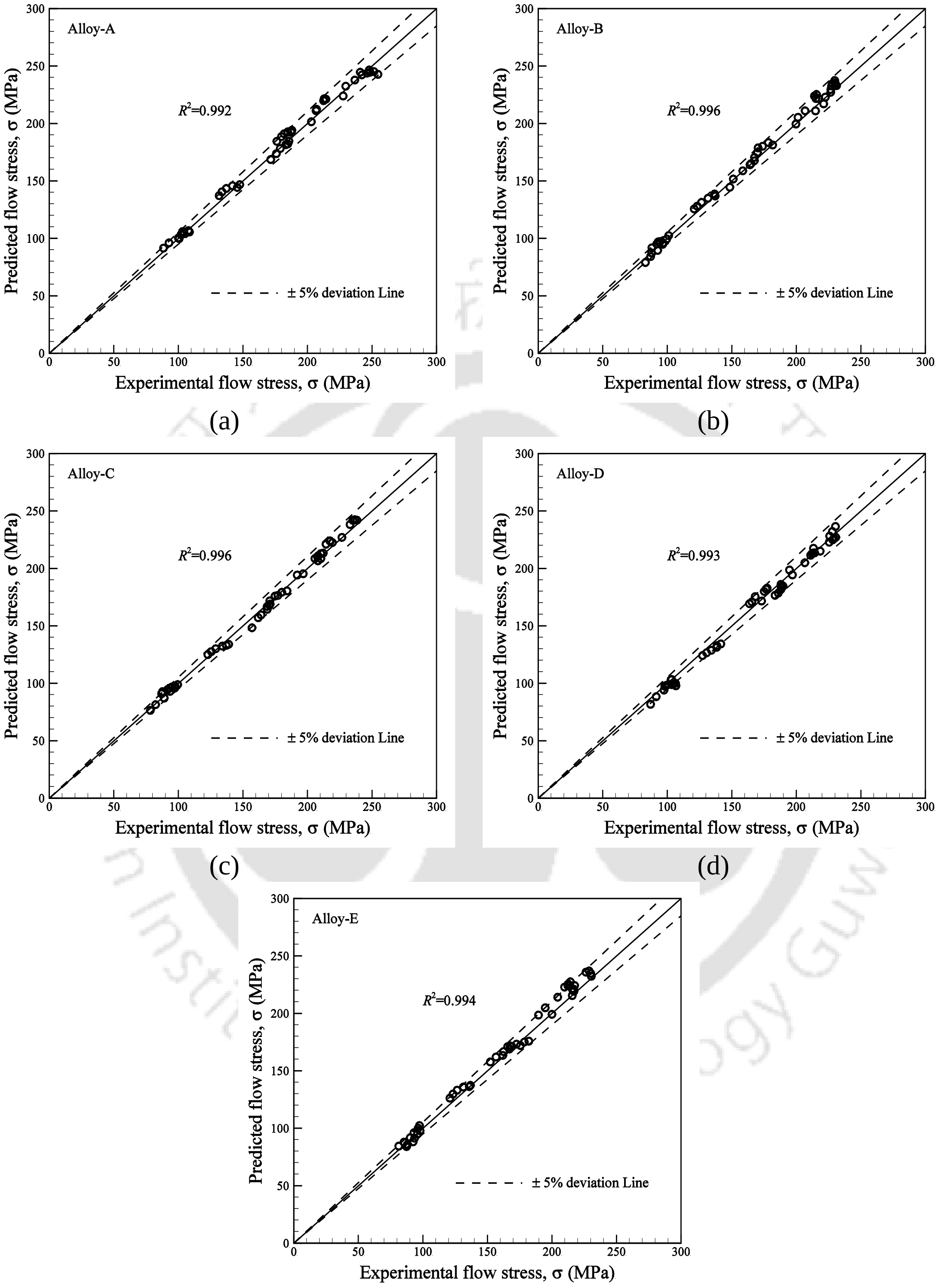

(a) (b)

(c) (d)

(e)

Figure 4.37 Plot showing predicted flow stress versus experimental flow stress during testing

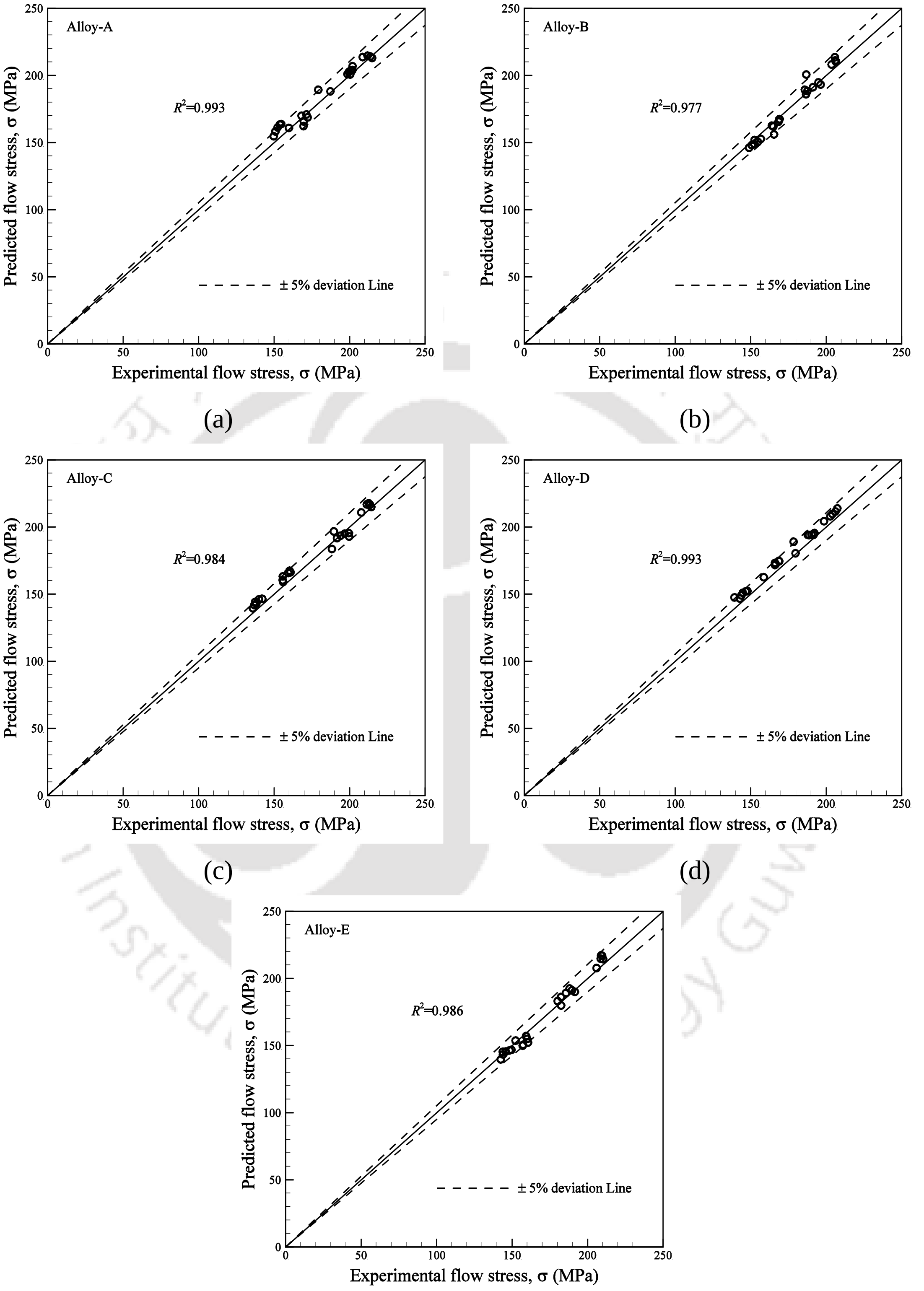

(a)

(b)

(c)

(d)

(e)

Figure 4.38 Plot showing predicted flow stress versus experimental flow stress during validation

$$\begin{aligned} R^2 &= 1 - \frac{SS_{residual}}{SS_{total}} \\ SS_{residual} &= \sum_{i=1}^{n} (E_i - P_i)^2 \\ SS_{total} &= (n-1) \times \sigma^2 \\ \sigma^2 &= \frac{\sum_{i=1}^{n} (E_i - \bar{E})^2}{n} \end{aligned} \tag{3.5}$$

Simulation was carried out for strains up to 0.6 at 400°C and compared with the values obtained from the hot compression tests at the same temperature and strain rates. Figure 4.39 shows the comparison of the simulated flow stress values with the experimental values for Alloy-A and Alloy-E, respectively. The coefficient of determination (R^2) during the prediction of flow curve for all alloys under different strain rates are found to lie between 0.97–0.99. The maximum deviation error during the simulation was 4.3%, 6.1% and 5.3% for strain rates of 0.001 s^{-1}, 0.01 s^{-1} and 0.1 s^{-1} for alloy-A. For alloy-E maximum deviation error is 6.0%, 6.6% and 6.3% for strain rates of 0.001 s^{-1}, 0.01 s^{-1} and 0.1 s^{-1} respectively. The percentage deviation error and the R^2 values during simulation indicate good prediction capability of artificial neural network (ANN) technique for flow cure simulation.

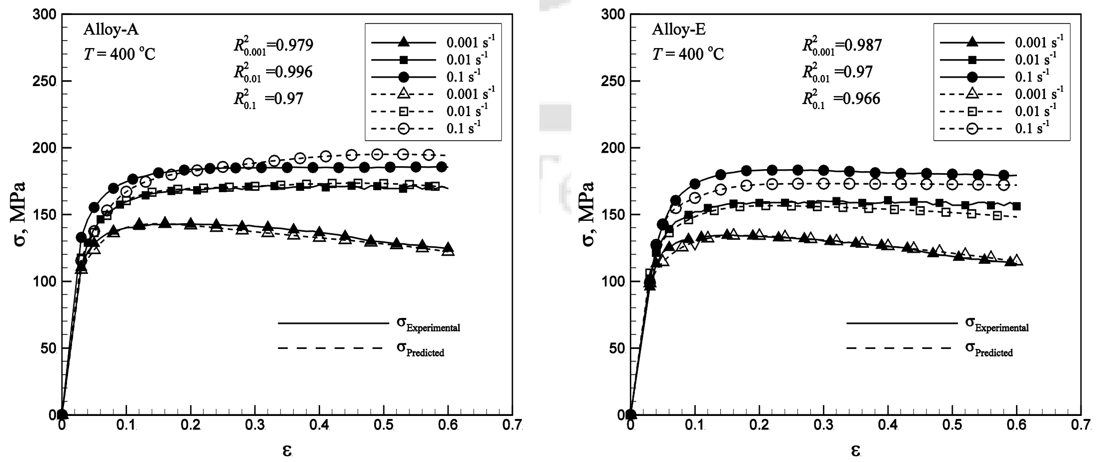

(a) (b)

Figure 4.39 Comparison of simulated flow stress values with the experimental values for (a) Alloy-A and (b) Alloy-E

4.5 Generation of processing maps for hot workability

Results of the artificial neural network (ANN) modeling for flow stress (σ) in the process domain (i.e. $\varepsilon, \dot{\varepsilon}$ and T) of experimental investigation show high value of coefficient of determination ($0.97 < R^2 < 0.99$). This indicates very good prediction capability. Flow stresses were simulated at small temperature intervals ($\Delta T = 10$ °C) and strain rates ($\log(\Delta\dot{\varepsilon}) = 0.1$) for the entire experimental process domain of temperature and strain rates. These data were used to generate processing maps, which would demarcate the process domains for safe hot working of the alloys. Generation of the processing maps is of considerable importance for industrial processing of these alloys.

Workability is an important parameter in mechanical working of materials which is dependent on the inherent flow characteristics of the material and the externally controllable variables like deformation temperature (T), strain rate ($\dot{\varepsilon}$), and strain (ε). The processing map is obtained by the superimposition of instability map on the power dissipation efficiency map and is explained in detail in section 2.8 and section 3.5.3. The results obtained and the discussions are as follows.

From the predicted flow stress values the value of strain rate sensitivity (m) was determined using equation 2.21 for different combination of strain rate and temperatures over the entire domain of experiments. The efficiency of power dissipation (η) and instability regime [101] was thus determined.

The contour plot of strain rate sensitivity (m) value obtained for Alloy-A at a strain of 0.1 is shown in Figure 4.40 (a). The figure reveal the following: (i) the strain rate sensitivity (m) value increases with increase in temperature (T) and decrease in strain rate ($\dot{\varepsilon}$); (ii) maximum strain rate sensitivity (m) value is 0.16 which is observed at strain rate = 0.001 s^{-1} and temperature > 450 ºC and (iii) strain rate sensitivity (m) value is negative for strain rate > 0.025 s^{-1} and temperature < ~330 ºC.

Contour plots of efficiency of power dissipation (η) for Alloy-A obtained at a strain of 0.1 is shown in Figure 4.40 (b). The observations are: (i) value of efficiency of power dissipation (η) increases with increase in temperature and decrease in strain rate; (ii) maximum value of efficiency of power dissipation (η) is 38% and is observed at strain rate = 0.001 s^{-1} and temperature > 480 ºC and (iii) contour plots are widely spaced when efficiency of power dissipation, η > 15% for which strain rate sensitivity m > 0.05. From these observations, it is evident that the efficiency of power dissipation, η is higher for regimes having higher strain rate sensitivity, m values.

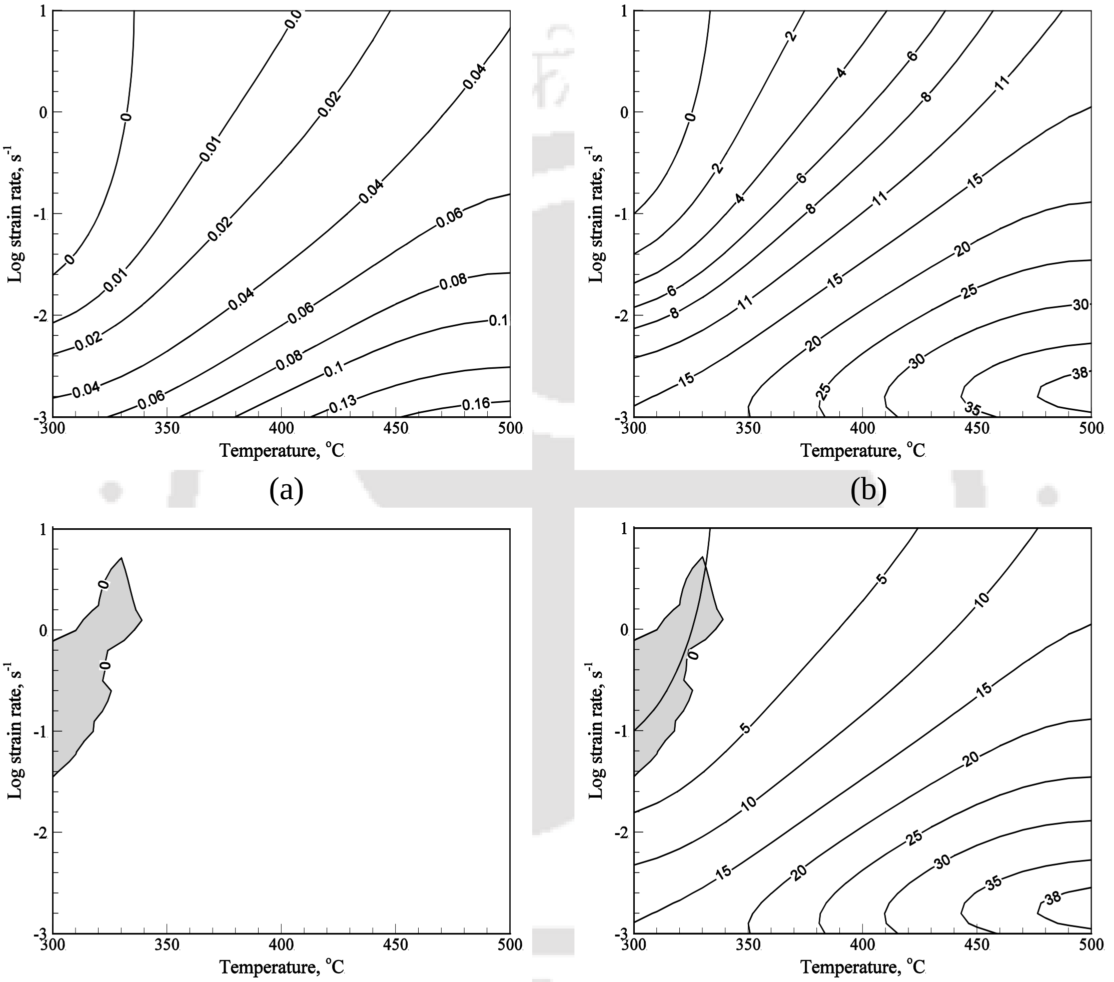

(a) (b)

(c) (d)

Figure 4.40 (a) Contour plot of strain rate sensitivity (m), (b) contour plot of efficiency of power dissipation (η), (c) instability regime and (d) deformation processing map for Alloy A at a strain of 0.1

The instability regime for Alloy-A at a strain of 0.1 is shown by the shaded area in Figure 4.40 (c). The processing map, obtained by superimposing instability map on the efficiency of power dissipation map, has been shown in Figure 4.40 (d). The region of instability is found to be at temperature < 340 ºC and 0.04 s^{-1} >strain rate < ~0.8 s^{-1}.

The contour plots of strain rate sensitivity, *m* values and processing maps for Alloy-A at strains of 0.2, 0.4 and 0.6 are depicted in Figure 4.41. From the figure it is evident that efficiency of power dissipation (η) increases with increase in strain. As the strain is increased, the instability region gradually spreads towards the region of higher temperatures and strain rates. The *m* value and efficiency of power dissipation (η) increases with increase in strain at all process conditions (i.e. combination of temperatures and strain rates). At strain value of 0.6, the regime of instability is identified to be at temperatures < 380 °C and strain rate > 0.1 s^{-1}.

The contour plots for the strain rate sensitivity (*m*) values for the remaining alloys deformed to a strain of 0.6 are shown in Figure 4.42 (a) to (d). The strain rate sensitivity (*m*) value for all alloys is highest at regimes of high temperature and low strain rates. The maximum strain rate sensitivity (*m*) value decreases continuously from 0.25 for the alloy with 0 wt.% silver to 0.14 for the alloy with 0.1 wt.% silver, at a strain value of 0.6.

The processing maps for Alloy-B, Alloy-C, Alloy-D and Alloy-E at strain of 0.6 are shown in Figure 4.43 (a) to Figure 4.43(d), respectively. It is evident that the efficiency of power dissipation (η) decreases with increase in silver content in the alloy. As silver content increases from 0 wt.% to 0.1 wt.%, efficiency of power dissipation (η) value decreases continuously from 54% to 34%. With increase in silver content, the unstable region increases and spreads towards the region of higher temperatures. Instability regime for the alloy containing 0.03 wt.% silver (Alloy-B), after a strain of 0.6, is observed to be at strain rate > 0.125 s^{-1} and temperatures in the range 300–380 °C. For alloy with 0.1 wt.% silver (Alloy-E), instability regime is at strain rate > 0.125 s^{-1} and temperatures 300–480 °C.

The stable flow regime (safe process regime) for Alloy-E at a strain value of 0.6 is found for the low strain rate regions (i.e. $\dot{\varepsilon} < 0.125\ s^{-1}$) for the entire range of investigated temperatures. Maximum values of strain rate sensitivity (*m*), efficiency of power dissipation (η) and regimes of stable flow for alloys are shown in Table 4.18.

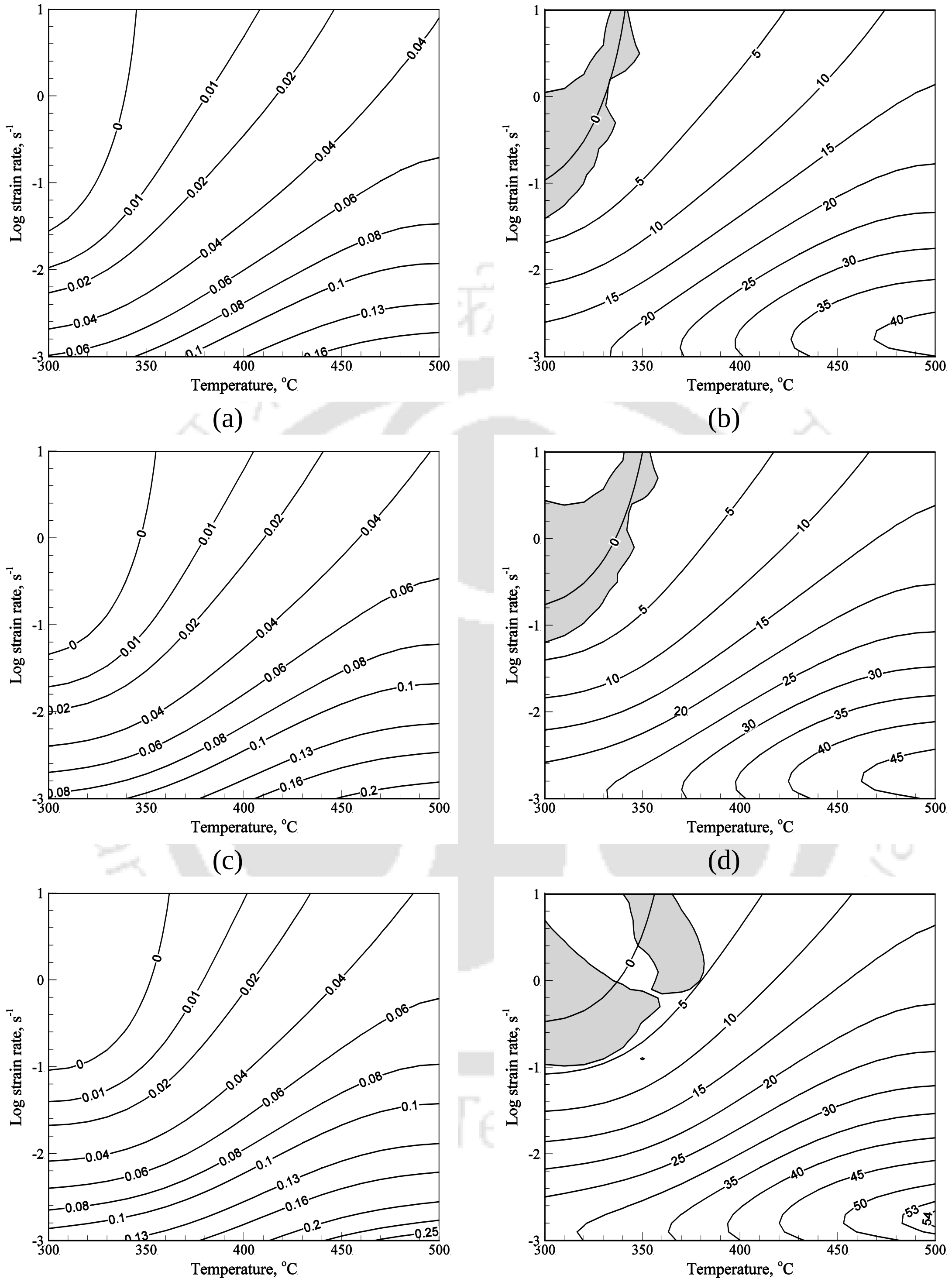

(a) (b)

(c) (d)

(e) (f)

Figure 4.41 Contour plots of strain rate sensitivity (*m*) value and processing map for Alloy-A, respectively, at strains (a) & (b) 0.2, (c) & (d) 0.4 and (e) & (f) 0.6

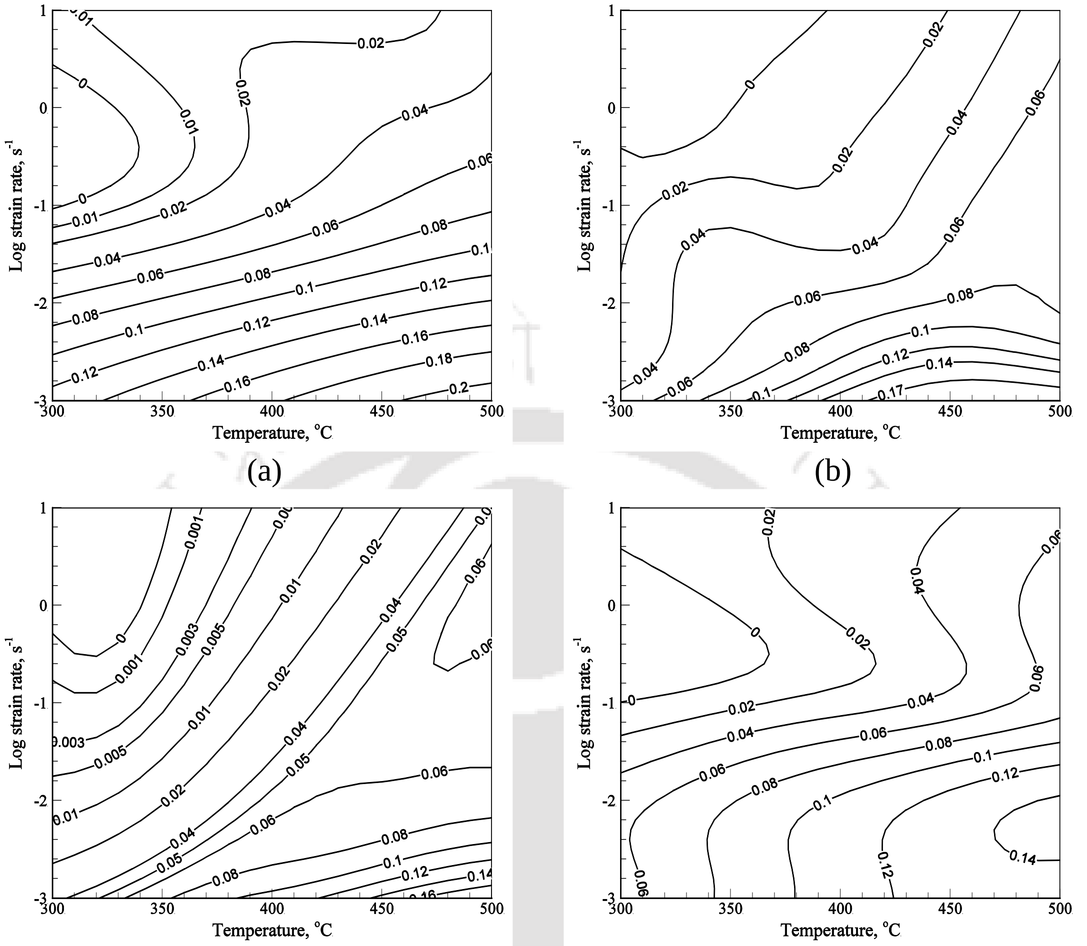

(a) (b)

(c) (d)

Figure 4.42 Contour plots of strain rate sensitivity (m) at strain 0.6 for (a) Alloy-B, (b) Alloy-C, (c) Alloy-D and (d) Alloy-E

Table 4.18 Process parameters for maximum power dissipation efficiency values of the alloys

Sample ID	Maximum strain rate sensitivity factor (m)	Strain-rate ranges (s^{-1})	Temperature ranges (°C)	Maximum power dissipation efficiency, η (%)
Alloy-A	0.25	0.001–0.01	470–500	54
Alloy-B	0.20	0.001–0.01	450–450	45
Alloy-C	0.17	0.001–0.01	420–500	42
Alloy-D	0.16	0.001–0.01	450–500	36
Alloy-E	0.14	0.001–0.01	470–500	32

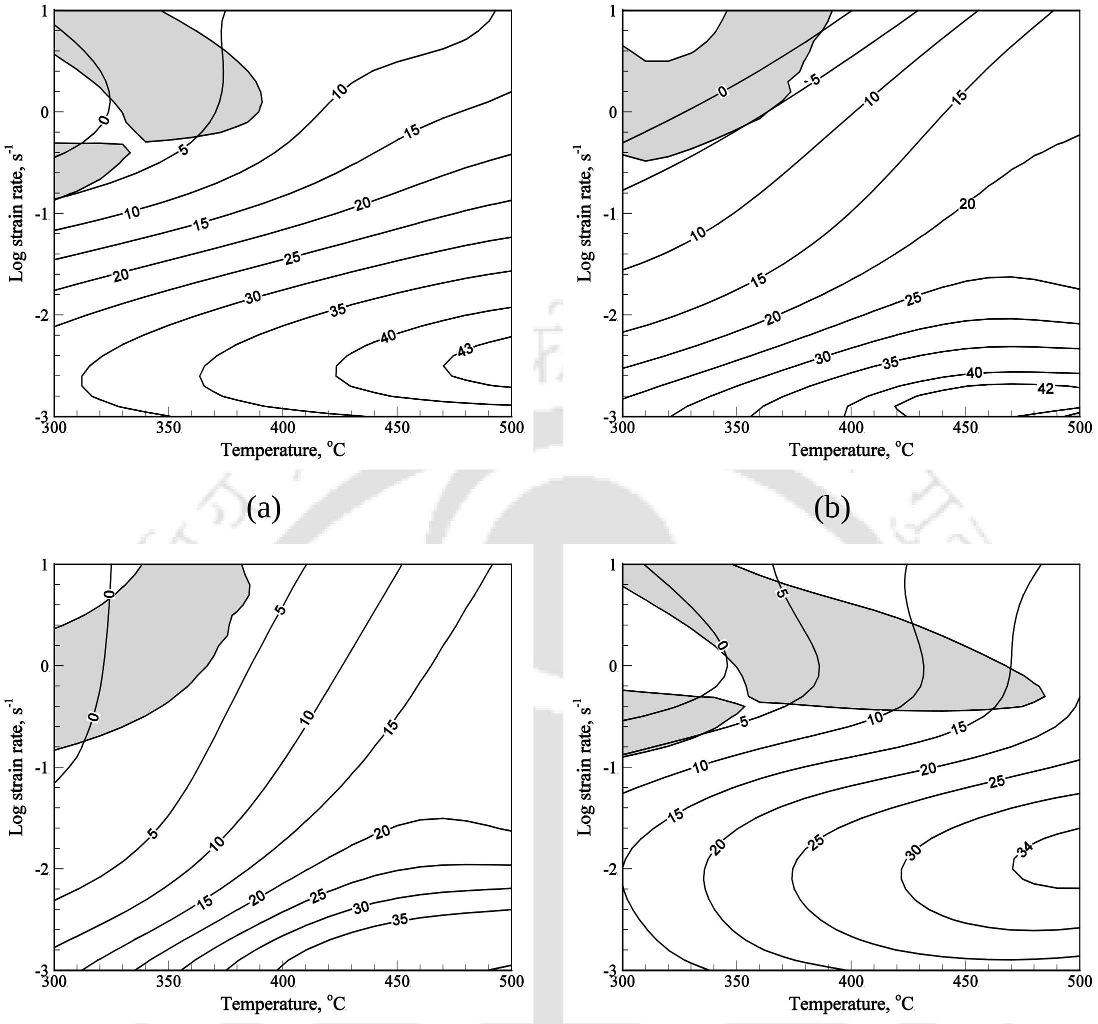

(a) (b)

(c) (d)

Figure 4.43 Contour plots of deformation processing map at strain 0.6 for (a) Alloy-B, (b) Alloy-C, (c) Alloy-D and (d) Alloy-E

Microstructure of the specimen after hot deformation was observed using optical microscope to investigate the dissipative microstructures formed during the hot deformation. The microstructure of Alloy-A before hot deformation has been shown in Figure 4.44 (a). Figure reveals the following; (i) almost equiaxed grains (ii) presence of second phase ($CuAl_2$) particles and (iii) small amount of low melting point phases at the grain boundary regions. Figure 4.44 (b) & (c) reveals features typical of inter-granular cracking along the grain boundary regions. These micrographs correspond to the samples which were deformed at 300 ºC and strain rates of 10 s^{-1} and 1 s^{-1}, respectively. Referring to Figure 4.41 these process

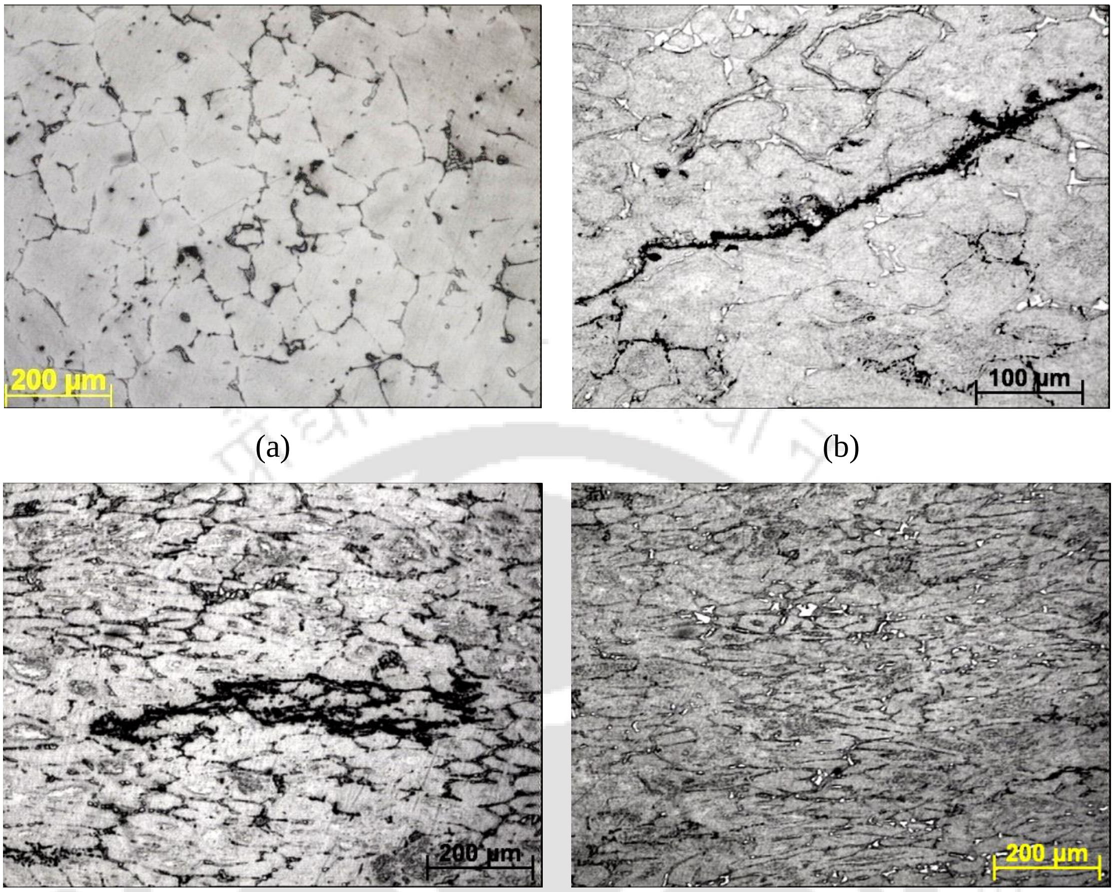

(a) (b)

(c) (d)

Figure 4.44 Optical micrograph of Alloy-A (a) before hot deformation (X10 magnification), (b) inter-granular cracking (X20 magnification) along the grain boundary regions at strain rate 10 s^{-1} at 300 °C, (c) inter–granular cracking (X10 magnification) along the grain boundary regions at strain rate 1 s^{-1} at 300 °C and (d) Dynamic recrystallized grains (X10 magnification) at strain rate at strain rate 0.01 s^{-1} and temperature 500 °C

corresponds to the regimes of plastic instability (shown shaded). It has been reported that inter-granular cracking can occur in materials having low melting points when subjected to plastic deformation at intermediate temperatures and high strain rates [29]. Presence of $CuAl_2$ and small amounts of low melting point phases at grain boundary regions results in the plastic instability during hot deformation by inter-crystalline cracking. Figure 4.44 (d) shows the microstructure of Alloy-A deformed at temperature 500 °C and strain rate of 0.01 s^{-1}. Referring to Figure 4.41 this process condition corresponds to the regime of stable plastic flow (i.e. safe region). The micrograph reveals fine recrystallized grains nucleated at the grain boundaries indicating dynamic recrystallization.

Dynamic recrystallization is beneficial [94] since softens the material and provides a stable flow during hot deformation [95]. From the observations made from Figure 4.41 Figure 4.44 one can arrive at the fact that the safe process regimes for hot deformation of Alloy-A are at; (i) strain rates in the range 0.001 s^{-1} – 0.1 s^{-1} for all temperatures and (ii) temperature in the range 380–500 °C for all strain rates.

Photomicrographs of Alloy-B before and after deformation at strain rate 1.0 s^{-1} and 300 °C has been shown in Figure 4.45 (a) and Figure 4.45 (b), respectively. Figure 4.45(b) reveals void formation at triple junctions. The void formation results in stress relieving during deformation. The photomicrographs of Alloy-D deformed at temperature 300 °C and strain rate 1.0 s^{-1} has been shown in Figure 4.46 (a). The figure reveals void formation at grain boundary regions when deformed at low temperature and high strain rate. The microstructure of Alloy-D after deformation at temperature 500 °C and strain rate 0.001 s^{-1} has been shown in Figure 4.46 (b). The features represent dynamic recrystallization when deformed at high temperature and low strain rates. This region is considered to be a safe process zone. From Figure 4.43(c) and 4.46 the safe process regime for hot deformation of Alloy-D identified as; (i) low strain rates in the range 0.001–0.1 s^{-1} for all temperatures and (ii) at temperatures in the range 380–500 °C for all strain rates.

Optical micrographs of Alloy-E deformed at (a) 300 ºC temperature and strain rate 10 s^{-1} and (b) 500 °C temperature and strain rate 0.001 s^{-1} has been shown in Figure 4.47 (a) and Figure (b), respectively. Figure 4.47(a) reveals void formation during hot deformation whereas Figure 4.47 (b) reveals dynamic recrystallization along with small amount of flow localization. The silver content in Alloy-E is 0.1 wt.% silver. Figure 4.43 (d) reveals lower efficiency of power dissipation, η (~23%) value at 500 ºC temperature and strain rate 0.001 s^{-1} compared to other alloys. Though dominant microstructural feature at this condition is dynamic recrystallization, the formation of flow localization reduces the efficiency of power dissipation (η) for this alloy.

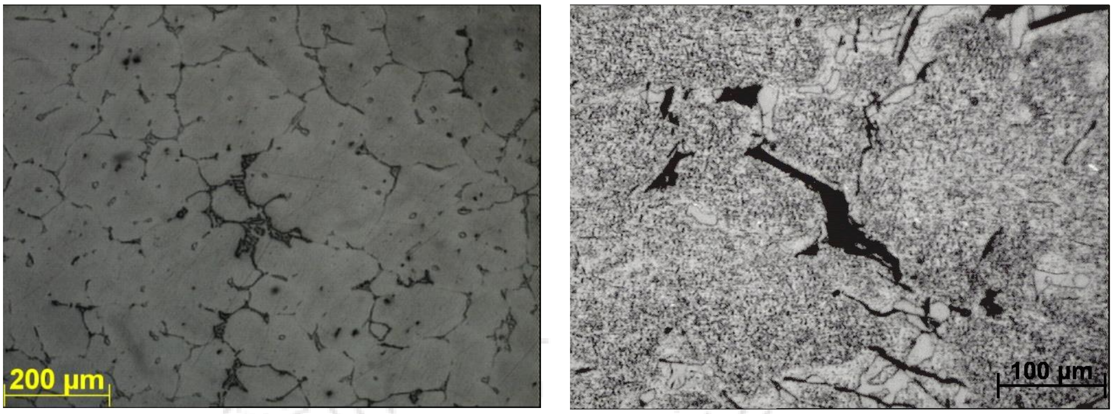

(a) (b)

Figure 4.45 Optical micrograph of Alloy-B (a) before hot deformation (X10 magnification) and (b) void formation at triple junctions (X20 magnification) at strain rate 1 s^{-1} and temperature 300 °C

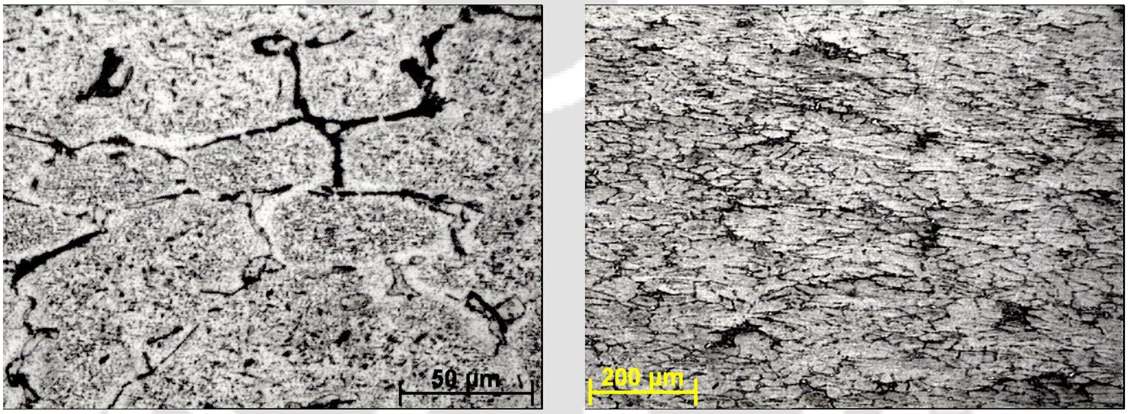

(a) (b)

Figure 4.46 Optical micrograph of Alloy-D (a) void formation at grain boundary (X50 magnification) strain at rate 1 s^{-1} and temperature 300 °C and (b) dynamic recrystallization (X10 magnification) at strain rate 0.001 s^{-1} and temperature 500 °C

The regimes of flow instability during hot working of the investigated alloys have been identified. The instability regimes of all alloys are presented in Table 4.19. From the comparison of the deformation processing maps and microstructural investigations the findings can be summarized as follows:

a. The instability regimes in the alloys are at regions of high strain rates and low temperatures.

b. Stable regime for hot deformation decreases with increase in silver content.

c. Void nucleation and intercrystalline cracking are the major mechanisms of flow instability in these alloys. Flow localization is observed in alloy containing 0.1 wt.% silver resulting in reduction in the efficiency of power dissipation.

d. High efficiency of power dissipation corresponds to regimes of stable plastic flow.

e. The safe plastic flow regimes during hot deformation are characterized by dynamic recrystallization.

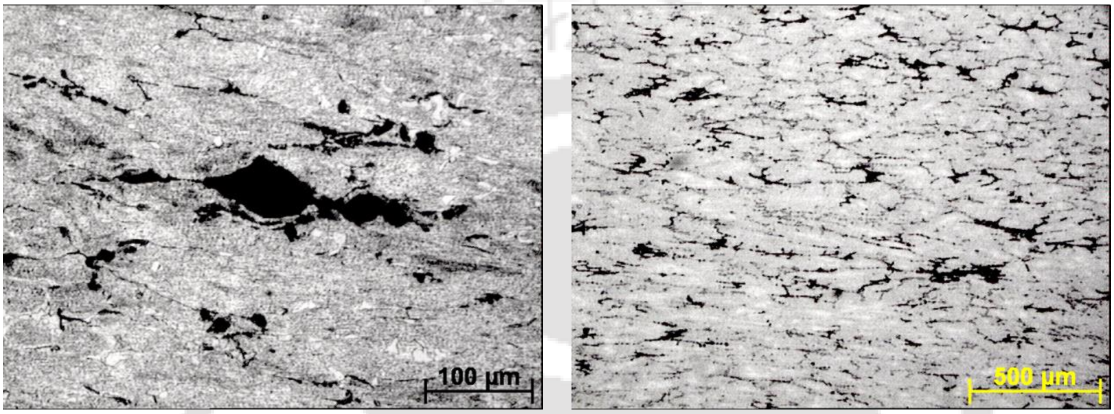

(a) (b)

Figure 4.47 Optical micrograph of Alloy-E (a) void formation (X20 magnification) at strain rate 10 s^{-1} and 300 °C and (b) dynamic recrystallization (X5 magnification) along with small amount of flow localization at strain rate 0.001 s^{-1} and 500 °C

Table 4.19. Metallurgical interpretation of Alloy

Sample ID	Manifestation	Strain-rate ranges (s^{-1})	Temperature (°C)
Alloy-A	Inter-granular cracking	0.125–10.00	300–380
	Dynamic recrystallization	0.001–0.01	480–500
Alloy-B	Void formation at triple junctions	0.125–1.00	300–370
	Dynamic recrystallization	0.001–0.01	460–500
Alloy-D	Void formation	0.316–1.00	300–390
	Dynamic recrystallization	0.001–0.01	400–500
Alloy-E	Void formation	0.125–10.00	300–480
	Dynamic recrystallization	0.010–0.10	480–500

Chapter 5

Conclusion and Scope of Future Work

5.1 Conclusion

Al-Cu-Zn-Fe-Ti-Si-Mg-Mn (≈2219 Al-alloy) containing trace additions (varying in the range 0 to 0.1 wt.%) of silver was processed by casting route and subjected to different thermo-mechanical treatments. The mechanical properties, microstructure and age hardening behavior of these alloys were investigated systematically. The constitutive parameters for the hot deformation behavior of these alloys were determined. Processing maps were generated for delineating the safe and un-safe regimes during hot deformation of these alloys, using artificial neural network. The main conclusions arrived at from the present work are as follows:

- The cast alloys revealed dendrite structures. Two types of secondary phases: $CuAl_2$ and Al-Fe-Cu-Si-Mn phase, were observed at the grain boundary regions.
- The volume of the Al-Fe-Cu-Si-Mn phase increased with increase in silver content in the alloy.
- Solutionizing heat treatment resulted in almost disappearance of the Al-Fe-Cu-Si-Mn phase.
- The average grain diameter of alloy increased with increase in silver content.
- The hardness of the alloy increased uniformly with increase in silver percentage under rolled and heat treated conditions.
- Peak hardness in all the alloys was attained on ageing at 150 °C for 45 hours.
- The maximum hardness was observed in the alloy with 0.07 wt.% silver (Alloy-D).
- The yield strength and ultimate tensile strength of the rolled and age hardened alloy increased with increase in silver content up to 0.07 wt.% . The percentage of elongation in these alloys was 10%. The alloy with 0.07 wt.% silver exhibited 30% and 15% increase in yield strength (YS) and ultimate tensile strength (UTS), respectively, compared to the standard 2219 Al alloy.
- During the hot deformation, peak flow stress of the alloys decreased with increase in silver content.

- Flow softening occurs during hot deformation at temperatures above 400 °C. Flow softening was higher at lower strain rates.

- Presence of silver in 2219 aluminum alloy reduced the activation energy for hot deformation.

- Zener-Hollomon parameter (Z) and the constants in the constitutive model for hot deformation were determined. More than 88% of the peak flow stress values could be predicted using the constitutive equations with deviation error within ± 12.5%.

- Flow stress as a function of strain, strain rate and temperature during hot deformation was predicted for all alloys by artificial neural network modeling. The coefficient of determinant (R^2) during the prediction of more than 0.97 indicates very good prediction capability by artificial neural network (ANN) technique.

- Strain rate sensitivity value, m for the investigated alloys were higher at high temperatures (500 °C) and low strain rate (0.001 s^{-1}) regimes.

- Maximum efficiency of power dissipation η_{max} for Alloy-A was 54% at regimes of low strain rates and high temperature for a strain value of 0.6. Efficiency of power dissipation decreased with increase in silver content in the alloy.

- The instability maps and deformation mechanism maps reveals metallurgical instability at processing regimes of low temperature and high strain rates. The instability regime increased with increase in strain towards region of higher temperature.

- The instability regime increased with increase in silver content in the alloy. For Alloy-A the instability regime at a strain of 0.6 is found to be at strain rate > 0.1 s^{-1} and temperatures between 300–370 °C whereas for Alloy-E containing 0.1 wt.% silver, the unstable region is at strain rates > 0.1 and temperatures from 300–475 °C.

- Defect formation during hot deformation in the investigated alloys is driven by voids at triple junction points and intergranular cracking at high strain rates and low temperatures and by localized shear band formation at high strain rates and temperatures.

- Dynamic recrystallization is the main mechanism of flow softening. This occurs at regimes of plastic stability.

The investigation carried out establishes the influence of microalloying with silver on the microstructure, mechanical properties and hot deformation behavior of 2219 aluminum alloy. The results indicate that mechanical working and/or heat treatments of the as-cast alloy is required for achieving improved mechanical properties. The best combination mechanical properties was achieved for the thermo-mechanically processed alloy containing 0.07 wt.% silver. The mechanical properties of these alloys achieved for this alloy was better than the standard 2219 Al alloy. Microstructural investigation of the hot worked samples reveal the safe processing zone for these alloys has a strong influence on the silver content. Prediction of flow stress by artificial neural network (ANN) modeling demonstrates excellent prediction capability.

5.2 Scope for future work

The present study was focused on understanding the influence of trace additions of silver on the microstructure and mechanical properties of Al-Cu alloy. The results indicate improvement in mechanical properties of Al-Cu alloy by microalloying. A few of the future scope of the investigation which are required to be addressed are enumerated below:

1. Influence of microalloying with combination of more than one element viz. titanium (Ti), silver (Ag), tin (Sn), lead (Pb), cadmium (Cd), vanadium (V) etc. on the microstructure and mechanical properties of high strength 2xxx, 6xxx and 7xxx series aluminum alloys.
2. Investigation of microstructure, mechanical properties and strengthening mechanism of aluminum alloys microalloyed with nano-tubes of titanium (Ti), copper (Cu), iron (Fe) etc.
3. In depth study on the precipitation sequence and kinetics of microalloyed aluminum alloys. Study should be supported by extensive investigation of transmission electron microscope (TEM).

4. Generation of deformation mechanism map for newly developed ferrous or non-ferrous alloy with the combination of strain, strain rate and temperature for industrial application.
5. So far no work has been reported regarding fracture toughness, fatigue crack growth of microalloyed aluminum alloys. These studies are very important especially of light weight structural applications. Future work should be centered on studying these properties under different thermo-mechanical conditions, supported by microscopic investigation.

References

1 Metals Handbook Properties and Selection: Non-Ferrous Alloys and Special Purpose Materials, vol. 2, ASM International, Metals Park, OH, USA, 10th edition, (1990).

2 J. Gilbert Kaufman, Introduction to aluminum alloys and tempers, ASM International, (2000).

3 W.D. Callister and G.R. David, Materials Science and engineering: an Introduction, 7th edition, John Wiley & Sons, Inc, (2009).

4 A.Heinz, A.Haszler, C.Keidel, S.Moldenhauer, R.Benedictus and W.S.Miller, Recent development in aluminum alloys for aerospace applications, Materials Science and Engineering: A, 280 (2000) pp. 102–107.

5 V. Elagin, Ways of developing high-strength and high-temperature structural aluminum alloys in the 21st century, Metal Science and Heat Treatment, 49 (2007) pp. 427–434.

6 T.V. Rajan, C.P. Sharma and A. Sharma, Heat treatment: Principles and techniques, PHI Learning Pvt. Ltd., (2011).

7 Ø. Ryen, B. Holmedal, O. Nijs, E. Nes, E. Sjölander and H.E. Ekström, Strengthening mechanisms in solid solution aluminum alloys, Metallurgical and Materials Transactions A, 37 (2006) pp. 1999–2006.

8 W. Miao and D. Laughlin, Effects of Cu content and preaging on precipitation characteristics in aluminum alloy 6022, Metallurgical and Materials Transactions A, 31 (2000) pp. 361–371.

9 R. Livak, The effects of copper and chromium on the aging response of dilute Al-Mg-Si alloys, Metallurgical transactions A, 13 (1982) pp. 1318–1321.

10 L. Tarasenko, N. Kolobnev and L. Khokhlatova, Phase composition and mechanical properties of alloys of the Al-Mg-Li-Me system, Metal Science and Heat Treatment, 50 (2008) pp. 80–82.

11 G. Wang, Q. Sun, L. Shan, Z. Zhao and L. Yan, Influence of indium trace addition on the precipitation behavior in a 357 cast aluminum alloy, Journal of Materials Engineering and Performance, 16 (2007) pp. 752–756.

12 L. Weijing, C. Shihai, H. Jianmin and X. Chao, Effect of Silicon on the casting properties of Al–5.0% Cu alloy, Rare Metals, 25 (2006) pp. 133–135.

13 V. Zakharov, Effect of scandium on the structure and properties of aluminum alloys, Metal Science and Heat Treatment, 45 (2003) pp. 246–253.

14 S. Hirosawa, T. Sato, A. Kamio and H. Flower, Classification of the role of microalloying elements in phase decomposition of Al based alloys, Acta Materialia, 48 (2000) pp. 1797–1806.

15 P.N. Raju, K.S. Rao, G. Reddy, M. Kamaraj and K.P. Rao, Microstructure and high temperature stability of age hardenable AA2219 aluminum alloy modified by Sc, Mg and Zr additions, Materials Science and Engineering: A, 464 (2007) pp. 192–201.

16 K. Yu, W. Li, S. Li and J. Zhao, Mechanical properties and microstructure of aluminum alloy 2618 with Al_3(Sc, Zr) phases, Materials Science and Engineering: A, 368 (2004) pp. 88–93.

17 S. Banerjee, P. Robi, A. Srinivasan and P.K. Lakavath, Effect of trace additions of Sn on microstructure and mechanical properties of Al–Cu–Mg alloys, Materials & Design, 31 (2010) pp. 4007–4015.

18 H. Kamali, M. Emamy and A. Razaghian, The influence of Ti on the microstructure and tensile properties of cast Al–4.5Cu–0.3Mg alloy, Materials Science and Engineering: A, 590 (2014) pp. 161–167.

19 S. Banerjee, P. Robi, A. Srinivasan and L.P. Kumar, High temperature deformation behavior of Al–Cu–Mg alloys micro-alloyed with Sn, Materials Science and Engineering: A, 527 (2010) pp. 2498–2503.

20 H.Z. Li, X.M. Zhang, M.A. Chen and Z.P. Zhou, Effects of Ag on microstructure and mechanical properties of 2519 aluminum alloy, Journal of Central South University of Technology, 13 (2006) pp. 130–134.

21 X.Y. Liu, Q.L. Pan, Y.B. He, W.B. Li, W.J. Liang and Z.M. Yin, Flow behavior and microstructural evolution of Al–Cu–Mg–Ag alloy during hot compression deformation, Materials Science and Engineering: A, 500 (2009) pp. 150–154.

22 X.Y. Liu, Q.L. Pan, C.G. Lu, Y.B. He, W.B. Li and W.J. Liang, Microstructure and mechanical properties of Al–Cu–Mg–Mn–Zr alloy with trace amounts of Ag, Materials Science and Engineering: A, 525 (2009) pp. 128–132.

23 H. Qi, X.Y. Liu, S.X. Liang, X.L. Zhang, H.X. Cui, L.Y. Zheng, F. Gao and Q.H. Chen, Mechanical properties and corrosion resistance of Al–Cu–Mg–Ag heat-resistant alloy modified by interrupted aging, Journal of Alloys and Compounds, 657 (2016) pp. 318–324.

24 K. Hono, T. Sakurai and I. Polmear, Pre-precipitate clustering in an Al-Cu-Mg-Ag alloy, Scripta metallurgica et materialia, 30 (1994) pp. 695–700.

25 S. Ringer, T. Sakurai and I. Polmear, Origins of hardening in aged Al-Cu-Mg-(Ag) alloys, Acta materialia, 45 (1997) pp. 3731–3744.

26 S. Ringer, K. Hono, I. Polmear and T. Sakurai, Nucleation of precipitates in aged Al-Cu-Mg-(Ag) alloys with high Cu:Mg ratios, Acta Materialia, 44 (1996) pp. 1883–1898.

27 H.J. McQueen and N.D. Ryan, Constitutive analysis in hot working, Material Science and Engineering: A, 322 (2002) pp. 43–63.

28 H.J. McQueen and M.E. Kassner, Elevated temperature deformation: Hot working amplifies creep, Material Science and Engineering: A, 410 (2005) pp. 58–61.

29 H. Wu, L. Du and X. Liu, Dynamic recrystallization and precipitation behavior of Mn-Cu-V weathering steel, Journal of Materials Science & Technology, 27 (2011) pp. 1131–1138.

30 W. Liu, H. Zhao, D. Li, Z. Zhang, G. Huang and Q. Liu, Hot deformation behavior of AA7085 aluminum alloy during isothermal compression at elevated temperature, Materials Science and Engineering: A, 596 (2014) pp. 176–182.

31 G. Wang, L. Xu, Y. Wang, Z. Zheng, Y. Cui and R. Yang, Processing maps for hot working behavior of a PM TiAl alloy, Journal of Materials Science & Technology, 27 (2011) pp. 893–898.

32 Y.Q. Yang, Y.A. Dong, Q.Z. Zhang, L.F. Cao, X.D. Wu, G.J. Huang and L.I. Qing, Flow behavior and microstructure evolution of 6A82 aluminium alloy with high copper content during hot compression deformation at elevated temperatures, Transactions of Nonferrous Metals Society of China, 26 (2016) pp. 649–657.

33 B. Li, Q. Pan and Z. Yin, Characterization of hot deformation behavior of as-homogenized Al–Cu–Li–Sc–Zr alloy using processing maps, Materials Science and Engineering: A, 614 (2014) pp. 199–206.

34 S.Y. Park and W.J. Kim, Difference in the hot compressive behavior and processing maps between the as-cast and homogenized Al-Zn-Mg-Cu (7075) alloys, Journal of Materials Science & Technology, 32 (2016) pp. 660–670.

35 H.E. Hu, L. Zhen, L. Yang, W.Z. Shao and B.Y. Zhang, Deformation behavior and microstructure evolution of 7050 aluminum alloy during high temperature deformation, Materials Science and Engineering: A, 488 (2008) pp. 64–71.

36 S.F. Medina and C.A. Hernandez, General expression of the Zener-Hollomon parameter as a function of the chemical composition of low alloy and microalloyed steels, Acta Materialia, 44 (1996) pp. 137–148.

37 Y.V.R.K. Prasad, H.L. Gegel, S.M. Doraivelu, J.C. Malas, J.T. Morgan, K.A. Lark and D.R. Barker, Modeling of dynamic material behavior in hot deformation: forging of Ti-6242, Metallurgical Transactions A, 15 (1984) pp. 1883–1892.

38 H. Zhang, L. Li, D. Yuan and D. Peng, Hot deformation behavior of the new Al–Mg–Si–Cu aluminum alloy during compression at elevated temperatures, Materials Characterization, 58 (2007) pp. 168–173.

39 Y.V.R.K. Prasad and S. Sasidhara, Hot working guide: A compendium of processing maps, ASM International, Materials Park, OH. (1997).

40 P.S. Robi and U.S. Dixit, Application of neural networks in generating processing map for hot working, Journal of Materials Processing Technology, 142 (2003) pp. 289–294.

41 Y.V.R.K. Prasad, Recent advances in the science of mechanical processing, Indian Journal of Technology, 28 (1990) pp. 435–451.

42 Y.V.R.K Prasad and N. Ravichandran, Effect of stacking fault energy on the dynamic recrystallization during hot working of FCC metals: A study using processing maps, Bulletin of Material Science, 14 (1991) pp. 1241–1248.

43 Y.V.R.K. Prasad, T. Seshacharyalu, S.C. Medeiors and W.G. Frazier, Effect of preform microstructure on the hot working mechanisms in ELI grade Ti–6Al–4V: transformed β v. equiaxed (α + β), Material Science and Technology, 16 (2000) pp. 511–516.

44 S. Banerjee, P.S. Robi and A. Srinivasan, Deformation Processing Maps for Control of Microstructure in Al-Cu-Mg Alloys Microalloyed with Sn, Metallurgical and Materials Transactions A, 43 (2012) pp. 3834–3849.

45 S.G. Shabestari, The effect of iron and manganese on the formation of intermetallic compounds in aluminum–silicon alloys, Materials Science and Engineering: A, 383 (2004) pp. 289–298.

46 E.M. Taleff, G.A. Henshall, T.G. Nieh, D.R. Lesuer and J. Wadsworth, Warm-temperature tensile ductility in Al-Mg alloys, Metallurgical and Materials Transactions A, 29 (1998) pp. 1081–1091.

47 V.I. Elagin, Ways of developing high-strength and high-temperature structural aluminum alloys in the 21st century, Metal Science and Heat Treatment, 49 (2007) pp. 427–434.

48 George E. Dieter, Mechanical Metallurgy, SI Metric edition (1988).

49 D.J. Chakrabarti, B.K. Cheong and D.E. Laughlin, Automotive Alloys II, TMS Annual Meeting, San Antonio, (1998) pp. 27–44.

50 D.K. Chatterjee and K.M. Entwistle, A study of the effect of magnesium loss and of the addition of copper on the aging of aluminum-magnesium-silicon alloys, Journal of the Institute of Metals, 101 (1973) pp. 53–59.

51 T. Sakurai and T. Eto, Proc. 3rd Int. Conf. Aluminum (eds. L. Arnberg, O. Lohne, E. Nes and N. Ryum) 1 (1992) 220–225.

52 H. Suzuki, M. Kanno and G. Itoh, A consideration on two-step aging in Al-Mg-Si alloy, Journal of Japan Institute of Light metals, 30 (1980) pp. 609–616.

53 M. Tamizifar and G.W. Lorimer, Proc. 3rd Int. Conf. Aluminum (eds. L. Arnberg, O. Lohne, E. Nes and N. Ryum) 1 (1992) pp. 220–225.

54 S.P. Wen, Z.B. Xing, H. Huang, B.L. Li, W. Wang and Z.R. Nie, The effect of erbium on the microstructure and mechanical properties of Al–Mg–Mn–Zr alloy, Materials Science and Engineering: A, 516 (2009) pp. 42–49.

55 A.M. Mohamed, F.H. Samuel, A.M. Samuel, H.W. Doty and S. Valtierra, Influence of tin addition on the microstructure and mechanical properties of Al-Si-Cu-Mg and Al-Si-Mg casting alloys, Metallurgical and Materials Transactions A, 39 (2008) pp. 490–501.

56 E. Orowan, Symposium on Internal Stresses in Metals, Institute of Metals, London, (1948) pp. 451–453.

57 E. Hornbogen, Hundred years of precipitation hardening, Journal of light Metals, 1 (2001) pp. 127–132.

58 W.J. Liang, Q.L. Pan, Y.B. He, Y.C. Li and X.G. Zhang, Flow stress behavior of Al-Cu-Li-Zr alloy containing Sc during hot compression deformation, Journal of Central South University and Technology, 15 (2008) pp. 289–294.

59 J.R. Cho, W.B. Bae, W.J. Hwang and P. Hartley, A study on the hot-deformation behavior and dynamic recrystallization of Al–5wt.% Mg alloy, Journal of Materials Processing Technology, 118 (2001) pp. 356–361.

60 T.J. Smith, H. Sehitoglu, E. Fleury, H.J. Maier and J. Allison, Modeling high-temperature stress-strain behavior of cast aluminum alloys, Metallurgical and Materials Transactions A, 30 (1999) pp. 133–146.

61 R. Kaibyshev, O. Sitdikov, I. Mazurina and D.R. Lesuer, Deformation behavior of a 2219 Al alloy, Material Science and Engineering: A, 334 (2002) pp. 104–113.

62 P. Cavaliere, Hot and warm forming of 2618 aluminium alloy, Journal of Light Metals, 2 (2002) pp. 247–252.

63 F. Bardi, M. Cabibbo, E. evangelista, S. Spigarelli and M. Vukcevic, An analysis of hot deformation of an Al–Cu–Mg alloy produced by powder metallurgy, Material Science and Engineering: A, 339 (2003) pp. 43–52.

64 S. Spigarelli, M. Cabibbo, E. Evangelista and J. Bidulska, A study of the hot formability of an Al-Cu-Mg-Zr alloy, Journal of Materials Science, 38 (2003) pp. 81–88.

65 A. Gholamzadeh and A.K. Taheri, The prediction of hot flow behavior of Al–6% Mg alloy, Mechanics Research Communications, 36 (2009) pp. 252–259.

66 X.Y. Liu, Q.L. Pan, Y.B. He, W.B. Li, W.J. Liang and Z.M. Yin, Flow behavior and microstructural evolution of Al–Cu–Mg–Ag alloy during hot compression deformation, Materials Science and Engineering: A, 500(2009) pp. 150–154.

67 H. Zhang, L. Li, D. Yuan and D. Peng, Hot deformation behavior of the new Al–Mg–Si–Cu aluminum alloy during compression at elevated temperatures, Material Characterization, 58 (2007) pp. 168–173.

68 C.M. Sellars and W.J. McG. Tegart, Mem. Sci. Rev. Metall, 63 (1966) pp. 731–746.

69 W.J. McG. Tegart, Ductility, American Society of Metals, Metals Park, Ohio, (1968) Chap. 5.

70 A.K. Ghosh, A physically-based constitutive model for metal deformation, Acta Metallurgica, 28 (1980) pp. 1443–1465.

71 C.G. Schmidt and A.K. Miller, A unified phenomenological model for non-elastic deformation of type 316 stainless steel, Res Mechanica, 3 (1981) pp. 109–129.

72 Z.Y. Chen, S.Q. Xu and X.H. Dong, Deformation behavior of AA6063 aluminium alloy after removing friction effect under hot working conditions, Acta Metallurgica Sinica (English Letters), 21 (2008) pp. 451–458.

73 E. Evangelista, A. Forcellesa, F. Gabrielli and P. Mengucci, Hot formability of AA 6061 PM aluminium alloy, Journal of Materials Processing Technology, 24 (1990) pp. 323–332.

74 S.F. Medina and C.A. Hernandez, General expression of the Zener-Hollomon parameter as a function of the chemical composition of low alloy and microalloyed steels, Acta Materialia, 44 (1996) pp. 137–148.

75 Y. Wang, W.Z. Shao, L. Zhen, L. Yang and X.M. Zhang, Flow behavior and microstructures of superalloy 718 during high temperature deformation, Material Science and Engineering: A, 497 (2008) pp. 479–486.

76 H. Takuda, H. Fujimoto and N. Hatta, Modelling on flow stress of Mg–Al–Zn alloys at elevated temperatures, Journal of Materials Processing Technology, 80 (1998) pp. 513–516.

77 H. Yang, Z.H. Li and Z.L. Zhang, Investigation on Zener-Hollomon parameter in the warm-hot deformation behavior of 20CrMnTi, Journal of Zhejiang University Science A, 7 (2006) pp. 1453–1460.

78 B.L. Zhang, M.S. Maclean and T.N. Baker, Hot deformation behaviour of aluminium alloy 6061/SiCp MMCs made by powder metallurgy route, Material Science and Technology, 16 (2000) pp. 897–902.

79 C. Zener and J.H. Holloman, Effect of strain rate upon plastic flow of steel, Journal of Applied Physics, 15 (1944) pp. 22–32.

80 E. Cerri, P. Leo and P.P. De Marco, Hot compression behavior of the AZ91 magnesium alloy produced by high pressure die casting, Journal of Materials Processing Technology, 189 (2007) pp. 97–106.

81 B. Ronning and N. Ryum, Constitutive relationships for AlZnMg, AlZnMgCr, and AlZnMgZr alloys, Metallurgical and Materials Transactions A, 32 (2001) pp. 769–776.

82 W.S. McCulloch and W. Pitts, A logical calculus of the ideas immanent in nervous activity, The bulletin of mathematical biophysics, 5 (1943) pp.115–133.

83 R. Ravi, Y.V.R.K. Prasad and V.V.S. Sharma, Artificial neural network models to predict workability parameters for dynamic recrystallisation domain and instability regimes, International Workshop on Neural Network and Genetic Algorithm in Material Science and Engineering (NGMS-2006), (2006) pp. 257–271.

84 S. Banerjee, P.S. Robi and A. Srinivasan, Prediction of hot deformation behavior of Al–5.9%Cu–0.5% Mg alloys with trace additions of Sn, Journal of Materials Science, 47 (2012), pp. 929–948.

85 J.M. Zurada, Introduction to artificial neural systems, St. Paul: West, vol. 8 (1992).

86 P.W. Flynn, J. Mote and J.E. Dorn, On the thermally activated mechanism of prismatic slip in magnesium single crystals, Transactions of the Metallurgical Society of AIME, 221 (1961) pp. 1148–1154.

87 J.J. Jonas, C.M. Sellars and W.J.McG. Tegart, Strength and structure under hot-working conditions, Metallurgical Reviews, 14 (1969) pp. 1–24.

88 H.J. Frost and M.F. Ashby, Deformation-mechanism maps, Pergamon Press, New York and Oxford, (1982).

89 R. Raj, Development of a processing map for use in warm-forming and hot-forming processes, Metallurgical and Materials Transactions A, 12 (1981) pp. 1089–1097.

90 V.V. Kutumba Rao and T. Rajagopalachary, Recent developments in modeling the hot working behavior of metallic materials, Bulletin of Material Science, 19 (1996) pp. 677–698.

91 H.J. McQueen, E. Evangelista, N.D. Ryan and T Chandra, Recrystallization ('90) in Metals and Materials, TMS-AIME, Warrendale, PA (1990), pp. 89–100.

92 W. Roberts, Deformation Processing and Structure, Ed. G. Krauss, ASM, Metals Park, OH. (1984).

93 T. Sakai and J.J. Jonas, Overview no. 35 dynamic recrystallization: mechanical and microstructural considerations, Acta Metallurgica, 32 (1984) pp. 189–209.

94 C. Gandhi, On fracture initiation mechanisms and dynamic recrystallization during hot deformation of pure nickel, Metallurgical Transactions A, 13 (1982) pp. 1233–1238.

95 C.M. Styles, I. Sinclair, P.J. Gregson and S.M. Flitcroft, Effect of microstructure on mechanical properties of thermomechanically processed 2124–SiCp metal matrix composite, Material Science and Technology, 10 (1994) pp. 475–480.

96 S.V.S. Narayana Murty, B.N. Rao and B.P. Kashyap, Instability criteria for hot deformation of materials, International Materials Reviews, 45 (2000) pp. 15–26.

97 Y.V.R.K. Prasad, T. Seshacharyalu, S.C. Medeiors and W.G. Frazier, Effect of preform microstructure on the hot working mechanisms in ELI grade Ti–6Al–4V: transformed β v. equiaxed (α+ β), Material Science and Technology, 16 (2000) pp. 511–516.

98 N. Ravichandran and Y.V.R.K Prasad, Dynamic recrystallization during hot deformation of aluminum: a study using processing maps, Metallurgical Transactions A, 22 (1991) pp. 2339–2348.

99 M.J. Luton and C.M. Sellars, Dynamic recrystallization in nickel and nickel-iron alloys during high temperature deformation, Acta Metallurgica, 17 (1969) pp. 1033–1043.

100 H. Ziegler, Some extremum principles in irreversible thermodynamics with application to continuum mechanics, In Progress in Solid Mechanics, vol. 4, SneddonIN, HillR (eds). North-Holland: Amsterdam, (1963).

101 A.K.S. Kalyan Kumar, MS Thesis, Indian Institute of Science, Bangalore, India. (1987).

102 D. Zhao, P.K. Chaudhury, M. Thirukkonda and J.J. Valencia, Intermetallic Matrix Composites III, Pittsburgh, Materials Research Society. 350 (1994) pp. 273–281.

103 A. Al Omar, J.M. Cabrera and J.M. Prado, Characterization of the hot deformation in a microalloyed medium carbon steel using processing maps, Scripta Materialia, 34 (1996) pp. 1303–1308.

104 S. Venugopal, S.L. Mannan and Y.V.R.K. Prasad, Influence of state of stress on the processing map for hot working of stainless steel type AISI 304L: compression vs. torsion, Material Science and Engineering: A, 60 (1993) pp. 63–69.

105 S. Ramanathan, R. Karthikeyan, V. Deepak Kumar and G. Ganesan, Journal of Material Science and Technology, 22 (2006) pp. 611–615.

106 K.P. Rao, Y.V.R.K. Prasad and K. Sivaram, Deformation processing map for control of microstructure in Al–4Mg alloy, Materials Letters, 10 (1990) pp. 66–70.

107 E. Cerri, S. Spigarelli, E. Evangelista and P. Cavaliere, Hot deformation and processing maps of a particulate-reinforced 6061+20%Al_2O_3 composite, Material Science and Engineering: A, 324 (2002) pp. 157–161.

108 S.V. Kailas, Y.V.R.K. Prasad and S.K. Biswas, Microstructural Features of Flow, Metallurgical Transactions A, 24 (1993) pp. 2513–2520.

109 G. Meng, B Li, H. Li, H. Huang and Z. Nie, Hot deformation and processing maps of an Al–5.7wt.% Mg alloy with erbium, Material Science and Engineering: A, 517 (2009) pp. 132–137.

110 S. Yang, D. Yi, H. Zhang and S. Yao, Flow stress behavior and processing map of Al-Cu-Mg-Ag alloy during hot compression, Journal of Wuhan University of Technology–Materials Science Edition, 23 (2008) pp. 694–698.

111 P.L. Jain, Principles of foundry technology. Tata McGraw-Hill Education (2003).

112 P.N. Rao, Manufacturing technology, Tata McGraw-Hill Education, vol. 1 (2013).

113 Metallography and Microstructures, American Society for Metals, Metals Handbook, 9th edition, Vol. 9 (1986).

114 Annual handbook of ASTM standards, metals test methods and analytical procedures, vol. 03.01 section 3 (1997).

115 L.F. Mondolfo, Aluminum Alloys, Structure and Properties. London: Butterworths. (1976).

116 J. L. Murray, The aluminium-copper system, International metals reviews, 30 (1985) pp. 211–234.

117 M. Murayama and K Hono, Role of Ag and Mg on precipitation of T1 phase in an Al-Cu-Li-Mg-Ag alloy, Scripta materialia, 44 (2001) pp. 701–706.

118 A.K. Mukhopadhyay, Compositional characterization of Cu-rich phase particles present in as-cast Al-Cu-Mg (-Li) alloys containing Ag, Scripta materialia, 41 (1999) pp. 667–672.

119 K. Hono, T. Sakurai and I.J. Polmear, Pre-precipitate clustering in an Al-Cu-Mg-Ag alloy, Scripta metallurgica et materialia, 30 (1994) pp. 695–700.

120 S. Banerjee, Mechanical properties and high temperature deformation behavior of Al-Cu-Mg alloys microalloyed with Sn, PhD thesis, IIT Guwahati, (2011).

121 C. Shi, W. Mao and X.G. Chen, Evolution of activation energy during hot deformation of AA7150 aluminum alloy, Materials Science and Engineering: A, 571 (2013) pp. 83–91.

122 C. Shi and X.G. Chen, Effect of Zr addition on hot deformation behavior and microstructural evolution of AA7150 aluminum alloy, Materials Science and Engineering: A, 596 (2014) pp. 183–193.

123 C. Shi and X.G. Chen, Effects of Zr And V micro-alloying on activation Energy during hot deformation of 7150 aluminum alloys, Light Metals, (2015) pp. 163–167.

Appendix–I

Comparison of experimental and predicted flow stress for **training data** set of **Alloy-A** generated by artificial neural network (ANN) simulation

Sl No	Experimental flow stress (MPa)	Predicted flow stress (MPa)	Error (MPa)	Error (%)
1	193.3	194.0	–0.7	0.36
2	140.0	136.2	3.8	2.71
3	77.5	78.6	–1.1	1.42
4	183.6	183.9	–0.3	0.16
5	133.4	135.7	–2.3	1.72
6	208.4	209.9	–1.5	0.72
7	174.7	177.7	–3.0	1.72
8	124.4	127.8	–3.4	2.73
9	195.7	192.1	3.6	1.84
10	175.6	174.0	1.6	0.91
11	196.2	195.0	1.2	0.61
12	190.1	194.6	–4.5	2.37
13	158.2	156.9	1.3	0.82
14	212.1	211.0	1.1	0.52
15	144.3	142.4	1.9	1.32
16	76.7	77.6	–0.9	1.17
17	200.5	200.0	0.5	0.25
18	135.5	139.1	–3.6	2.66
19	232.6	232.8	–0.2	0.09
20	183.6	188.9	–5.3	2.89
21	127.4	129.3	–1.9	1.49
22	214.3	210.2	4.1	1.91
23	187.4	180.8	6.6	3.52
24	219.7	216.4	3.3	1.50
25	206.8	208.0	–1.2	0.58
26	164.6	160.1	4.5	2.73
27	217.5	219.2	–1.7	0.78
28	140.4	141.6	–1.2	0.85
29	73.3	74.6	–1.3	1.77
30	207.5	205.8	1.7	0.82
31	134.6	137.6	–3.0	2.23
32	242.7	246.8	–4.1	1.69
33	185.1	191.2	–6.1	3.30
34	126.8	127.6	–0.8	0.63
35	219.3	217.5	1.8	0.82
36	188.3	181.5	6.8	3.61
37	227.7	229.6	–1.9	0.83
38	210.3	211.8	–1.5	0.71

39	160.7	159.5	1.2	0.75
40	216.5	218.0	–1.5	0.69
41	136.5	138.3	–1.8	1.32
42	69.2	71.0	–1.8	2.60
43	210.8	205.6	5.2	2.47
44	133.8	134.4	–0.6	0.45
45	248.3	250.9	–2.6	1.05
46	185.1	190.2	–5.1	2.76
47	125.1	124.7	0.4	0.32
48	220.9	218.9	2.0	0.91
49	186.7	180.1	6.6	3.54
50	232.0	233.7	–1.7	0.73
51	210.1	212.1	–2.0	0.95
52	155.7	157.6	–1.9	1.22
53	214.5	213.7	0.8	0.37
54	129.4	134.2	–4.8	3.71
55	63.6	67.1	–3.5	5.50
56	210.7	203.9	6.8	3.23
57	131.7	130.6	1.1	0.84
58	252.2	251.7	0.5	0.20
59	185.3	188.3	–3.0	1.62
60	123.5	121.2	2.3	1.86
61	221.7	218.7	3.0	1.35
62	183.7	178.0	5.7	3.10
63	234.1	235.0	–0.9	0.38
64	209.5	211.4	–1.9	0.91
65	151.8	154.9	–3.1	2.04
66	212.7	208.5	4.2	1.97
67	124.7	129.7	–5.0	4.01
68	59.7	63.2	–3.5	5.86
69	211.1	201.5	9.6	4.55
70	129.6	126.2	3.4	2.62
71	254.8	251.6	3.2	1.26
72	185.3	185.8	–0.5	0.27
73	122.7	117.5	5.2	4.24
74	222.2	218.2	4.0	1.80
75	180.4	175.1	5.3	2.94
76	236.5	235.7	0.8	0.34
77	209.2	210.2	–1.0	0.48
78	149.1	152.0	–2.9	1.95

Appendix–II

Comparison of experimental and predicted flow stress for **testing data** set of **Alloy-A** generated by artificial neural network (ANN) simulation

Sl No	Experimental flow stress (MPa)	Predicted flow stress (MPa)	Error (MPa)	Error (%)
1	171.5	168.7	2.8	1.63
2	108.5	105.6	2.9	2.67
3	206.6	211.1	–4.5	2.18
4	103.9	105.8	–1.9	1.83
5	203.0	201.5	1.5	0.74
6	145.6	144.4	1.2	0.82
7	187.9	194.1	–6.2	3.30
8	176.2	184.5	–8.3	4.71
9	183.1	181.6	1.5	0.82
10	107.7	106.9	0.8	0.74
11	229.6	232.5	–2.9	1.26
12	103.1	105.9	–2.8	2.72
13	227.6	223.9	3.7	1.63
14	147.5	146.8	0.7	0.47
15	207.0	212.4	–5.4	2.61
16	187.3	192.3	–5.0	2.67
17	185.6	184.6	1.0	0.54
18	104.5	104.2	0.3	0.29
19	240.8	244.7	–3.9	1.62
20	102.0	103.4	–1.4	1.37
21	236.6	237.8	–1.2	0.51
22	141.9	145.8	–3.9	2.75
23	212.4	219.9	–7.5	3.53
24	187.2	193.5	–6.3	3.37
25	184.7	182.2	2.5	1.35
26	99.9	100.4	–0.5	0.50
27	247.8	246.6	1.2	0.48

28	100.6	99.9	0.7	0.70
29	242.1	242.3	–0.2	0.08
30	137.1	143.5	–6.4	4.67
31	212.8	221.5	–8.7	4.09
32	184.6	192.7	–8.1	4.39
33	178.9	178.3	0.6	0.34
34	92.7	96.2	–3.5	3.78
35	251.4	245.2	6.2	2.47
36	96.7	96.0	0.7	0.72
37	246.0	243.8	2.2	0.89
38	133.7	140.5	–6.8	5.09
39	213.4	221.6	–8.2	3.84
40	181.9	191.1	–9.2	5.06
41	175.8	173.7	2.1	1.19
42	88.4	91.6	–3.2	3.62
43	254.5	242.8	11.7	4.60
44	95.5	91.8	3.7	3.87
45	248.4	244.6	3.8	1.53
46	131.5	137.3	–5.8	4.41
47	214.3	221.2	–6.9	3.22
48	179.8	188.7	–8.9	4.95

Appendix–III

Comparison of experimental and predicted flow stress for **training data** set of **Alloy-B** generated by artificial neural network (ANN) simulation

Sl No	Experimental flow stress (MPa)	Predicted flow stress (MPa)	Error (MPa)	Error (%)
1	183.6	184.6	–1.0	0.54
2	137.1	135.3	1.8	1.31
3	74.1	73.8	0.3	0.40
4	186.9	188.2	–1.3	0.70
5	132.3	129.8	2.5	1.89
6	207.0	214.5	–7.5	3.62
7	173.6	180.2	–6.6	3.80
8	115.9	118.8	–2.9	2.50
9	199.0	200.4	–1.4	0.70
10	172.7	165.9	6.8	3.94
11	205.3	208.4	–3.1	1.51
12	193.3	191.4	1.9	0.98
13	154.2	157.5	–3.3	2.14
14	194.6	193.4	1.2	0.62
15	134.9	133.8	1.1	0.82
16	73.2	72.0	1.2	1.64
17	197.4	197.1	0.3	0.15
18	132.9	131.1	1.8	1.35
19	228.3	223.3	5.0	2.19
20	182.9	184.7	–1.8	0.98
21	117.9	118.3	–0.4	0.34
22	211.9	210.5	1.4	0.66
23	177.7	168.7	9.0	5.06
24	229.0	223.3	5.7	2.49
25	205.3	199.5	5.8	2.83
26	156.6	154.0	2.6	1.66
27	195.7	197.1	–1.4	0.72
28	128.4	128.4	0.0	0.00
29	70.6	69.1	1.5	2.12
30	199.9	202.1	–2.2	1.10
31	131.2	130.1	1.1	0.84
32	234.9	228.5	6.4	2.72
33	182.4	183.6	–1.2	0.66
34	116.8	117.2	–0.4	0.34
35	213.1	214.7	–1.6	0.75
36	174.5	167.6	6.9	3.95
37	237.0	236.0	1.0	0.42
38	205.5	206.6	–1.1	0.54

39	151.0	152.8	–1.8	1.19
40	194.3	194.6	–0.3	0.15
41	121.1	121.9	–0.8	0.66
42	66.9	65.6	1.3	1.94
43	200.3	202.9	–2.6	1.30
44	129.6	127.8	1.8	1.39
45	238.8	233.0	5.8	2.43
46	181.3	181.6	–0.3	0.17
47	115.1	115.9	–0.8	0.70
48	211.1	213.6	–2.5	1.18
49	170.7	163.6	7.1	4.16
50	242.0	242.1	–0.1	0.04
51	202.7	205.7	–3.0	1.48
52	145.4	149.9	–4.5	3.09
53	190.4	188.3	2.1	1.10
54	112.2	115.2	–3.0	2.67
55	62.7	62.2	0.5	0.80
56	198.7	200.7	–2.0	1.01
57	125.6	123.6	2.0	1.59
58	243.0	237.5	5.5	2.26
59	180.1	181.6	–1.5	0.83
60	114.4	114.1	0.3	0.26
61	209.0	211.4	–2.4	1.15
62	167.7	160.7	7.0	4.17
63	245.1	243.1	2.0	0.82
64	200.0	200.3	–0.3	0.15
65	141.5	144.8	–3.3	2.33
66	189.1	181.7	7.4	3.91
67	107.8	108.4	–0.6	0.56
68	58.4	59.1	–0.7	1.20
69	200.5	196.4	4.1	2.04
70	124.7	117.7	7.0	5.61
71	246.3	242.6	3.7	1.50
72	179.8	182.1	–2.3	1.28
73	113.5	110.8	2.7	2.38
74	209.1	213.2	–4.1	1.96
75	165.1	159.8	5.3	3.21
76	246.8	240.9	5.9	2.39
77	199.2	196.7	2.5	1.26
78	139.7	139.8	–0.1	0.07

Appendix–IV

Comparison of experimental and predicted flow stress for **testing data** set of **Alloy-B** generated by artificial neural network (ANN) simulation

Sl No	Experimental flow stress (MPa)	Predicted flow stress (MPa)	Error (MPa)	Error (%)
1	164.0	164.1	–0.1	0.06
2	101.0	102.5	–1.5	1.49
3	201.2	205.4	–4.2	2.09
4	96.6	96.1	0.5	0.52
5	206.7	211.1	–4.4	2.13
6	136.6	138.7	–2.1	1.54
7	199.6	199.5	0.1	0.05
8	170.3	178.8	–8.5	4.99
9	167.4	167.6	–0.2	0.12
10	99.5	99.5	0	0.00
11	221.1	217.1	4	1.81
12	94.4	97.3	–2.9	3.07
13	222.4	223.0	–0.6	0.27
14	137.1	136.9	0.2	0.15
15	214.8	211.0	3.8	1.77
16	181.6	181.3	0.3	0.17
17	164.8	165.1	–0.3	0.18
18	96.4	94.8	1.6	1.66
19	226.5	227.2	–0.7	0.31
20	92.9	97.0	–4.1	4.41
21	226.6	229.5	–2.9	1.28
22	131.5	135.0	–3.5	2.66
23	217.1	221.7	–4.6	2.12
24	178.3	183.5	–5.2	2.92
25	158.4	158.8	–0.4	0.25
26	92.5	89.6	2.9	3.14
27	229.9	234.0	–4.1	1.78
28	91.8	95.2	–3.4	3.70

29	227.2	232.7	–5.5	2.42
30	126.5	131.4	–4.9	3.87
31	215.5	225.4	–9.9	4.59
32	173.8	180.3	–6.5	3.74
33	151.1	151.7	–0.6	0.40
34	87.0	84.2	2.8	3.22
35	230.0	235.4	–5.4	2.35
36	88.0	91.8	–3.8	4.32
37	227.9	234.7	–6.8	2.98
38	123.1	128.1	–5	4.06
39	213.9	223.9	–10	4.68
40	169.8	174.8	–5	2.94
41	148.4	144.6	3.8	2.56
42	83.0	79.1	3.9	4.70
43	231.1	233.0	–1.9	0.82
44	87.8	87.4	0.4	0.46
45	229.7	237.4	–7.7	3.35
46	120.8	125.7	–4.9	4.06
47	215.1	221.7	–6.6	3.07
48	167.5	170.5	–3	1.79

Appendix–V

Comparison of experimental and predicted flow stress for **training data** set of **Alloy-C** generated by artificial neural network (ANN) simulation

Sl No	Experimental flow stress (MPa)	Predicted flow stress (MPa)	Error (MPa)	Error (%)
1	182.4	180.0	2.4	1.32
2	132.1	130.0	2.1	1.59
3	74.0	74.0	0.0	0.00
4	179.2	182.0	–2.8	1.56
5	134.9	128.1	6.8	5.04
6	200.1	203.1	–3.0	1.50
7	171.1	177.6	–6.5	3.80
8	105.8	111.8	–6.0	5.67
9	200.2	202.3	–2.1	1.05
10	168.8	162.0	6.8	4.03
11	203.4	201.4	2.0	0.98
12	189.2	190.4	–1.2	0.63
13	150.0	151.8	–1.8	1.20
14	195.1	193.8	1.3	0.67
15	131.8	132.7	–0.9	0.68
16	71.6	71.5	0.1	0.14
17	192.1	194.6	–2.5	1.30
18	135.8	131.1	4.7	3.46
19	223.2	220.8	2.4	1.08
20	180.9	186.3	–5.4	2.99
21	108.0	112.6	–4.6	4.26
22	220.4	217.3	3.1	1.41
23	175.5	166.3	9.2	5.24
24	221.3	218.4	2.9	1.31
25	200.2	199.0	1.2	0.60
26	155.5	152.2	3.3	2.12
27	200.2	201.0	–0.8	0.40
28	127.1	129.3	–2.2	1.73
29	68.9	67.6	1.3	1.89
30	195.9	199.7	–3.8	1.94
31	135.2	130.4	4.8	3.55
32	230.1	231.7	–1.6	0.70
33	180.8	188.4	–7.6	4.20
34	107.9	111.3	–3.4	3.15
35	226.2	224.0	2.2	0.97
36	173.1	166.1	7.0	4.04
37	226.1	227.8	–1.7	0.75
38	199.7	200.4	–0.7	0.35

39	151.1	149.4	1.7	1.13
40	201.1	200.5	0.6	0.30
41	120.8	122.8	–2.0	1.66
42	65.5	63.7	1.8	2.75
43	198.3	199.8	–1.5	0.76
44	133.8	128.4	5.4	4.04
45	233.6	235.1	–1.5	0.64
46	179.7	187.4	–7.7	4.28
47	105.7	109.3	–3.6	3.41
48	227.3	225.6	1.7	0.75
49	169.0	164.2	4.8	2.84
50	227.3	229.7	–2.4	1.06
51	196.1	198.3	–2.2	1.12
52	144.8	145.6	–0.8	0.55
53	197.6	195.7	1.9	0.96
54	111.7	115.2	–3.5	3.13
55	60.8	60.4	0.4	0.66
56	196.5	198.2	–1.7	0.87
57	129.3	125.9	3.4	2.63
58	236.3	235.4	0.9	0.38
59	179.6	185.4	–5.8	3.23
60	104.6	107.2	–2.6	2.49
61	226.0	225.3	0.7	0.31
62	165.3	161.8	3.5	2.12
63	227.8	228.2	–0.4	0.18
64	191.6	194.8	–3.2	1.67
65	139.8	141.1	–1.3	0.93
66	194.7	188.7	6.0	3.08
67	107.0	107.5	–0.5	0.47
68	57.1	57.8	–0.7	1.23
69	196.8	195.9	0.9	0.46
70	128.2	123.3	4.9	3.82
71	238.7	234.6	4.1	1.72
72	178.6	183.1	–4.5	2.52
73	103.7	105.1	–1.4	1.35
74	223.8	224.3	–0.5	0.22
75	162.2	159.2	3.0	1.85
76	229.2	225.2	4.0	1.75
77	190.4	190.5	–0.1	0.05
78	137.2	136.3	0.9	0.66

Appendix–VI

Comparison of experimental and predicted flow stress for **testing data** set of **Alloy-C** generated by artificial neural network (ANN) simulation

Sl No	Experimental flow stress (MPa)	Predicted flow stress (MPa)	Error (MPa)	Error (%)
1	164.0	159.6	4.4	2.68
2	99.4	99.0	0.4	0.40
3	192.0	194.3	–2.3	1.20
4	97.1	95.9	1.2	1.24
5	205.7	208.6	–2.9	1.41
6	137.1	133.1	4.0	2.92
7	196.7	195.4	1.3	0.66
8	177.0	176.6	0.4	0.23
9	170.6	168.1	2.5	1.47
10	97.3	97.7	–0.4	0.41
11	208.2	210.9	–2.7	1.30
12	94.9	96.9	–2.0	2.11
13	226.6	227.1	–0.5	0.22
14	138.9	134.0	4.9	3.53
15	210.3	208.6	1.7	0.81
16	184.1	180.5	3.6	1.96
17	171.0	169.1	1.9	1.11
18	93.4	93.0	0.4	0.43
19	214.3	221.1	–6.8	3.17
20	93.2	96.0	–2.8	3.00
21	232.9	238.2	–5.3	2.28
22	134.0	132.5	1.5	1.12
23	212.2	213.4	–1.2	0.57
24	180.1	179.3	0.8	0.44
25	168.8	164.5	4.3	2.55
26	89.0	87.2	1.8	2.02
27	217.3	224.0	–6.7	3.08
28	91.5	94.5	–3.0	3.28

29	235.1	241.9	–6.8	2.89
30	128.9	130.2	–1.3	1.01
31	210.3	212.9	–2.6	1.24
32	174.8	176.0	–1.2	0.69
33	161.8	157.1	4.7	2.90
34	82.3	81.5	0.8	0.97
35	217.6	223.8	–6.2	2.85
36	87.7	92.8	–5.1	5.82
37	236.7	242.5	–5.8	2.45
38	125.5	127.6	–2.1	1.67
39	207.6	210.3	–2.7	1.30
40	170.7	171.8	–1.1	0.64
41	157.0	148.4	8.6	5.48
42	78.2	76.5	1.7	2.17
43	219.3	222.5	–3.2	1.46
44	86.9	91.0	–4.1	4.72
45	238.3	242.0	–3.7	1.55
46	122.8	125.1	–2.3	1.87
47	208.1	206.7	1.4	0.67
48	168.7	167.0	1.7	1.01

Appendix–VII

Comparison of experimental and predicted flow stress for **training data** set of **Alloy-D** generated by artificial neural network (ANN) simulation

Sl No	Experimental flow stress (MPa)	Predicted flow stress (MPa)	Error (MPa)	Error (%)
1	190.1	191.4	–1.3	0.68
2	137.9	139.8	–1.9	1.38
3	78.7	78.2	0.5	0.64
4	184.5	184.4	0.1	0.05
5	131.2	129.5	1.7	1.30
6	192.8	198.5	–5.7	2.96
7	168.1	173.8	–5.7	3.39
8	108.9	113.0	–4.1	3.76
9	191.8	189.1	2.7	1.41
10	164.1	163.2	0.9	0.55
11	189.2	189.2	0.0	0.00
12	179.8	181.4	–1.6	0.89
13	148.6	150.7	–2.1	1.41
14	207.5	208.6	–1.1	0.53
15	140.5	143.7	–3.2	2.28
16	75.9	77.5	–1.6	2.11
17	198.5	199.9	–1.4	0.71
18	134.5	133.6	0.9	0.67
19	212.8	217.7	–4.9	2.30
20	182.8	184.3	–1.5	0.82
21	112.1	114.5	–2.4	2.14
22	209.1	207.0	2.1	1.00
23	170.8	170.6	0.2	0.12
24	210.2	209.8	0.4	0.19
25	193.1	197.8	–4.7	2.43
26	155.6	156.0	–0.4	0.26
27	212.6	213.0	–0.4	0.19
28	137.8	140.7	–2.9	2.10
29	73.7	74.0	–0.3	0.41
30	201.6	205.1	–3.5	1.74
31	133.8	133.1	0.7	0.52
32	218.3	223.6	–5.3	2.43
33	184.8	186.4	–1.6	0.87
34	110.8	113.2	–2.4	2.17
35	213.1	211.3	1.8	0.84
36	168.2	169.4	–1.2	0.71
37	216.8	219.1	–2.3	1.06

38	196.7	201.7	–5.0	2.54
39	153.4	153.6	–0.2	0.13
40	213.8	213.4	0.4	0.19
41	132.9	135.4	–2.5	1.88
42	69.2	69.8	–0.6	0.87
43	202.8	207.2	–4.4	2.17
44	133.3	131.6	1.7	1.28
45	221.4	225.7	–4.3	1.94
46	184.9	186.9	–2.0	1.08
47	108.9	112.3	–3.4	3.12
48	214.6	211.4	3.2	1.49
49	165.1	167.0	–1.9	1.15
50	220.4	222.4	–2.0	0.91
51	195.7	201.2	–5.5	2.81
52	148.7	149.1	–0.4	0.27
53	211.6	212.4	–0.8	0.38
54	124.2	128.7	–4.5	3.62
55	63.6	65.3	–1.7	2.67
56	201.6	209.0	–7.4	3.67
57	129.3	129.5	–0.2	0.15
58	223.0	228.1	–5.1	2.29
59	185.5	187.0	–1.5	0.81
60	107.9	111.1	–3.2	2.97
61	216.0	211.8	4.2	1.94
62	162.5	165.3	–2.8	1.72
63	221.7	224.8	–3.1	1.40
64	194.1	199.7	–5.6	2.89
65	143.9	144.9	–1.0	0.69
66	210.2	210.3	–0.1	0.05
67	118.7	120.7	–2.0	1.68
68	59.5	60.0	–0.5	0.84
69	203.3	210.6	–7.3	3.59
70	128.6	127.1	1.5	1.17
71	224.7	231.6	–6.9	3.07
72	184.7	186.8	–2.1	1.14
73	106.4	109.5	–3.1	2.91
74	216.8	212.9	3.9	1.80
75	160.3	163.6	–3.3	2.06
76	222.4	226.4	–4.0	1.80
77	193.6	198.9	–5.3	2.74
78	140.2	141.8	–1.6	1.14

Appendix–VIII

Comparison of experimental and predicted flow stress for **testing data** set of **Alloy-D** generated by artificial neural network (ANN) simulation

Sl No	Experimental flow stress (MPa)	Predicted flow stress (MPa)	Error (MPa)	Error (%)
1	165.5	170.9	–5.4	3.26
2	102.9	103.2	–0.3	0.29
3	194.6	198.7	–4.1	2.11
4	106.7	98.0	8.7	8.15
5	196.9	194.4	2.5	1.27
6	138.4	132.8	5.6	4.05
7	188.0	186.1	1.9	1.01
8	173.0	171.6	1.4	0.81
9	176.5	182.1	–5.6	3.17
10	103.4	103.3	0.1	0.10
11	213.2	217.6	–4.4	2.06
12	106.3	100.1	6.2	5.83
13	218.4	215.1	3.3	1.51
14	141.4	134.3	7.1	5.02
15	206.5	205.0	1.5	0.73
16	188.3	183.7	4.6	2.44
17	177.3	182.9	–5.6	3.16
18	100.9	99.1	1.8	1.78
19	214.8	213.1	1.7	0.79
20	104.7	99.6	5.1	4.87
21	225.4	222.8	2.6	1.15
22	138.2	131.4	6.8	4.92
23	211.0	211.5	–0.5	0.24
24	189.6	184.7	4.9	2.58
25	175.0	180.0	–5.0	2.86
26	97.4	94.1	3.3	3.39
27	225.7	228.2	–2.5	1.11
28	103.4	99.0	4.4	4.26

29	228.1	225.0	3.1	1.36
30	134.1	128.8	5.3	3.95
31	212.2	213.1	–0.9	0.42
32	188.0	181.8	6.2	3.30
33	168.0	175.4	–7.4	4.40
34	91.4	88.4	3.0	3.28
35	227.8	232.1	–4.3	1.89
36	99.5	98.4	1.1	1.11
37	229.2	226.0	3.2	1.40
38	130.4	126.6	3.8	2.91
39	213.2	213.5	–0.3	0.14
40	185.9	178.6	7.3	3.93
41	163.6	169.4	–5.8	3.55
42	87.0	81.8	5.2	5.98
43	230.2	236.5	–6.3	2.74
44	98.0	97.6	0.4	0.41
45	230.5	227.1	3.4	1.48
46	127.3	124.2	3.1	2.44
47	214.1	213.6	0.5	0.23
48	183.4	176.6	6.8	3.71

Appendix–IX

Comparison of experimental and predicted flow stress for **training data** set of **Alloy-E** generated by artificial neural network (ANN) simulation

Sl No	Experimental flow stress (MPa)	Predicted flow stress (MPa)	Error (MPa)	Error (%)
1	191.1	187.8	3.3	1.73
2	133.0	132.3	0.7	0.53
3	75.4	75.6	–0.2	0.27
4	177.7	181.1	–3.4	1.91
5	122.4	125.7	–3.3	2.70
6	203.7	203.9	–0.2	0.10
7	173.0	170.3	2.7	1.56
8	117.6	119.8	–2.2	1.87
9	197.3	197.5	–0.2	0.10
10	161.0	157.7	3.3	2.05
11	199.1	199.5	–0.4	0.20
12	190.0	189.8	0.2	0.11
13	151.8	155.4	–3.6	2.37
14	205.9	202.0	3.9	1.89
15	133.5	133.7	–0.2	0.15
16	73.3	72.7	0.6	0.82
17	190.1	191.8	–1.7	0.89
18	123.0	124.5	–1.5	1.22
19	228.4	223.0	5.4	2.36
20	183.1	177.7	5.4	2.95
21	117.4	118.0	–0.6	0.51
22	215.0	214.8	0.2	0.09
23	164.5	162.1	2.4	1.46
24	220.5	216.8	3.7	1.68
25	203.0	199.5	3.5	1.72
26	159.2	155.7	3.5	2.20
27	209.6	208.5	1.1	0.52
28	130.3	130.0	0.3	0.23
29	70.0	69.4	0.6	0.86
30	192.4	193.2	–0.8	0.42
31	121.9	121.2	0.7	0.57
32	236.1	237.6	–1.5	0.64
33	183.1	179.8	3.3	1.80
34	114.7	116.1	–1.4	1.22
35	217.7	219.9	–2.2	1.01
36	159.2	161.6	–2.4	1.51
37	226.2	229.0	–2.8	1.24

38	202.7	200.8	1.9	0.94
39	158.1	153.8	4.3	2.72
40	210.0	206.9	3.1	1.48
41	126.4	125.3	1.1	0.87
42	66.7	66.2	0.5	0.75
43	193.8	191.7	2.1	1.08
44	121.4	118.0	3.4	2.80
45	240.7	243.2	–2.5	1.04
46	181.0	180.3	0.7	0.39
47	112.0	114.2	–2.2	1.96
48	217.4	218.8	–1.4	0.64
49	154.3	159.2	–4.9	3.18
50	229.0	231.5	–2.5	1.09
51	199.3	199.6	–0.3	0.15
52	154.9	151.5	3.4	2.19
53	207.3	203.4	3.9	1.88
54	118.6	120.6	–2.0	1.69
55	61.7	63.3	–1.6	2.59
56	191.4	191.1	0.3	0.16
57	117.0	115.7	1.3	1.11
58	244.1	244.1	0.0	0.00
59	180.3	178.8	1.5	0.83
60	110.1	111.5	–1.4	1.27
61	216.5	216.3	0.2	0.09
62	150.5	156.3	–5.8	3.85
63	230.9	231.4	–0.5	0.22
64	196.0	197.9	–1.9	0.97
65	151.0	148.9	2.1	1.39
66	205.7	200.1	5.6	2.72
67	113.3	116.5	–3.2	2.82
68	58.5	60.8	–2.3	3.93
69	191.8	191.7	0.1	0.05
70	115.6	114.2	1.4	1.21
71	245.9	242.6	3.3	1.34
72	179.2	175.5	3.7	2.06
73	108.8	107.7	1.1	1.01
74	215.6	213.5	2.1	0.97
75	148.3	153.0	–4.7	3.17
76	232.3	230.7	1.6	0.69
77	194.4	196.0	–1.6	0.82
78	146.8	146.2	0.6	0.41

Appendix–X

Comparison of experimental and predicted flow stress for **testing data** set of **Alloy-E** generated by artificial neural network (ANN) simulation

Sl No	Experimental flow stress (MPa)	Predicted flow stress (MPa)	Error (MPa)	Error (%)
1	161.9	163.5	–1.6	0.99
2	97.3	102.5	–5.2	5.34
3	189.5	198.6	–9.1	4.80
4	97.8	97.9	–0.1	0.10
5	194.7	204.9	–10.2	5.24
6	135.9	136.3	–0.4	0.29
7	199.9	199.2	0.7	0.35
8	175.5	172.1	3.4	1.94
9	167.6	171.7	–4.1	2.45
10	96.3	100.2	–3.9	4.05
11	204.4	214.1	–9.7	4.75
12	95.7	94.9	0.8	0.84
13	217.5	224.2	–6.7	3.08
14	136.8	137.4	–0.6	0.44
15	215.7	215.5	0.2	0.09
16	182.0	175.8	6.2	3.41
17	165.6	171.1	–5.5	3.32
18	93.0	96.1	–3.1	3.33
19	209.7	222.9	–13.2	6.29
20	93.5	91.4	2.1	2.25
21	226.3	235.9	–9.6	4.24
22	131.3	135.9	–4.6	3.50
23	216.7	221.2	–4.5	2.08
24	178.5	175.1	3.4	1.90
25	162.4	166.8	–4.4	2.71
26	90.2	91.9	–1.7	1.88
27	212.2	224.3	–12.1	5.70
28	92.4	88.3	4.1	4.44

29	228.7	236.9	–8.2	3.59
30	126.5	133.2	–6.7	5.30
31	215.6	221.4	–5.8	2.69
32	172.5	173.3	–0.8	0.46
33	156.6	162.0	–5.4	3.45
34	85.3	87.9	–2.6	3.05
35	212.5	225.5	–13.0	6.12
36	87.9	85.8	2.1	2.39
37	230.0	234.9	–4.9	2.13
38	123.3	129.8	–6.5	5.27
39	216.0	220.5	–4.5	2.08
40	168.9	171.2	–2.3	1.36
41	152.2	157.7	–5.5	3.61
42	81.3	84.5	–3.2	3.94
43	214.2	227.6	–13.4	6.26
44	87.3	84.1	3.2	3.67
45	230.4	232.4	–2.0	0.87
46	120.9	126.2	–5.3	4.38
47	217.0	219.3	–2.3	1.06
48	167.1	169.0	–1.9	1.14

List of publication

1 Purnendu Kumar Mandal, P.S.Robi, Effect of silver on microstructure and mechanical properties of 2219 aluminum alloy, Proceedings of the International Conference: PFAM XXII, 18th - 20th December, 2013, pp 112-119, Singapore.

2 Purnendu Kumar Mandal, P.S.Robi, High Temperature deformation behavior of 2219 Aluminum Alloys Micro-Alloyed with Silver, AMPT 2014, 16th -20th November, 2014, Dubai, UAE.

3 Purnendu Kumar Mandal, P.S.Robi, Artificial neural network modeling of High Temperature Deformation of Al-Cu-Mg Alloys Micro-Alloyed with Silver, PFAM XXIII, 5th -7th December, 2014, IIT Roorkee, India.

4 Purnendu Kumar Mandal, P.S. Robi, Influence of Micro-alloying with Silver on Microstructure and Mechanical Properties of Al-Cu alloy, Materials Science and Engineering: A (under review).

5 Purnendu Kumar Mandal, P.S. Robi, Experimental Investigation and Constitutive modeling for Hot Deformation Behavior of 2219 Al-alloy micro-alloyed with silver, Journal of Engineering Materials and Technology (1st revision completed).